MAGNETIC RESONANCE SPECTROSCOPY IMAGING OF 2-HYDROXYGLUTARATE IN BRAIN TUMORS AT 3T AND 7T IN VIVO

APPROVED BY SUPERVISORY COMMITTEE

Changho Choi, Ph.D. (Mentor)

Craig Malloy, M.D.

Marco Da Cunha Pinho, M.D.

Jimin Ren, Ph.D.

Dean Sherry, Ph.D. (Chair)

DEDICATION

To my family

This dissertation is dedicated to my mom and dad who raised me with full of unconditional love. I can't ask more for their guidance and support in my life and career. I think I am the luckiest son.

I thank my lovely wife, Limei Jin, for her continuous support and willingness to bet on a man who always want to explore new things. I think I am the luckiest husband.

I thank my mentor, Dr. Changho Choi, who moistened my critical thinking with details and inspiration. Dr. Choi has always thought about how to make me a more successful person, and I think I am the luckiest student.

I want to thank, Dr. Hua Guo, who led me into NMR field and inspired me to pursue my doctoral degree.

I am truly blessed for being surrounded and loved by so many great people. I want to give my deepest gratitude for everyone's support.

MAGNETIC RESONANCE SPECTROSCOPY IMAGING OF 2-HYDROXYGLUTARATE IN BRAIN TUMORS AT 3T AND 7T IN VIVO

by

ZHONGXU AN

DISSERTATION

Presented to the Faculty of the Graduate School of Biomedical Sciences

The University of Texas Southwestern Medical Center at Dallas

In Partial Fulfillment of the Requirements

For the Degree of

DOCTOR OF PHILOSOPHY

The University of Texas Southwestern Medical Center at Dallas

Dallas, Texas

August, 2018

MAGNETIC RESONANCE SPECTROSCOPY IMAGING OF 2-HYDROXYGLUTARATE IN BRAIN TUMORS AT 3T AND 7T IN VIVO

Publication No. _____

Zhongxu An, Ph.D.

The University of Texas Southwestern Medical Center at Dallas, 2018

Supervising Professor: Changho Choi, Ph.D.

The identification of 2-hydroxyglutarate (2HG) by ^{1}H magnetic resonance spectroscopy (MRS) in patients with isocitrate dehydrogenase mutant gliomas is a significant breakthrough in neuro-oncology imaging. 2HG is the first imaging biomarker that is specific to a genetic mutation in gliomas, making the diagnosis of IDH mutant gliomas possible without biopsy. 2HG also has a significant predictive value with respect to the stage and survival in gliomas because IDH mutation carries a favorable prognosis. Gliomas are highly heterogeneous and infiltrative in malignant transformation and recur beyond the borders of the initial tumor mass. Therefore, a high-resolution 3D imaging platform to measure 2HG rapidly has an outstanding strength for monitoring IDH-mutant tumors. The present work aims to develop new techniques that provide meaningful estimation of 2HG and other metabolites in gliomas *in vivo*. As the first topic, novel triple refocusing MRS was developed at 3T for improving the 2HG signal sensitivity and specificity compared to prior methods. The optimized triple refocusing sequence

conferred excellent discrimination of the 2HG 2.25-ppm signal from the adjacent resonances and consequently improved the precision of 2HG estimation substantially. Another accomplishment was development of fast high-resolution imaging of 2HG in patients at 3T and 7T. A new echo-planar spectroscopic imaging (EPSI) readout was designed incorporating dual-readout alternated gradients (DRAG-EPSI). At 7T, DRAG-EPSI was utilized for increasing the spectral width for fully covering the spectral region of interest, which is not possible with conventional EPSI. DRAG-EPSI was used for 2D imaging of 2HG in 5 patients at 7T. At 3T, at which the spectral width of conventional EPSI is sufficiently large for covering the spectral region of interest, DRAG-EPSI was utilized for reducing the readout gradient strengths, thereby improving the imaging performance and patient compliance. DRAG-EPSI induced frequency drifts smaller by 5.5-fold and acoustic noise lower by 25 dB compared with conventional EPSI. In a 19-min scan, DRAG-EPSI produced, for the first time, 3D imaging of 2HG with precision at a resolution of $10\times10\times10$ mm^3 at 3T. Data from 4 patients indicated that DRAG-EPSI may provide reliable 3D high-resolution imaging of 2HG at 3T *in vivo*.

TABLE OF CONTENTS

PRIOR PUBLICATIONS

1. **Z. An**, V. Tiwari, W. Y., J. Baxter, M. Levy, H. K. J., E. Pan, E. A. Maher, T. R. Patel, B. E. Mickey, C. Choi, 3D High-Resolution Imaging of 2-Hydroxyglutarate in Glioma Patients using DRAG-EPSI at 3T In Vivo. *Magn Reson Med* (under review).
2. V. Tiwari*, **Z. An***, Y. Wang, C. Choi, Distinction of the GABA 2.29 ppm resonance using triple refocusing at 3 T in vivo. *Magn Reson Med*, (2018). [Epub ahead of print]
3. **Z. An**, V. Tiwari, S. K. Ganji, J. Baxter, M. Levy, M. C. Pinho, E. Pan, E. A. Maher, T. R. Patel, B. E. Mickey, C. Choi, Echo-planar spectroscopic imaging with dual-readout alternated gradients (DRAG-EPSI) at 7 T: Application for 2-hydroxyglutarate imaging in glioma patients. *Magn Reson Med* **79**, 1851-1861 (2018).
4. **Z. An**, S. K. Ganji, V. Tiwari, M. C. Pinho, T. Patel, S. Barnett, E. Pan, B. E. Mickey, E. A. Maher, C. Choi, Detection of 2-hydroxyglutarate in brain tumors by triple-refocusing MR spectroscopy at 3T in vivo. *Magn Reson Med* **78**, 40-48 (2017).
5. V. Tiwari, **Z. An**, S. K. Ganji, J. Baxter, T. R. Patel, E. Pan, B. E. Mickey, E. A. Maher, M. C. Pinho, C. Choi, Measurement of glycine in healthy and tumorous brain by triple-refocusing MRS at 3 T in vivo. *NMR Biomed* **30**, e3747 (2017).
6. S. K. Ganji, **Z. An**, V. Tiwari, S. McNeil, M. C. Pinho, E. Pan, B. E. Mickey, E. A. Maher, C. Choi, In vivo detection of 2-hydroxyglutarate in brain tumors by optimized point-resolved spectroscopy (PRESS) at 7T. *Magn Reson Med* **77**, 936-944 (2017).
7. C. Choi, J. M. Raisanen, S. K. Ganji, S. Zhang, S. S. McNeil, **Z. An**, A. Madan, K. J. Hatanpaa, V. Vemireddy, C. A. Sheppard, D. Oliver, K. M. Hulsey, V. Tiwari, T. Mashimo, J. Battiste, S. Barnett, C. J. Madden, T. R. Patel, E. Pan, C. R. Malloy, B. E. Mickey, R. M. Bachoo, E. A. Maher, Prospective Longitudinal Analysis of 2-Hydroxyglutarate Magnetic Resonance Spectroscopy Identifies Broad Clinical Utility for the Management of Patients With IDH-Mutant Glioma. *J Clin Oncol* **34**, 4030-4039 (2016).

8. A. Madan, S. K. Ganji, **Z. An**, K. S. Choe, M. C. Pinho, R. M. Bachoo, E. M. Maher, C. Choi, Proton T2 measurement and quantification of lactate in brain tumors by MRS at 3 Tesla in vivo. *Magn Reson Med* **73**, 2094-2099 (2015).
9. S. K. Ganji, **Z. An**, A. Banerjee, A. Madan, K. M. Hulsey, C. Choi, Measurement of regional variation of GABA in the human brain by optimized point-resolved spectroscopy at 7 T in vivo. *NMR Biomed* **27**, 1167-1175 (2014).
10. C. Choi, S. K. Ganji, A. Madan, K. M. Hulsey, **Z. An**, S. Zhang, M. C. Pinho, R. J. DeBerardinis, R. M. Bachoo, E. A. Maher, In vivo detection of citrate in brain tumors by ^{1}H magnetic resonance spectroscopy at 3T. *Magn Reson Med* **72**, 316-323 (2014).

LIST OF FIGURES

LIST OF DEFINITIONS

^{1}H	Proton
2HG	2-Hydroxyglutarate
B_0	Static magnetic field
B_1	External RF field
CSI	Chemical-shift imaging
Cr	Creatine
CRLB	Cramer-Rao lower bound
EPSI	Echo planar spectroscopy imaging
FID	Free induction decay
FLAIR	Fluid attenuation inversion recovery
GABA	γ-aminobutyric acid
Gln	Glutamine
Glu	Glutamate
Gly	Glycine
Lac	Lactate
mI	Myo-inositol
MRI	Magnetic resonance imaging
MRS	Magnetic resonance spectroscopy
MRSI	Magnetic resonance spectroscopy imaging
NAA	N-acetylaspartate
NMR	Nuclear magnetic resonance
PRESS	Point resolved spectroscopy
PO	Product operator
RF	Radio frequency

STEAM	Stimulated echo acquisition mode
SNR	Signal-to-noise ratio
tCr	Total creatine (Creation + Phophocreatine)
tCho	Total choline (Phosphocholine + Glycerophosphocholine + Free choline)
tNAA	Total NAA (N-acetylaspartate + N-acetylaspartyglutamate)

CHAPTER ONE

INTRODUCTION AND BACKGROUND

1.1 INTRODUCTION TO THESIS

Cancers reprogram their metabolism to meet the needs of rapid cell growth (*1*, *2*), resulting in alterations in metabolic profiles. The metabolic activity in tumors may be predictive of the genotype of the tumors and may also predict tumor grade and patient outcomes. The majority of World Health Organization (WHO) grade II and III gliomas and secondary glioblastomas harbor isocitrate dehydrogenase (IDH) mutations in the cytosol (IDH1) and mitochondria (IDH2), and these mutations are associated with better response to therapy and more prolonged survival compared to IDH wildtype tumors (*3*-*5*). The IDH mutation gives rise to the NADPH-dependent reduction of α-ketoglutarate to 2-hydroxyglutarate (2HG). As a result, 2HG, which is normally present in minute quantities, is elevated by orders of magnitude in IDH mutant gliomas (*6*-*8*). Thus, the capability to detect 2HG noninvasively provides a novel tool for identifying IDH mutation in patients without need of tumor biopsy.

The present work aims to develop new magnetic resonance spectroscopy (MRS) techniques to precisely image 2HG and other metabolites in gliomas. To accomplish the goal, the projects are divided into three parts: 1) Develop a single voxel MRS sequence (1D) for 2HG detection with high sensitivity and specificity; 2) Develop an *in vivo* 2D high-resolution imaging technique for 2HG and other metabolites; 3) Develop 3D imaging of 2HG and other metabolites in gliomas.

1.1.1 SPECIFIC AIMS:

AIM1: *In vivo* 1D Detection of 2-Hydroxyglutartate in Brain Tumors by Triple-Refocusing MR Spectroscopy at 3T

AIM2: *In vivo* 2D Echo-Planar Spectroscopic Imaging of 2HG and other metabolites in Glioma Patients with Dual-Readout Alternated Gradients (DRAG-EPSI) at 7T

AIM3: *In vivo* 3D Imaging of 2HG in Glioma Patients Using Echo-Planar Spectroscopic Imaging with Dual-Readout Alternated Gradients (DRAG-EPSI) at 3T

1.1.2 RESEARCH STRATEGY

Significance: Gliomas are highly heterogeneous and infiltrative in malignant transformation. The capability to image 2HG with high resolution rapidly has great potential for patient care and cancer research. At present, precise evaluation of 2HG at a relatively low concentration with abundant signals in the proximity remains challenging. The 2HG and interference resonances are all strongly coupled, and consequently, the coherences evolve with time in complex fashion. As an example, the 2HG C4-proton signal is not symmetric with respect to the first and second subecho times of PRESS (point-resolved spectroscopy), TE_1 and TE_2 (*9*). This dependence of strongly-coupled resonances on the inter-RF pulse timings can be utilized for manipulating the J-coupled spin coherence evolution for detection of signals of interest. Due to the effects of increased number of subecho times, triple refocusing provides an effective tool for selective detection of metabolite of interest.

^{1}H echo-planar spectroscopic imaging (EPSI) (*10*) has been used for fast imaging of brain metabolites at 3T and 4T *in vivo* (*11, 12*), but its application for high-resolution imaging of J-coupled spin metabolites is limited due to the small spectral widths (in particular at 7T), low SNR, and the requirement of high gradient strength (*13*). The new method, DRAG-EPSI, increases the spectral width, improves the signal-to-noise ratio (SNR), and reduces the burden on the gradient system, thereby improving the data quality, compared to the published EPSI methods. This eventually enables 3D high-resolution imaging of 2HG and other technically-challenging J-coupled metabolites with precision.

1.1.3 INNOVATION & APPROACH

Triple refocusing (90˚- 180˚- 180˚-180˚) has three subecho times and may provide a means of manipulating the J-coupled spin signals more efficiently (Fig. 1.1). The subecho times and RF pulse duration of a triple-refocusing sequence were tailored, with numerical simulation and phantom validation, for generating a well-defined 2HG signal at 2.25 ppm, with minimal spectral overlaps with the neighboring signals from Glu, Gln, and GABA between 2.2 and 2.3 ppm.

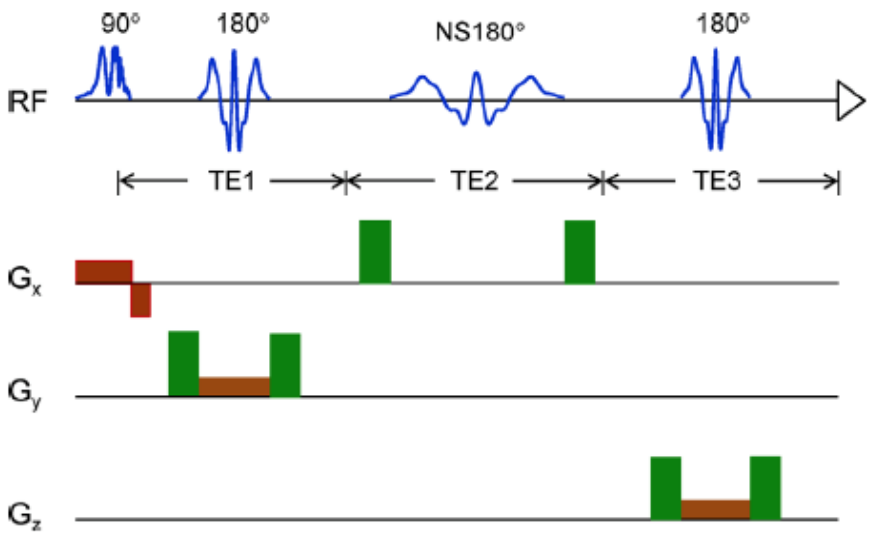

Figure 1.1 Schematic diagram of a triple-refocusing sequence.

Localization of VOI (volume of interest) is obtained with slice-selective 90° and 180° RF pulses while the second 180° RF pulse is non-slice selective (NS180). The three subecho times (TE1, TE2, and TE3) can be tailored for detection of signals of interest. All RF pulses shown are vendor-supplied (termed SHARP by Philips Medical Systems).

Several EPSI acquisition and reconstruction approaches were proposed. First, odd/even echo editing was conventionally used for neuro-metabolic imaging at 1.5T, 3T, and 4T (*11-14*). This echo editing results in a spectral width halved with respect to the acquisition dwell time. Second, the interlaced Fourier transformation approach maintains the full spectral width, but it is achieved at the expense of the prevailing gradient delay artifacts (*15, 16*). Third, a dual-readout EPSI with flyback gradients (*17*) was proposed to increase the spectral width. Data acquired using two sets of interleaved readout gradients with flyback gradients were combined to a single set of data, leading to a spectral width greater by two-fold with respect

to the acquisition dwell time. This approach was used recently for brain tumor metabolic imaging at 7T, with an in-plane resolution of 10×10 mm^2 (*18*). Lastly, time-shift EPSI was proposed for increasing spectral width (*19, 20*). Here I propose a new EPSI readout scheme, which was designed from a combination of the conventional bipolar readout gradient and dual-readout approaches. Taking advantage of the two published schemes, this new method provides increased spectral width, high SNR, and small burden on the gradient system, compared to the published EPSI methods. The new EPSI scheme, combined with our previously-reported 2HG-optimized PRESS sequence (*21*), was used for high-resolution imaging of 2HG and other metabolites at 3T and 7T.

1.2 IN VIVO MAGNETIC RESONANCE SPECTROSCOPY

Magnetic Resonance Spectroscopy, known initially as nuclear magnetic resonance (NMR) spectroscopy, is widely used for measurements of chemical compounds, such as glutamate (*22*) and lipids (*23*), in in-*vivo* and ex-*vivo* conditions of human (*24, 25*) and animal brain tissues (*26, 27*). The technique, which was invented more than a half-century ago, is one of the most robust non-invasive methods to understand human physiology today.

MRS is non-invasive, radiation-free technology that is available on nearly all magnetic resonance imaging (MRI) scanners. *In vivo* MRS was first demonstrated in mid-1980s and has been used to detect ^{1}H, ^{13}C, ^{31}P, and ^{23}Na signals of metabolites, such as 2HG, Glu, GABA, Lip, Cho, ATP, ADP, Cit, and NAA in human brain, breast, liver, prostate, heart, and muscle, for diseases like cancer, lesions, neuropsychiatric disorders, metabolic disorders, and musculoskeletal diseases (*28-32*). Among these applications and techniques, *in vivo* brain ^{1}H MRS for gliomas and neuropsychiatric disorders is predominantly popularized (*26, 29, 30*), because of its unique capability to quantify some important metabolites in these diseases, such as 2HG, Glu, GABA, Gly, Cho, NAA, and Lac.

Proton MRS detects the signals of low-molecular weight molecules, which are predominantly present in intracellular spaces. In general, a ^{1}H MRS spectrum is characterized by four factors: 1) The

resonance frequency of each signal; 2) The integrated signal strength is determined by the concentration of the metabolite; 3) T_1 relaxation time; 4) T_2 relaxation time. The two relaxation times are largely determined by the mobility of the molecules, which is affected by the physical environment of the molecule. In general, the T_2 relaxation time of the proton resonances, which is governed by the dipolar interaction (direct spin-spin interaction), is relatively long when the molecule's mobility is high, leading to well-detectable narrow MRS signals. Prior studies in cell culture reported the water T_1 and T_2 in mitochondria and cytosol, suggesting that the water mobility in mitochondria may be lower than that in cytosol (*33*). In contrast, prior in-vivo MRS studies showed that 2HG is well detectable in both IDH1 and IDH2 mutations, which are confined to cytosol and mitochondria respectively (*9*, *34*, *35*). Whether the 2HG molecules produced by mutant IDH2 are present in mitochondria and/or in cytosol is unknown, requiring further study. For large molecules such as DNA and membrane phospholipids, the mobility is very low and thus the MR signals are very broad and not clearly detectable (*36*).

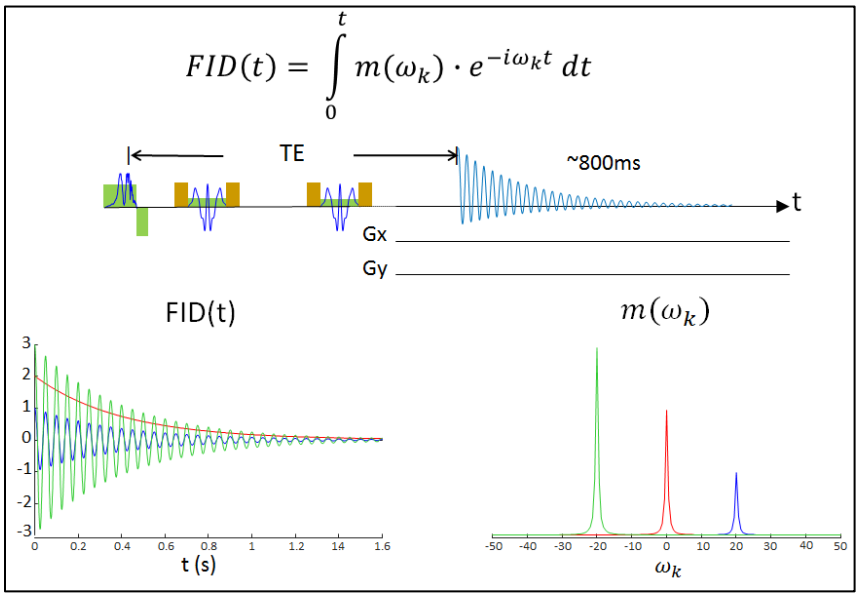

Figure 1.2 Formula and diagram of single voxel MRS

MRS can be categorized into single voxel localized MRS and multi-voxel MRS imaging (*37*).

1.2.1 SINGLE VOXEL MRS

Single voxel MRS acquires signals from a single volume, typically from 1 to 30 cm^3, defined by three slices in three orthogonal directions, as shown in Fig. 1.2. The two popular sequences are PRESS and STEAM (STimulated Echo Acquisition Mode). PRESS (*38*) is composed of one 90˚ and two 180° slice-selective RF pulses, giving a fully refocused echo. STEAM (*39*) has three slice-selective 90° RF pulses, resulting in a stimulated echo whose signal intensity is 50% of the PRESS signal. Researchers showed PRESS has lower sensitivity to motion and diffusion, compared to STEAM (*40*). However, STEAM can reach much shorter TE and is therefore used for detection of metabolites that have short T_2s.

1.2.2 MULTI-VOXEL MRS IMAGING

1.2.2.1 Chemical Shift Imaging

Multi-voxel MRS imaging (MRSI), can produce spectra from multiple locations simultaneously. As a conventional imaging method (Fig. 1.3), phase encoding gradients are applied during the VOI-prescription sequence and the ensuing free induction decay (FID) are recorded, which is termed chemical-sift imaging (CSI) (*41*, *42*). For an arbitrary voxel size, MRSI will show the same signal-to-noise ratio (SNR) as that of single-voxel MRS for an identical scan time (*14*, *43*).

MRSI requires recording of both spatial and spectral information. To achieve the spatial localization of spectral information, a time dependent component needs to be added to the model which results in a prolonged acquisition window to resolve signals with different frequencies, as shown in Fig. 1.3. The function of phase encoded gradients G_x and G_y is to navigate free induction decay acquisition through the K-space trajectory as if the frequency ω_k is another “spatial” axis. A 3D Fourier transformation will convert the K-space and time domain into spatial (2D) and frequency domain (1D), respectively. However, this requires recording of each K-space point at a time and potentially a very long scan time is

required when the voxel size is small (i.e., large number of voxels) or 3D spatial imaging is needed. The scan time in CSI is calculated by the product of TR times the number of phase encoding steps, which is

$$CSI(2D)\ scantime = TR\ \times (N_x \times N_y) \qquad \text{Equation 1.1}$$

where N_x and N_y are number of phase encoding in x and y directions, respectively.

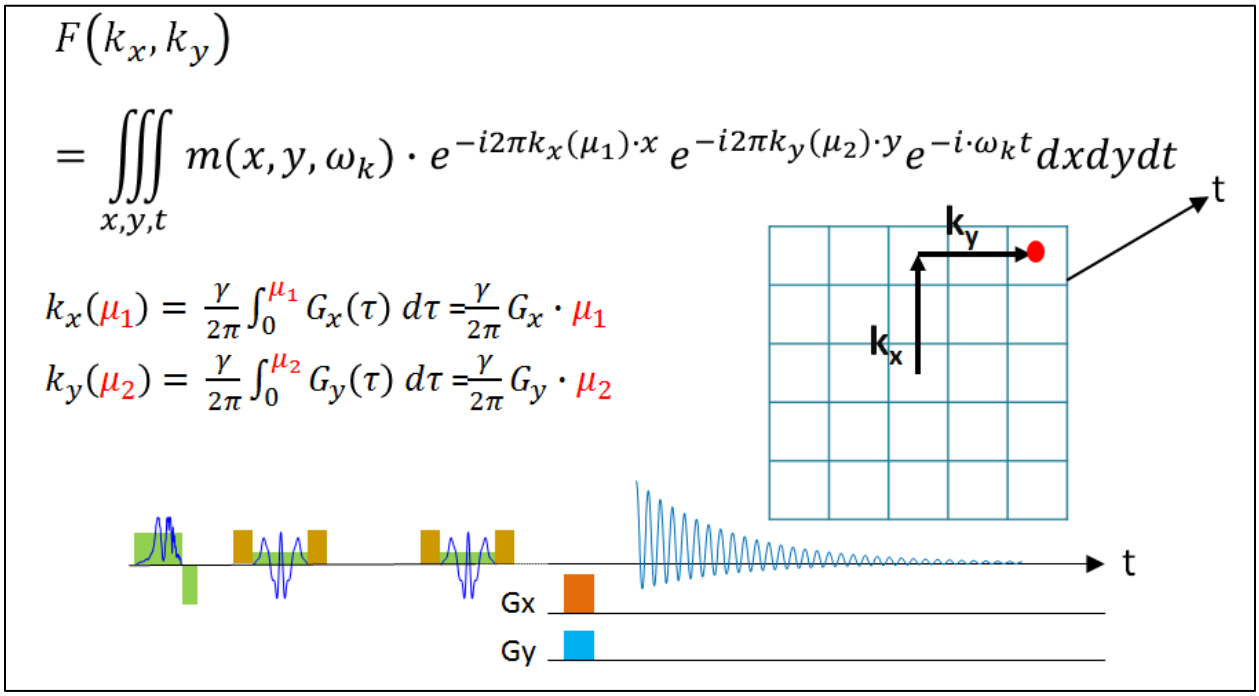

Figure 1.3 Formula and diagram of CSI

For example, if TR = 2 s, FOV = 200×240 mm^2, and voxel size = 10×10 mm^2. The acquisition matrix size is 20×24 ($N_x \times N_y$). The 2D-CSI scantime for NSA = 1 is 2×20×24 s = 16.0 min. If the voxel size is reduced to 5×5 mm^2, then the scan time becomes 2×40×48sec = 64.0 min. For a 3D-CSI, TR = 2 s, FOV = 200×240×160 mm^3, voxel size = 10×10×10 mm^3, and matrix size = 20×24×16 ($N_x \times N_y \times N_z$), the scan time will be 4.3 hours for NSA = 1 which is not practical for a human scan.

To overcome this issue, several fast spectroscopic imaging methods were proposed for *in vivo* imaging of brain metabolites, including parallel spectroscopic imaging (*44*), echo planar spectroscopic imaging(*10, 45, 46*), spiral spectroscopic imaging (*47*), rosette spectroscopic imaging (*48*), compressed sensing spectroscopic imaging (*49*) and hybrids of some methods (*50-52*).

1.2.2.2 Echo Planar Spectroscopy Imaging

Echo planar spectroscopy imaging (EPSI) was introduced as one of the fast alternatives of CSI. As shown in Fig. 1.4, EPSI replaces one of the phase encoding step with pairs of bipolar frequency encoding gradients which can reduce the scan time by N_y fold. Therefore, for matrix size = 20×24×16, EPSI only needs 10.7 minutes (2×20×16 s) for NSA = 1, instead of 4.3 hours by CSI. To be noticed, the SNR is $\sqrt{N_y}$ times lower for each NSA in EPSI campared to CSI, but EPSI can choose to scan NSA = 2 (scantime = 21.4 min) which may be sufficient for imagign of many metabolites in the brain. This is not achievale with CSI.

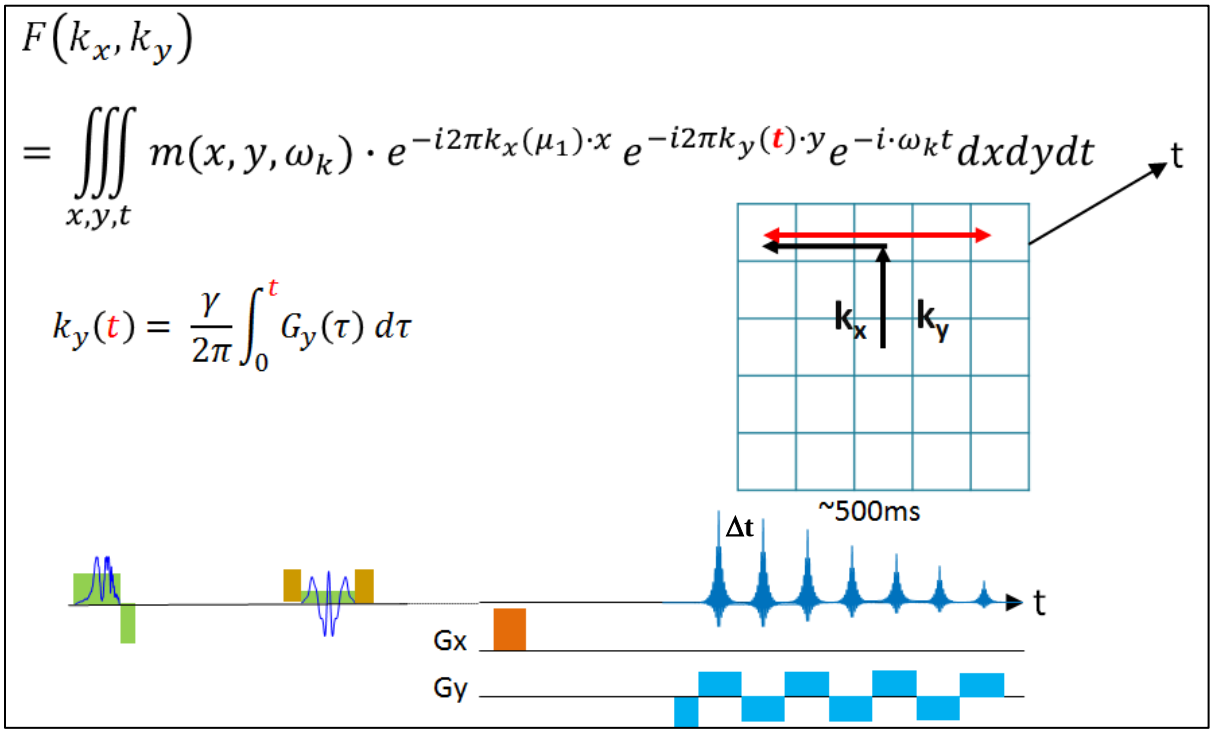

Figure 1.4 Formula and diagram of EPSI

The scan time reduction of EPSI comes with a cost. Because of the data were acquired using an alternated-gradient readout with a dwell time of Δt, the data acquired during positive and negative polarity gradients present opposite gradient delay effect, resulting in ghost artifact, and thus cannot be combined directly. To overcome this challenge, in conventional EPSI, the data acquired during the positive- and negative-polarity gradients are separated into odd- and even-echo sets and each data set is

processed for eddy current compensation and phase correction. The two sets of data may then be averaged to improve SNR. The ghost artifacts due to asymmetries in gradient switching can be removed with the odd/even echo editing (*53*), but the dwell time of the reconstructed data is twice ($2\Delta t$) the acquisition dwell time, resulting in spectral width of $1/(2\Delta t)$. The spectral width of this conventional EPSI in human MR scanners is typically about 1 kHz (*12, 14*), which is ~7.8 ppm at 3T and ~3.3 ppm at 7T. To increase the spectral width of conventional EPSI, a substantially high strength bipolar gradient is needed, which creates challenges in data acquisition and processing, including central frequency drift from system overheat and reduced patient compliance with high acoustic noise. My present work aims to overcome this challenge by using a different acquisition and reconstruction method and apply it for 3D high-resolution 2HG imaging.

There are advantages and disadvantages of single-voxel MRS and multi-voxel MRS, and thus they are used in the different application (*29, 30, 43*). For single-voxel MRS, the MRS sequences are readily available in most of human MR scanners. B_0 and B_1 shimming on the single localized volume is relatively straightforward, and the data processing is readily manageable. For these reasons the data quality (e.g., SNR and spectral resolution) is in general higher in single voxel MRS than MRSI. Therefore, single voxel MRS is widely used for studying technically-challenging neuro-transmitters (GABA, glutamate, etc.) in neuropsychiatric diseases such as autism (*54, 55*), schizophrenia (*56, 57*), and depression (*58, 59*). The advantage of MRSI is the ability to map the spatial distribution of metabolites (*14, 60*). However, it is challenging to achieve excellent shimming and water suppression in MRSI (*61, 62*). Practically in ^{1}H MRSI, lipid signals from the brain skull contaminate the data and make it difficult to detect low concentration metabolites (*61, 63*). Furthermore, the data processing needs to be optimized for extensive data sets, i.e., 5000 spectra in 3D MRSI (*12, 64*). Because of the pros and cons mentioned above, MRSI is usually used for imaging large signal metabolites such as NAA, Cho, Cr in brain tumors, the concentrations of the metabolites may be substantially altered heterogeneous in a large volume (*14, 18, 65*).

1.3 BASIC NMR THEORY

Spin is an intrinsic angular momentum inherent to any fundamental particle including protons. In fact, no particles physically spin. The concept of spin was derived from the quark theory. In the physical world, a rapidly rotating top will precess in a direction determined by the torque exerted by its weight. Similarly, a nucleus with a spin angular momentum will precess in a static magnetic field perpendicular to the field direction. Because a nuclear spin possesses a magnetic moment arising from the angular momentum of the nucleus, this magnetic moment will create torque when placed in a static magnetic field.

If the external static magnetic field is B_0, the magnetic moment (μ) has associated magnetic energy given by

$$E = -\boldsymbol{\mu} \cdot \vec{\boldsymbol{B}}_{\mathbf{0}} = -\mu_z \times B_0 \qquad \text{Equation 1.2}$$

where the magnetic moment (μ) is related to angular momentum **L** through

$$\boldsymbol{\mu} = \gamma \boldsymbol{L} \qquad \text{Equation 1.3}$$

where γ is gyromagnetic ratio of nucleus under investigation.

The angular momentum in z-direction, L_z, is given by

$$L_z = L \times \cos\theta = \left(\frac{h}{2\pi}\right)\sqrt{I(I+1)} \times \cos\theta \qquad \text{Equation 1.4}$$

where h is Planck's constant ($6.626068 \times 10^{-34} Js$), and I is the spin quantum number which can only be integral or half-integral.

Based on quantum mechanical theory, the angle θ between **μ** and $\mathbf{B_0}$ is given by

$$\cos\theta = \frac{m}{\sqrt{I(I+1)}} \qquad \text{Equation 1.5}$$

where m, a second quantum number, can have 2I+1 values, given by

$$m = I, I-1, I-2, I-3, \ldots, -I+1, -I \qquad \text{Equation 1.6}$$

Therefore, Eq. 1.4 and 1.5 give

$$L_z = \left(\frac{h}{2\pi}\right) \times m \qquad \text{Equation 1.7}$$

and

$$E = -\gamma\left(\frac{h}{2\pi}\right) \times m \times B_0 \qquad \text{Equation 1.8}$$

Since m is a discrete number, multiple energy states are being created by the magnetic moment. For instance, a proton (^{1}H) has a spin of I = ½ with two m (- ½ and ½) for two energy states, respectively. The transition from a low energy state to a high energy stage can be achieved when the energy of the applied electromagnetic wave is same as the energy difference between two states.

The energy of an electromagnetic wave is given by

$$E_{wave} = h\nu_0 \qquad \text{Equation 1.9}$$

where ν_0 is the applied wave frequency.

Therefore, for proton,

$$\Delta E = \gamma\left(\frac{h}{2\pi}\right) \times B_0 = h\nu_0 \qquad \text{Equation 1.10}$$

which results in the famous Larmor equation,

$$\omega_0 = 2\pi \times \nu_0 = \gamma B_0 \qquad \text{Equation 1.11}$$

where ω_0 is the so-called Larmor frequency. Therefore, the precession frequency ω_0 is directly proportional to the applied magnetic field $\mathbf{B_0}$. The Larmor frequency of a proton is approximately 64MHz at 1.5 Tesla, 128 MHz at 3 Tesla, and 298 MHz at 7 Tesla.

1.4 CHEMICAL SHIFTS

The local chemical environment plays a vital role in determining the resonance frequencies. In fact, this effect comes from the small net magnetic field applied by the molecule's electron which rotates around the nucleus with a negative charge. The effective field at the nucleus can be expressed as

$$B_{0eff} = B_0(1 - \sigma) \qquad \text{Equation 1.12}$$

where σ is the shielding constant with no unit. This effect makes the resonance frequency depend on B_0 and it would be difficult to compare chemical shifts measured at different field strengths. To make the comparison easy, it is standard to express chemical shifts in parts per million (ppm) relative to a reference

compound, which is tetramethylsilane (TMS) for ^{1}H and ^{13}C MRS. The chemical shifts (δ) can then be written as

$$\delta = \left(v - v_{ref}\right) * 10^{6}/v_{ref} \qquad \text{Equation 1.13}$$

where v is a signal of interest and v_{ref} is the reference signal. For ^{1}H MRS, chemical shift of TMS is 0 ppm. For in-vivo ^{1}H MRS, TMS signal is not available as a reference, therefore one of the indigenous spectral signals, such as water set to 4.68 ppm or the N-acetyl resonance of N-acetylaspartate (NAA) in the brain set to 2.01 ppm, is often used as a chemical shift reference.

1.5 J-COUPLING EFFECTS

Besides the chemical shift effect, Gutowsky discovered in 1951 that there is multiplicity effect on magnetic resonance signals (*66*). This effect is known as J-coupling, scalar-coupling, or indirect spin-spin coupling effect. The J-coupling comes from electrons' interactions through chemical bonds with the neighboring nucleus.

The multiplicity of J-coupling effect provides information on the structures of chemical bonds and thus can be used to predict a chemical structure and quantification. The J-coupling effect can be homonuclear or heteronuclear, and the interaction is reciprocal, namely, when A splits B, then B slips A. The strength of the signal split depends on 1) the relationship between the difference in two couple spins' chemical shift frequencies, and 2) the number of spins coupled.

In a simplified system, A_1B_1, A and B spin signals will be symmetrically split on $\frac{\delta_A+\delta_B}{2}$. When $|\delta_A - \delta_B| = 0$, there is no split. In strongly coupled condition, $|\delta_A - \delta_B| \sim J_{AB}$, the patterns of peaks look like Fig. 1.5, which is computer simulated. As the two spins' chemical shift distance gets larger, where $|\delta_A - \delta_B| \gg J_{AB}$ which is known as the weakly coupling limit, the four peaks (two from A spin, two from B spin) will become identical. The coupling strength J_{AB} is independent of field strength B0 while the chemical shift frequency difference $|\delta_A - \delta_B|$ increases as field strength increase. Therefore, at extremely

high magnetic field (15 to 25 Tesla), which is used for chemistry and *ex vivo* experiments, weak coupling is common and easy to interpret.

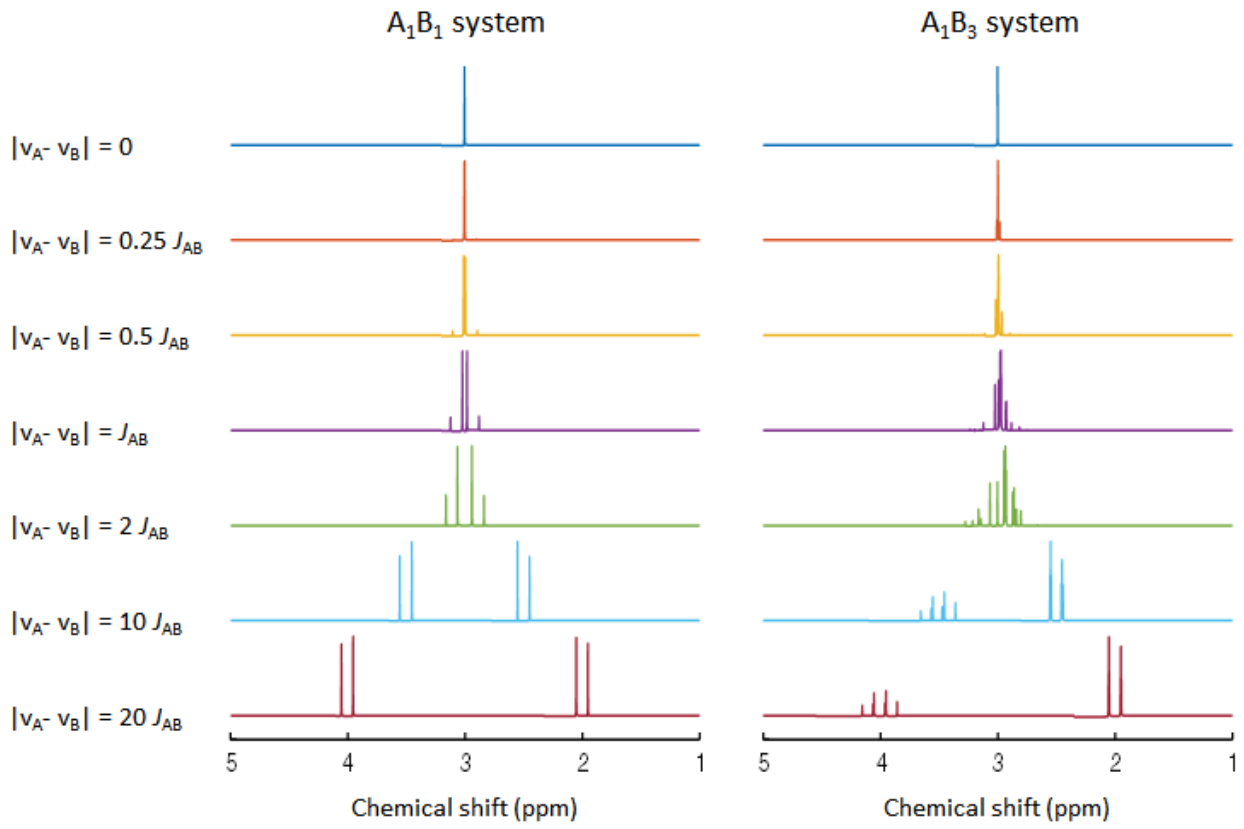

Figure 1.5 Simulated A_1B_1 and A_1B_3 NMR spectra

For *in vivo* MRS in human (1 to 7 Tesla), strongly coupled systems together with large number of spins are often encountered. In these cases, the symmetricity of signals would be destroyed, and the signal pattern becomes very complicated. As shown in Fig. 1.5, an A_1B_3 spin system exhibits an irregular pattern throughout the spectrum under the strong coupling condition, ($|\delta_A - \delta_B| \sim J_{AB}$). Therefore, a computer simulation is the only way to accurately assign the peaks of strongly coupled systems in *in vivo* MRS.

1.6 PRODUCT OPERATOR ALGORITHM AND COMPUTER SIMULATION

Quantum-mechanical simulations can be used to optimize the MRS sequence for detection of signals of interest and to create model spectra of metabolites for spectral fitting. The time evolution of the density operator is calculated numerically incorporating the shaped radio-frequency and gradient pulses. The product operator-based transformation matrix method (*67, 68*) provides an efficient tool for calculating MR spectra at numerous echo times. An echo time that gives the maximum signal of interest is then selected for the sequence used in the patient study. The density matrix simulations are programmed with Matlab (The MathWorks Inc.). Published chemical shift and coupling constants are used in the simulation (*69-71*).

The time evolution of the density operator is described by the Liouville-von Neumann equation (*67*)

$$\frac{\partial \rho}{\partial t} = -i[H, \rho] \qquad \text{Equation 1.14}$$

which has a solution

$$\rho = \exp(-iHt)\rho_0 \exp(iHt) \qquad \text{Equation 1.15}$$

for a time-independent Hamiltonian *H*. The Hamiltonian *H* may include the chemical shift (CS) and scalar coupling (J) terms and the radio-frequency (RF) and gradient (G) pulse terms,

$$H = H_{CS} + H_J + H_{RF} + H_G \qquad \text{Equation 1.16}$$

in the rotating frame.

1.6.1 PRODUCT OPERATOR ALGORITHM

For design and analysis of MR sequences with RF pulses, there are different models to describe NMR phenomena (*72*). First of all, the classical vector model is the simplest form of describing spin dynamics by ignoring J coupling effect and simulating the magnetization using Bloch equations. The classical vector model is sufficient for basic experiment of MRS including composite pulses (*73, 74*), slow chemical exchange (*75, 76*), spin imaging (*77*). Secondly, to encounter J coupling effect, semiclassical vector model, where it assigns a vector to each individual transition, were proposed (*72*). Although the

method was successful for some experiments, it cannot describe the interdependence of z-components with single transitions that have same energy states, thus requires careful handling of the process (*78-80*). In contrast to the classical and semiclassical vector models, product operator (PO) approach can adequately describe polarization transfer and multiple quantum coherences by rotating the products of angular momentum operators.

The subject of product operators is introduced through their matrix representations by R.R. Ernst (*72*) ,

$$\rho_0 = 2^{q-1} \prod_{k=1}^{N} (I_{kv})^{a_{sk}} \qquad \text{Equation 1.17}$$

where N = total number of I = ½ nuclei in the spin system, k = index of nucleus, v = x, y or z, q = number of single-spin operators in the product, a_{sk} = 1 for q nuclei and a_{sk} = 0 for the N-q remaining nuclei. For example, for the two-spin system, 16 product operators can be constructed.

$$\rho_0{}^{N=2} = 2 \times [operator\ for\ spin\ I_1\ (4\ choices)] \times [operator\ for\ spin\ I_1\ (4\ choices)]$$

Equation 1.18

namely,

q = 0 ½ E; (E is unity operator)

q = 1 I_{1x}, I_{1y}, I_{1z}, I_{2x}, I_{2y}, I_{2z};

q = 2 $2I_{1x}I_{2x}$, $2I_{1x}I_{2y}$, $2I_{1x}I_{2z}$, $2I_{1y}I_{2x}$, $2I_{1y}I_{2y}$, $2I_{1y}I_{2z}$, $2I_{1z}I_{2x}$, $2I_{1z}I_{2y}$, $2I_{1z}I_{2z}$;

1.6.2 PRODUCT-OPERATOR-BASED DENSITY MATRIX SIMULATION

For a spin system with N coupled protons (spin = 1/2), 4^N product operators can constitute a complete set in Liouville space (*72*). The density matrix may be written as a linear sum of the PO terms α

$$\rho = \sum_{i=1}^{4^N} c_i a_i \qquad \text{Equation 1.19}$$

where ρ and α are $2^N \times 2^N$ square matrices with complex entries, and the coefficient *c* is real. The density operator can be expressed as a column vector σ which is composed of the coefficients *c*,

$$\sigma = \begin{pmatrix} c_1 \\ c_2 \\ \vdots \\ c_{4^N} \end{pmatrix} \qquad \text{Equation 1.20}$$

The density operator evolution during a radio-frequency pulse can be put in terms of a single matrix multiplication,

$$\sigma' = \begin{pmatrix} c_1' \\ c_2' \\ \vdots \\ c_{4^N}' \end{pmatrix} = \begin{pmatrix} T_{1,1} & T_{1,2} & \dots & T_{1,4^N} \\ T_{2,1} & T_{2,2} & \dots & T_{2,4^N} \\ \vdots & \vdots & \vdots & \vdots \\ T_{4^N,1} & T_{4^N,2} & \cdots & T_{4^N,4^N} \end{pmatrix} \begin{pmatrix} c_1 \\ c_2 \\ \vdots \\ c_{4^N} \end{pmatrix} = T\sigma \qquad \text{Equation 1.21}$$

where the transformation matrix T is a 4^Nx4^N square matrix with real entries. The T-matrix is constructed for each spatially/spectrally-selective shaped radio-frequency pulse and used for calculating the time evolution of the density operator during the MRS sequences for each metabolite.

For a time-dependent radio-frequency pulse whose envelope consists of n numbers as a function of time, H_{RF} and consequently H may be constant during each time period Δt. The density operator following the RF pulse is calculated using a (total) time evolution operator $V_{total,}$

$$\rho = \mathrm{V}_{total}^{-1}\, \rho_0 V_{total} \qquad \text{Equation 1.22}$$

where

$$V_{total} = V_1 V_2 \cdots V_i \cdots V_n \qquad \text{Equation 1.23}$$

The time evolution operator for the i-th period of the radio-frequency pulse, Vi, is obtained using

$$V_i = U \exp\left(-iH_i^{diag}\Delta t\right) U^{-1} \qquad \text{Equation 1.24}$$

where H_i^{diag} (= $U^{-1}H_iU$) and U are the diagonalized matrix and the unitary matrix of the Hamiltonian of the i-th period, H_i, respectively.

When a gradient pulse is applied during a radio-frequency pulse for slice selection, since H_G and consequently H are position dependent, the space is divided into small segments and the calculation of Eq. 1.22 is undertaken for individual segments, assuming uniform H_G within each segment. The simulation for slice selection is usually conducted on a 20 mm thick slice at the center of a 30 mm sample. The sample space is divided into 150 segments, the spatial resolution being 1% with respect to the slice thickness (i.e., 0.01 = 30/150/20). The 90˚ and 180˚ slice-selective radio-frequency pulse envelopes consist of 500 and 200

digits for radio- frequency amplitude/phase variations, respectively. The bandwidths of the slice-selective 90° and 180° pulses are 4220 and 1260 Hz, respectively. With a radio-frequency carrier at 3 p.p.m., the slices of resonances between 1 – 5 ppm are all included within the sample dimension for both 90˚ and 180˚ radio-frequency pulses. For the 180° pulse, two density matrices are calculated with two orthogonal radio-frequency phases (i.e., 0 and π/2), and the slice-localized density matrix is obtained via subtraction between the matrices,

$$\rho_{slice} = \frac{\rho_{\phi=0} - \rho_{\phi=\frac{\pi}{2}}}{2} \qquad \text{Equation 1.25}$$

The square matrix ρ_{slice} slice was then converted to a column vector σ, whose *i*-th element is calculated from

$$c_i = trace(a_i \rho_{slice}) \qquad \text{Equation 1.26}$$

where α_i is the normalized *i*-th PO term of the spin system and i = 1, 2, …, 4^N. A single-column matrix is calculated from each PO term as an initial density operator prior to the radio- frequency pulse, and placed in the corresponding column of the T-matrix. For 2HG with 5 coupled spins, a 4^5x4^5 transformation matrix is constructed from the 4^5 column vectors, each from each PO term. The calculation of the T-matrix of 2HG for the slice selective 180° pulse is completed in ~1 hours in a PC (with 4 cores). The T-matrix calculation time for the PRESS 90° RF pulse is very short (~ 30 s) because the calculation is to be done only for a single PO term (i.e., I_z). For calculating a spectrum following a PRESS sequence

$$90 - TD_1 - 180 \quad - \quad TD_2 \quad - \quad 180 - TD_3 - \text{ Acquisition}$$

$$| \leftarrow \quad TE1 \quad \rightarrow | \leftarrow \quad TE2 \quad \rightarrow |$$

the simulation begins with the calculated density matrix of the slice-selective 90˚ pulse. The time evolution during the inter-radio-frequency pulse delay (TD_1) is calculated using

$$\rho = V^{-1} \rho_0 V \qquad \text{Equation 1.27}$$

where $V = U\, exp(-i\, H^{diag}\, TD_1)\, U^{-1}$, and H^{diag} and U are formed from $H = H_{CS} + H_J$. After this, the square density ρ matrix is converted to a column matrix σ using Eq. 1.26 and multiplied by the 180˚ pulse T-matrix (Eq. 1.21), giving a column matrix at the end of the ss180. This column matrix is then converted to a square

matrix ρ for calculating the density operator evolution during the subsequent time delay (TD_2). The calculation of the density operator evolution is continued to obtain the density operator ρ at the end of the sequence. The expectation values of single-quantum coherences are then extracted from the ρ, using trace(I_ρ), to construct a time- domain signal, which is Fourier transformed to obtain a spectrum in the frequency domain. The spoiling gradients symmetric about the PRESS 180° pulses are omitted in the simulation because the 2-step phase cycling in the *T*-matrix calculation eliminated the outer-band magnetization completely. With this transformation matrix method, a 3D-localized PRESS spectrum of 2HG was calculated in < 0.5 s in a PC.

CHAPTOR TWO

METABOLITES OF INTEREST FOR IN VIVO MRS IN BRAIN TUMORS

^{1}H MRS can detect up to 20 metabolites in the human brain, and some of them are very important in tumor study. Cho, NAA, and Cr give rise to the three large signals in conventional *in vivo* MRS and can be easily detected. Cho is associated with cell proliferation and member synthesis and is significantly elevated in brain tumors. NAA, a neuronal marker, decreases in brain tumors. There are many reports on the correlation of Cho and NAA levels with tumor grade and progression (*81-85*). However, using Cho and NAA as a marker for malignancy has limitations on its own because other brain lesions like lymphoma or metastases also have Cho elevation and NAA decrease (*86, 87*). ^{1}H MRS can also be used to measure 2-hydroxyglutarate (*9, 88-93*), glycine (*13, 94-97*), lactate (*98, 99*), citrate (*100-102*), myo-inositol (*97, 103*), glutamate (*104, 105*), and glutamine (*104, 106*) in brain tumors.

2.1 2-HYDROXYGLUTARATE

The breakthrough discovery of mutations in isocitrate dehydrogenases (IDHs) 1 and 2 (*3, 4*) in the earliest grade gliomas and the subsequent identification of the oncometabolite 2-hydroxyglutarate (2HG) as a direct consequence of these mutations (*107*) have provided new insights into gliomagenesis and opened up new opportunities for treatment. These heterozygous mutations are confined to the active site of the enzyme and result in a neomorphic activity that causes the mutant enzyme to produce 2HG, and as a result 2HG, which is normally present in vanishingly small quantities, is elevated by 2 - 3 orders of magnitude in IDH-mutated gliomas (*7, 8, 107*). Moreover, recent large-scale molecular studies of adult lower-grade gliomas (WHO grade 2 and 3 astrocytomas, oligodendrogliomas, and mixed gliomas) have clearly defined the IDH mutation as centrally important in determining prognosis (*108-110*). Patients with IDH-mutated oligodendrogliomas that harbor loss of chromosomal arms 1p and 19q (1p/19q codeleted)

have significantly prolonged survival when compared with those without the codeletion. These findings prompted a recent molecular reclassification of gliomas (*111*), which is likely to lead to a more accurate classification of individual tumors and is expected to play a role in treatment decision making and the future design of clinical trials in glioma. 2HG is currently the only direct metabolic consequence of a genetic mutation in a cancer cell that can be identified through noninvasive imaging and thus accumulation of high concentrations of 2HG in IDH-mutated cells has opened up an opportunity for development of 2HG as a clinical biomarker.

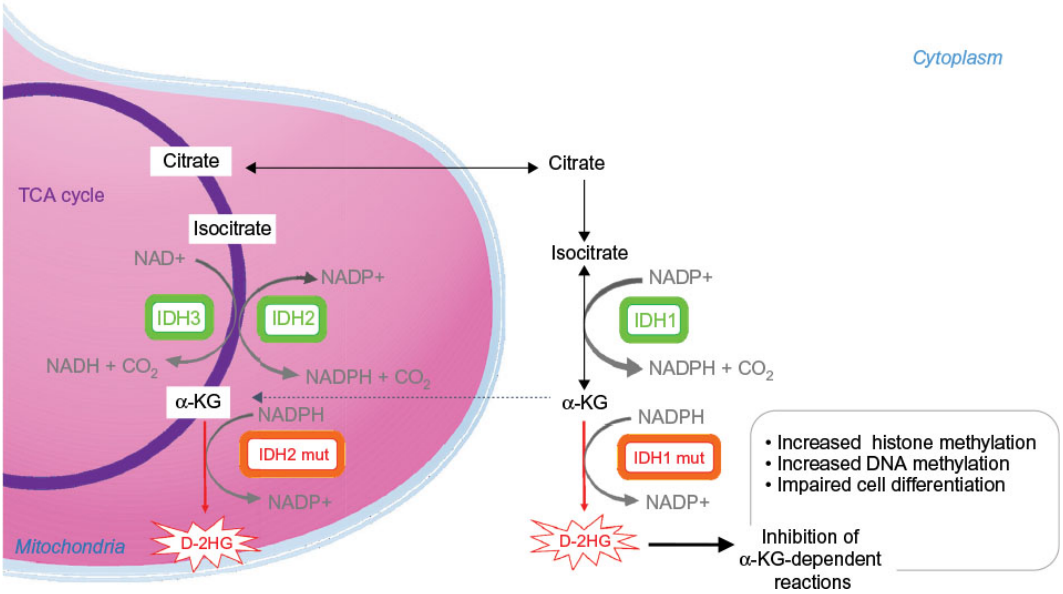

Figure 2.1 Enzymatic activities of IDH wild-type and IDH mutated enzymes (112)

Non-invasive identification of elevated 2HG therefore has significant clinical utility in patient care. At present, precise evaluation of 2HG at a relatively low concentration with abundant signals in the proximity remains challenging at 3T. When targeting the 2HG 2.25-ppm resonance, the major interferences include glutamate (Glu) and glutamine (Gln). The Glu C4-proton and Gln C3-proton resonances (2.35 and 2.12 ppm respectively) can interfere with 2HG estimation extensively when their signals are large compared to the 2HG signal. The 2HG and interference resonances are all strongly coupled, and consequently, the coherences evolve with time in complex manners. Gliomas are highly heterogeneous and infiltrative in malignant transformation and recur beyond the borders of the initial tumor mass. The need of a surveillance

technique for use in extended areas of the tumor is a high priority. The tumor cellularity and the 2HG level may vary within a tumor mass, and their spatial distributions may be non-uniform. A high-resolution 3D imaging platform to measure 2HG rapidly is an outstanding strength for monitoring IDH-mutant tumors. With the ability to detect 2HG by high-resolution 3D MRS imaging, this metabolite could be used to follow patients with high accuracy.

2.2 CHOLINE

The major signal of total choline, composed of glycerophosphocholine (GPC), phosphocholine (PC), and free choline (fCho), is located at 3.21 ppm, with a total concentration around 1.5 mM. Choline is involved in membrane synthesis and degradation, and the level of choline elevates when membrane turnover increases. Therefore, choline is being used as a marker of tumor proliferation and cellularity. Choline is elevated in brain tumors due to increased phospholipid metabolism (*113, 114*). Specifically, elevation of choline in IDH1-mutant gliomas may be attributed to membrane synthesis of mitochondria which is increased to compensate for the utilization of α-ketoglutarate and NADPH for the α-ketoglutarate to 2HG conversion in the cytosol (*115*).

2.3 NAA

As one of the most abundant amino acids, NAA gives rise to the largest peak at 2.01 ppm in ^{1}H MRS in the normal adult brain. NAA is predominantly presented in neurons, axons, and dendrites within the central nervous system and thus known as a neuronal marker. It is believed to be synthesized in neuronal mitochondria by aspartate and acetyl-CoA and used for lipid synthesis, protein synthesis (*116*). NAA concentration decreases in many diseases that result in neuronal and axonal loss, which include brain tumors, multiple sclerosis, and infarcts (*117*).

2.4 GLYCINE

Glycine (Gly), a non-essential amino acid, exerts inhibitory action via chloride-permeable ion channels (*118*), and also functions as a co-agonist at the excitatory N-methyl-D-aspartate (NMDA) receptors in the central nervous system (*119*). Abnormal levels of Gly have been implicated in neuropsychiatric disorders (*119, 120*). Elevated levels of Gly have been reported in central neurocytomas and Gly encephalopathy (*121, 122*). Also, Gly is elevated in malignant brain tumors and thus may be a biomarker of aggressiveness (*123, 124*). Recent metabolic profiling studies have reported that Gly consumption and synthesis are correlated with rapid cancer cell proliferation, suggesting the role of Gly in tumor cell metabolic reprogramming (*125, 126*). The capability to analyze human brain Gly non-invasively *in vivo* is therefore of high clinical significance.

The Gly singlet from two uncoupled protons resonating at 3.55 ppm is obscured by the four J-coupled resonances of myo-inositol (mI) at 3.61 and 3.52 ppm (*70*). For short-TE MRS at 3 T, the Gly signal appears on top of the largest peak of mI for linewidths larger than 3 Hz, and thus separation between Gly and mI is often elusive when mI is present at much higher concentrations than Gly *in vivo*. Many previous studies have exploited the J coupling difference between Gly and mI for the detection of Gly. In measurements of Gly by PRESS, TE averaging at 4 T (*127*) and long-TE (160 ms) PRESS at 3T (*94*), the Gly signal is detected as a shoulder signal on the larger mI multiplet in the healthy brain. Improved suppression of the mI signal in the proximity of the Gly resonance can be achieved at 3 T using triple refocusing (*97, 128*).

The resonances of mI that interfere with Gly detection are strongly coupled, and thus the coherences evolve with time in a complex manner which suggests that the mI spin coherence evolution can be efficiently manipulated by changing the radiofrequency (RF) pulses, as well as the inter- RF pulse time delays. Gly in the human brain may be notably different between gray matter (GM) and white matter (WM), as shown in previous MRS studies (*95, 129*). Tumors do not contain the GM or WM tissue type. This complicates the evaluation of the Gly abnormality in tumors in that the measurement may need to be

compared with that from a normal-appearing contralateral region and/or from a region in healthy subjects whose location is similar to the tumor location.

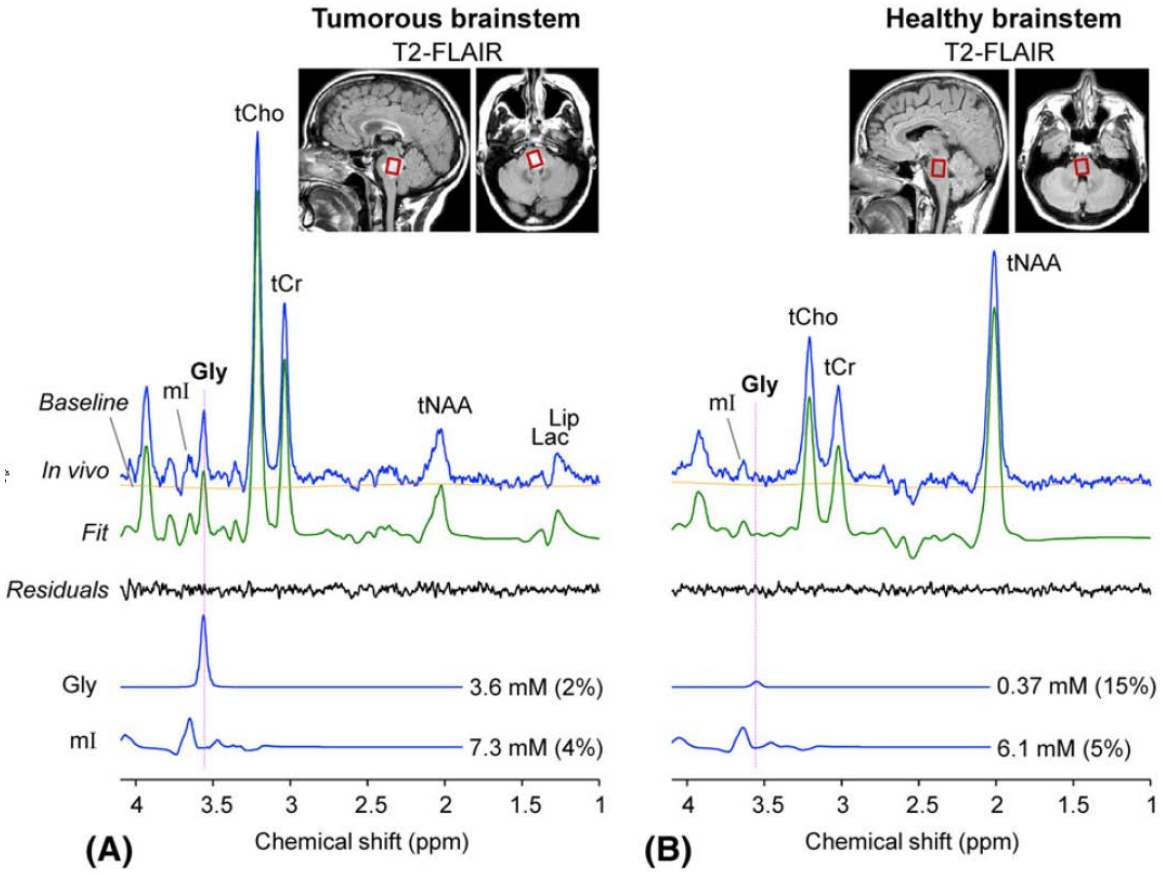

Figure 2.2 In vivo glycine spectra of tumor patient and healthy subject (97)

2.5 LACTATE

Lactate is an end-product of anaerobic glucose metabolism which is elevated in brain tumors due to Warburg effect (*130, 131*). Lactate level in the tumor can be used to predict overall survival of patients and metastases, as shown by several studies (*132-134*). It is also believed that hypoxia induces production of 2HG and thus the correlation between 2HG and lactate may provide valuable information on enzymatic activities inside a tumor cell. For *in vivo* measurement of lactate using ^{1}H MRS, the major lactate signal at 1.31 ppm is hard to detect in the normal brain due to its low concentration (~1mM) and the spectral

overlap with macromolecule signals. Although it is significantly elevated in the tumor, lactate is often difficult to measure precisely because of the overlaps with high lipids signals. Several methods can be used to separate lactate from lipids to improve detectability, including long TE PRESS (TE ≈ 144 ms) (*99, 135*) and spectral editing (*136*).

2.6 OTHERS

Other metabolites have been studied to understand brain tumor metabolism. Glutamate (*105, 137*) and GABA (*138, 139*) are essential neurotransmitters in the brain and have a critical role in gliomas growth. Citrate serves as an intermediate for energy generation and biosynthesis of lipids and related molecules (*140, 141*). Therefore, non-invasive analysis of Cit concentrations using ^{1}H MRS in tumors (*100*) would provide a window into this critical aspect of intermediary metabolism.

CHAPTER THREE

IN VIVO 1D DETECTION OF 2-HYDROXYGLUTARTATE IN BRAIN TUMORS BY TRIPLE-REFOCUSING MR SPECTROSCOPY AT 3T

3.1 INTRODUCTION

Cancers reprogram their metabolism to meet the needs of rapid cell growth (*1, 2*), resulting in alterations in metabolic profiles. The metabolic activity of tumors is predictive of their genetype and may also predict tumor grade and patient outcomes. The majority of World Health Organization grade-2 and grade-3 gliomas and secondary glioblastomas contain mutations in the metabolic enzymes, isocitrate dehydrogenase (IDH) 1 and 2 and the mutations are associated with 2 - 3 times longer patient survival compared to IDH wild-type tumors (*3, 4, 142*). These heterozygous mutations are confined to the active site of the enzyme and result in a neomorphic activity that causes the mutant enzyme to produce an oncometabolite, 2-hydroxyglutarate (2HG), and as a result 2HG, which is normally present in vanishingly small quantities, is elevated by 2 - 3 orders of magnitude in IDH-mutated gliomas (*7, 8, 107*). Noninvasive identification of elevated 2HG therefore has significant clinical utility in patient care.

In-vivo detection of 2HG in patients by ^{1}H MRS at the widely-available field strength 3T was recently reported by several researchers. Among the five non-exchangeable, J-coupled proton resonances of 2HG, the C4-proton resonances at ~2.25 ppm, which are proximate to each other, give rise to a large signal in most experimental situations and may be well detectable using short-TE point-resolved spectroscopy (PRESS) (*89, 90*) and optimized long-TE PRESS (*9, 90, 143*) when the 2HG concentration is relatively high. The C2-proton resonance at 4.02 ppm, which is weakly coupled to the C3-proton spins, can be detected using J-difference editing (*9, 88, 91*), but the small edited signal from a single proton spin

is difficult to assess reliably when the baseline at ~4 ppm is distorted due to the presence of artefactual signals arising from potential subject motion and/or imperfect cancelation of adjacent resonances including water. 2D correlation spectroscopy provides excellent signal separation (*88*), but the sensitivity is low compared to the aforementioned approaches, its applicability likely being limited to cases with high 2HG concentration.

At present, precise evaluation of 2HG at relatively low concentration with abundant signals in the proximity remains challenging at 3T. When targeting the 2HG 2.25-ppm resonance, the major interferences include glutamate (Glu) and glutamine (Gln). The Glu C4-proton and Gln C3-proton resonances (2.35 and 2.12 ppm respectively) can interfere with 2HG estimation extensively when their signals are large compared to 2HG signal. The 2HG and interference resonances are all strongly coupled and consequently the coherences evolve with time in complex manners. For example, the 2HG C4-proton signal is not symmetric with respect to the PRESS subecho times, TE_1 and TE_2 (*9*). This complicated dependence of strongly-coupled resonances on the inter-RF pulse timings can be utilized for manipulating the J-coupled spin coherences for detection of signals of interest. Triple refocusing (90˚ - 180˚ - 180˚ - 180 ˚) has three subecho times and may provide a means of manipulating the J-coupled spin signals more effectively. In this paper, we propose a triple-refocusing sequence for 2HG measurement, whose subecho times and RF pulse duration were tailored, with numerical simulation and phantom validation, for generating a large and narrow 2HG signal at 2.25 ppm and suppressing the Glu, Gln and GABA signals between 2.2 and 2.3 ppm. Preliminary in-vivo data from 15 glioma patients is presented.

3.2 METHODS

Fourteen patients with biopsy-confirmed IDH mutant gliomas and a patient with a lesion in the brainstem (6 males and 9 females; age range 25 - 67, median age of 44 years old) were recruited for the present study. The IDH mutations were all IDH1 R132H, according to immunohistochemical analysis of tumor tissue. The tumor locations included 6 frontal, 5 parietal, 3 temporal, and 1 brainstem. The protocol

was approved by the Institutional Review Board of the University of Texas Southwestern Medical Center. Written informed consent was obtained from patients prior to the scans.

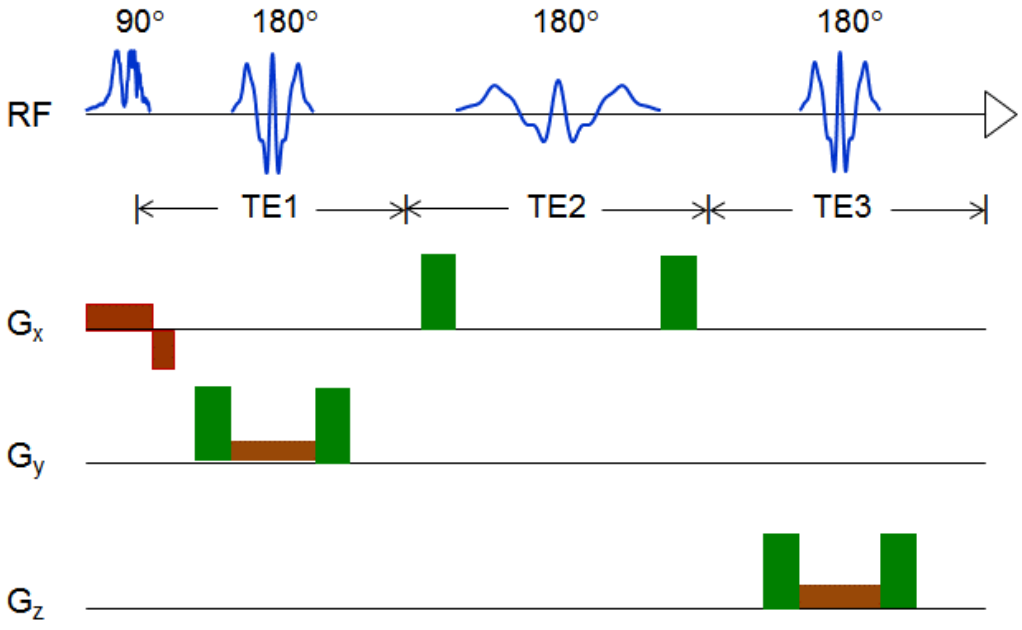

Figure 3.1 Schematic diagram of the triple-refocusing sequence

Density-matrix simulation of 3D-volume localized triple refocusing was carried out to optimize the sequence parameters for detection of the 2HG 2.25-ppm resonance. The time evolution of the density operator was calculated by solving the Liouville-von Neumann equation for the Hamiltonian that included Zeeman, chemical shift and scalar coupling terms, and shaped RF and gradient pulses, using a product-operator based transformation matrix algorithm described in a prior study (*9*). The spatial resolution of slice selection was set to 1%, namely, 0.01 = sample length / number of pixels / slice thickness, where the sample length was two-fold greater than the slice thicknesses with number of pixels (isochromats) of 200. The MRS sequence had three 180˚ RF pulses following a 90˚ excitation RF pulse, as shown in Fig 3.1. The 90˚ pulse and the first and third 180˚ pulses were slice selective while the second 180˚ was non-slice selective. Volume localization RF pulses included a 9.8-ms long 90˚ pulse with bandwidth (at half amplitude) of 4.2 kHz and two 13.2-ms long 180˚ pulses with bandwidth of 1.3 kHz, at an RF field strength (B1) of 13.5 μT, whose envelopes are shown in prior papers (*90, 144*). Spectra of 2HG, GABA, Glu, and

Gln were numerically calculated for various durations of the second 180˚ RF pulse and various subecho time sets (TE1, TE2, TE3). The carrier frequencies of the RF pulses were all set to 2.5 ppm in the simulations. Published chemical shift and J coupling constants were used for the simulations (*70, 145, 146*). The computer simulation was programmed with Matlab (The MathWorks, Inc., Natick, MA).

MR experiments were carried out on a whole-body 3T scanner (Philips Medical Systems, Best, The Netherlands), equipped with a whole-body coil for RF transmission and an 8-channel phased-array head coil for reception. An in-vitro test of the 2HG-optimized triple-refocusing sequence was conducted on a phantom solution with 2HG (8 mM) and Gly (10 mM), at pH = 7.0 and temperature 37□C. Data were acquired, with TR = 9 s and TE = 137 ms, from a 2x2x2 cm3 voxel at the center of the phantom sphere (6 cm diameter). Phantom T2s of 2HG and Gly were evaluated from comparison of experimental and calculated spectra at 10 equidistant TEs between 50 and 500 ms. In-vivo triple-refocused spectra were obtained from tumors identified by T2-weighted fluid-attenuated inversion recovery (T2-FLAIR) imaging. The MRS voxel size was 4 - 10 mL, depending on the tumor volume. MRS acquisition parameters included TR = 2 s, sweep width = 2.5 kHz, number of sampling points = 2048, and number of signal averages (NSA) = 128 - 512. Water suppression was obtained with a vendor-supplied four-pulse variable-flip-angle sub-sequence. First and second order shimming was carried out, using the fast automatic shimming technique by mapping along projections (FASTMAP) (19). A 256-step RF phase cycling scheme, which had 4 orthogonal phases for each of the four RF pulses, was used to minimize potential outer-volume signals. In addition, unsuppressed water was acquired from the voxel for eddy current compensation and multi-channel combination. Unsuppressed water was also obtained with short-TE (13 ms) STEAM and TR = 20 s, for use as reference in metabolite quantification. The RF carrier frequencies of the triple-refocusing sequence were set at 2.5 ppm and were adjusted for B0 drifts in each excitation using a vendor-supplied tool (Frequency Stablization). Surgical cavities, areas of intratumoral hemorrhage, cystic changes, and necrosis, identified on T2-FLAIR anatomical images, were excluded from the tumor voxels.

Spectral fitting was performed with LCModel software (*147*), following apodization using a 1-Hz exponential function. The basis set for the fitting had in-house calculated model spectra of 21

metabolites, which included 2HG, Glu, Gln, GABA, NAA (N-acetylaspartate), tCr (creatine+phosphocreatine), Gly (glycine), mI (myo-inositol), Lac (lactate), GSH (glutathione), Ala (alanine), Ace (acetate), Asp (aspartate), Eth (ethanolamine), PE (phosphorylethanolamine), sI (scyllo-inositol), Tau (taurine), NAAG (N-acetylaspartylglutamate), Glc (glucose), Suc (succinate), tCho (glycerophosphorylcholine + phosphorylcholine). The spectral fitting was conducted between 0.5 and 4.1 ppm. Cramér-Rao lower bounds (CRLB), returned as percentage standard deviation by LCModel, were used to determine the precision of the metabolite estimates. Metabolite concentrations were estimated with reference to water at 48 M for tumors and 40 M for normal-appearing white-matter regions. Relaxation effects on metabolite signals were corrected using published metabolite T2 and T1 values; T2 = 170, 280 and 260 ms for tCr, tCho and tNAA, respectively, and 180 ms for 2HG and other metabolites (*99, 148*); T1 = 1.2 s for 2HG, Glu, Gln and mI, and 1.5 s for other metabolites (*149, 150*). Data are presented as mean ± standard deviation.

3.3 RESULTS

Triple-refocused spectra of 2HG were numerically calculated for ten values of the non-selective (NS), second 180° RF pulse duration (i.e., TpNS180 = 14 - 32 ms with 2 ms increments) and for all possible combinations of subecho times TE1, TE2 and TE3 (2 ms increments for each) for total echo time (TE) between the shortest possible TE and 150 ms (total ~130,000 spectra). The result indicated that the 2HG 2.25-ppm peak amplitude overall increases with TE in a sinusoidal fashion, with temporal maxima at TEs of ~78, ~110 and ~136 ms (Fig. 3.2). The 2HG signal strength and its TE dependence were both very different between TpNS180 values, exhibiting large 2HG signals at TE = ~110 ms when TpNS180 = 14 - 18 ms, and at TE = ~136 ms when TpNS180 = 20 - 32 ms. The spectral pattern of the 2HG 2.25-ppm resonance also depended on TpNS180 and TE. The 2HG multiplet became progressively narrower with increasing T_p^{NS180} and as a result multiplet width at half amplitude was as small as a singlet width for TpNS180° $\geq$ 24 ms, for which the TEs of the signals were all between 130 and 140 ms, with subecho times of TE1 = 26 - 34 ms, TE2 = 82 - 90 ms, and TE3 = 20 - 24 ms. Apparently, long TE and long TpNS180

were preferable for minimizing the interferences from GABA, Glu and Gln (Fig. 3.3). To refine the TpNS180 and the subecho times, spectra of 2HG, GABA, Glu and Gln were calculated for the aforementioned subecho time ranges, with 1 ms increments of subecho times and for TpNS180 = 24, 26, 28, 30 and 32 ms. The Glu C4-proton resonance (~2.35 ppm) was attenuated, giving rise to small signals with various patterns between 2.25 and 2.3 ppm. For Gln, the C3-proton resonance (~2.12 ppm), which was also attenuated, exhibiting signal variations between 2.2 and 2.25 ppm. A triple-refocusing condition was searched for with criteria; 1) high amplitude and small width of the 2HG 2.25-ppm multiplet and 2) small signals of GABA, Glu and Gln between 2.2 and 2.3 ppm. A triple-refocusing scheme for 2HG detection was finalized as TpNS180 = 26 ms and (TE1, TE2, TE3) = (30, 86, 21) ms. In addition, with the same TpNS180 and the same total echo time of 137 ms, we obtained another subecho time set, (TE1, TE2, TE3) = (39, 26, 72) ms, at which the 2HG 2.25-ppm resonance was minimal. The 26-ms 180□RF pulse had a bandwidth of 640 Hz at half amplitude, acting on resonances between 0 and 5 ppm with a carrier frequency of 2.5 ppm.

Figure 3.4a shows the spectra of 2HG, GABA, Glu and Gln, calculated for the 2HG-optimized triple-refocusing sequence. For equal concentrations, the spectral range between 2.2 and 2.3 ppm was dominated by the 2HG and GABA signals, with minimal contributions from Glu and Gln. The Glu and Gln C4-/C3-proton signals, whose amplitudes are greater than the 2HG 2.25-ppm signal at zero TE (i.e., by 1.16 and 1.08 fold), were extensively suppressed, and as a result the Glu and Gln signals between 2.2 and 2.3 ppm were ~3% and ~7% with respect to 2HG, respectively. The GABA 2.29-ppm resonance, which also gives a larger signal (1.29 fold) than 2HG at zero TE, was markedly reduced (2.8 fold), resulting in a smaller signal (82%) than the 2HG signal. The 2HG 2.25-ppm signal yield of the sequence was 56% compared to 90□-acquisition for a localized volume, ignoring T2 relaxation effects. For the 2HG-

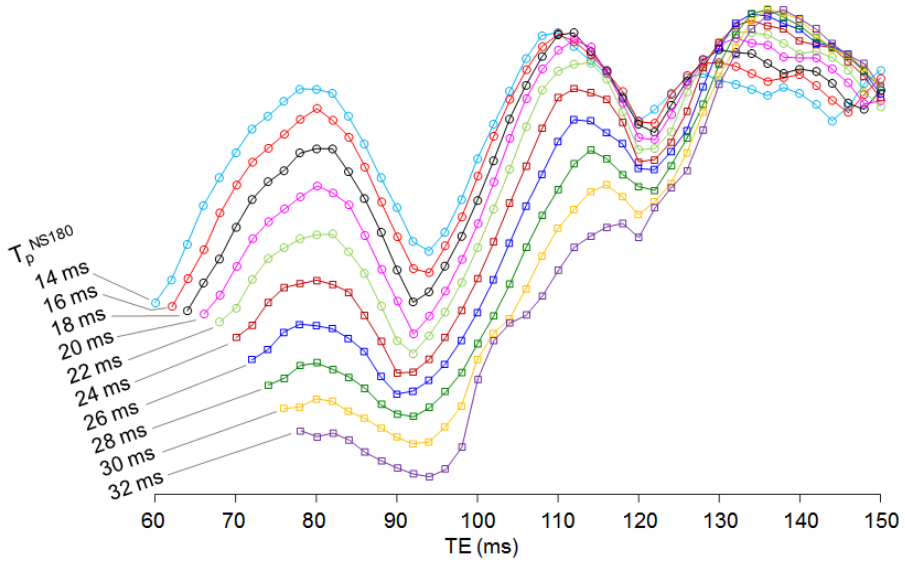

Figure 3.2 TE dependence of numerically-calculated 2HG 2.25 ppm peak amplitude

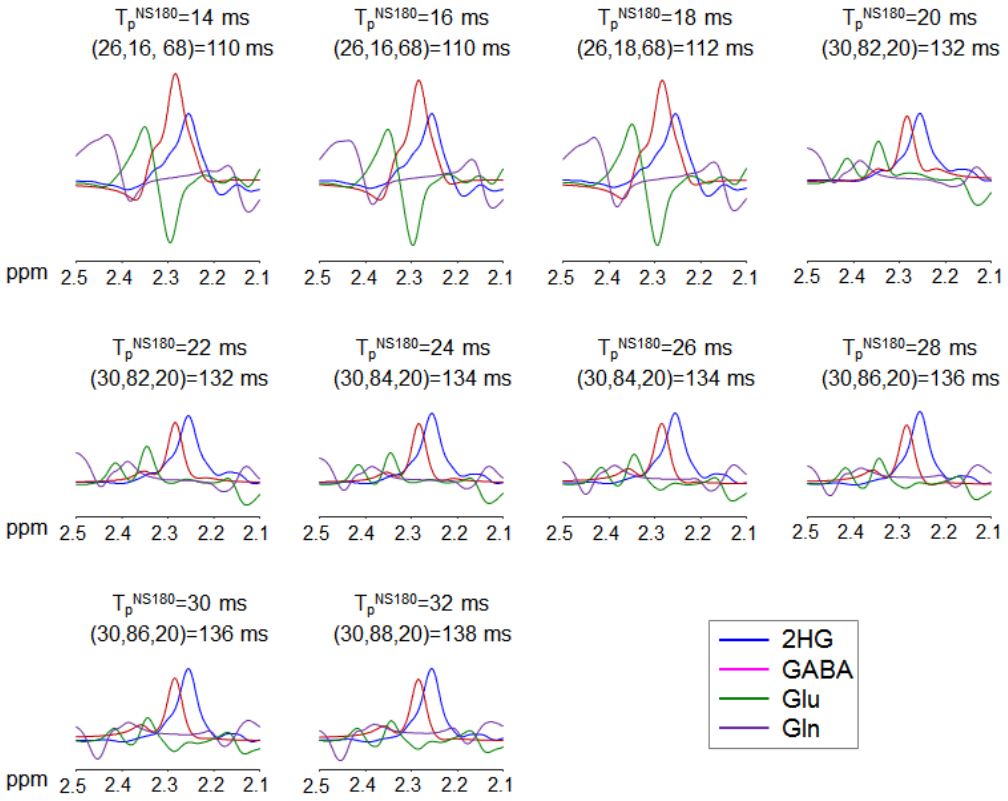

Figure 3.3 Numerically calculated spectra of 2HG, GABA, Glu and Gln

suppressed subecho time set, the 2HG signal was essentially null between 2.2 and 2.3 ppm, in which the GABA signal was dominant (Fig. 3.4b).

We tested the 2HG-optimized and 2HG-suppressed triple-refocusing sequences in a 2HG plus Gly phantom and in an IDH-mutated glioma patient *in vivo* (Fig. 3.5). The calculated 2HG spectra were in excellent agreement with phantom spectra for both triple-refocusing schemes. For the 2HG-optimized sequence, the calculated and phantom spectra both showed a large and narrow 2HG peak at 2.25 ppm, with small signals at ~1.9 and ~4.0 ppm. For a Gly 3.55-ppm singlet linewidth of 5 Hz, the 2HG 2.25-ppm signal width in the phantom spectrum was 5.5 Hz, consistent with the simulation. The experimental 2HG 2.25-ppm peak area was ~73% with respect to the Gly peak area, reproducing the prepared 2HG-to-Gly concentration ratio (8:10), when the phantom T2 effects were corrected (Gly T2 = 1.4 s and 2HG T2 = 0.7 s). For the 2HG-suppressed sequence, the 2HG 2.25-ppm resonance was diminished in the phantom spectrum, as predicted by the simulation. The 2HG signal manipulation by the triple-refocusing schemes was reproduced *in vivo*. In an IDH-mutated oligoastrocytoma patient, a large peak was observed at 2.25 ppm in the 2HG-optimized triple-refocused spectrum, but the 2HG-suppressed triple-refocused spectrum did not present a noticeable signal between 2.2 and 2.3 ppm, indicating that the large peak at 2.25 ppm was attributed to 2HG. The 2HG level in the tumor was estimated to be 15.0 mM, which was the highest among the 14 tumors studied. tCho was quite elevated (4.2 mM) compared to the published normal level from similar regions (~1.5 mM) (25).

Figure 3.6 compares in-vivo spectra from a tumor vs. the contralateral region in a subject with an IDH-mutated oligodendroglioma. 2HG-optimized triple-refocusing spectra were obtained from the tumor mass in the right insula and from a normal-appearing region in the left insula. With identical voxel size (5.8 mM) and scan time (13 min) between the scans, the signal-to-noise ratio and singlet linewidth were similar between the spectra. The overall spectral pattern was different between the spectra due to the differences in metabolite concentrations. The spectrum from the tumor showed slight elevation of tCho and tCr and marked decrease in tNAA, compared to the contralateral. A large signal was present at 2.25

ppm in the tumor spectrum. The 2HG level in the tumor was estimated to be 5.4 mM, with CRLB of 5%.

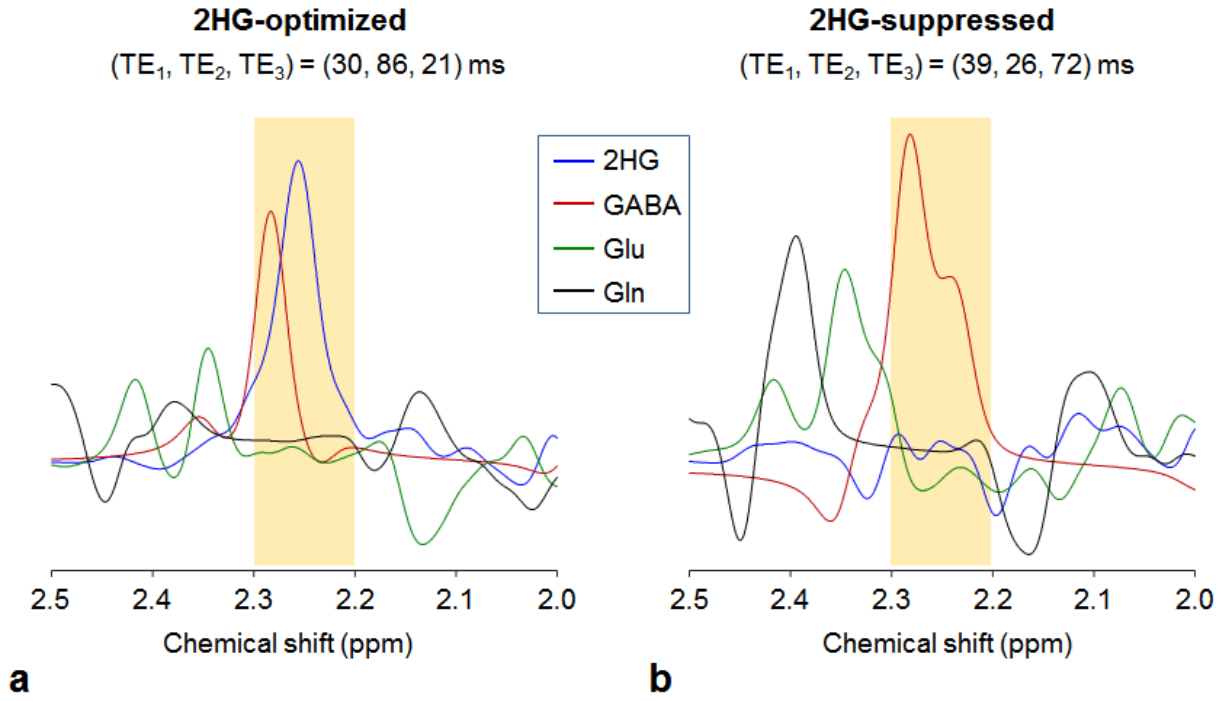

Figure 3.4 Spectra of 2HG-optimized and 2HG-suppressed triple-refocusing sequences

The data from the contralateral voxel did not show evidence of 2HG. GABA was not reliably measurable in the tumor or in the contralateral voxel.

Since the 2HG-optimized triple-refocusing sequence was designed for improving 2HG detectability, we compared its performance with a previously-reported PRESS TE=97 ms method (11) in an IDH-mutated tumor with relatively low 2HG concentration (Fig. 3.7). The metabolite signals were overall smaller in the triple-refocused spectrum than in the PRESS spectrum, largely due to differences in T2 relaxation effects (TE = 137 vs. 97 ms). In the PRESS spectrum (Fig. 3.7b), a signal was discernible at ~2.25 ppm, and the signal was extensively overlapped with a much larger Glu signal at 2.35 ppm. LCModel analysis of the PRESS data resulted in a 2HG estimate of 0.6 mM (CRLB = 61%), with a GABA estimate of 2.3 mM. In the triple-refocused spectrum, the Glu C4-proton resonance was drastically attenuated, giving rise to a clearly discernible signal at 2.25 ppm (Fig. 3.7a). 2HG was estimated to be 2.4 mM with a much smaller CRLB (11%). The GABA estimate was 0.9 mM, which may be slightly lower than normal

similarly to moderate decreases in tNAA and Glu. Albeit the large T2 signal loss the triple refocusing provided improved precision compared to the published long-TE PRESS method, which was largely due to line narrowing of 2HG and suppression of Glu, Gln and GABA resonances.

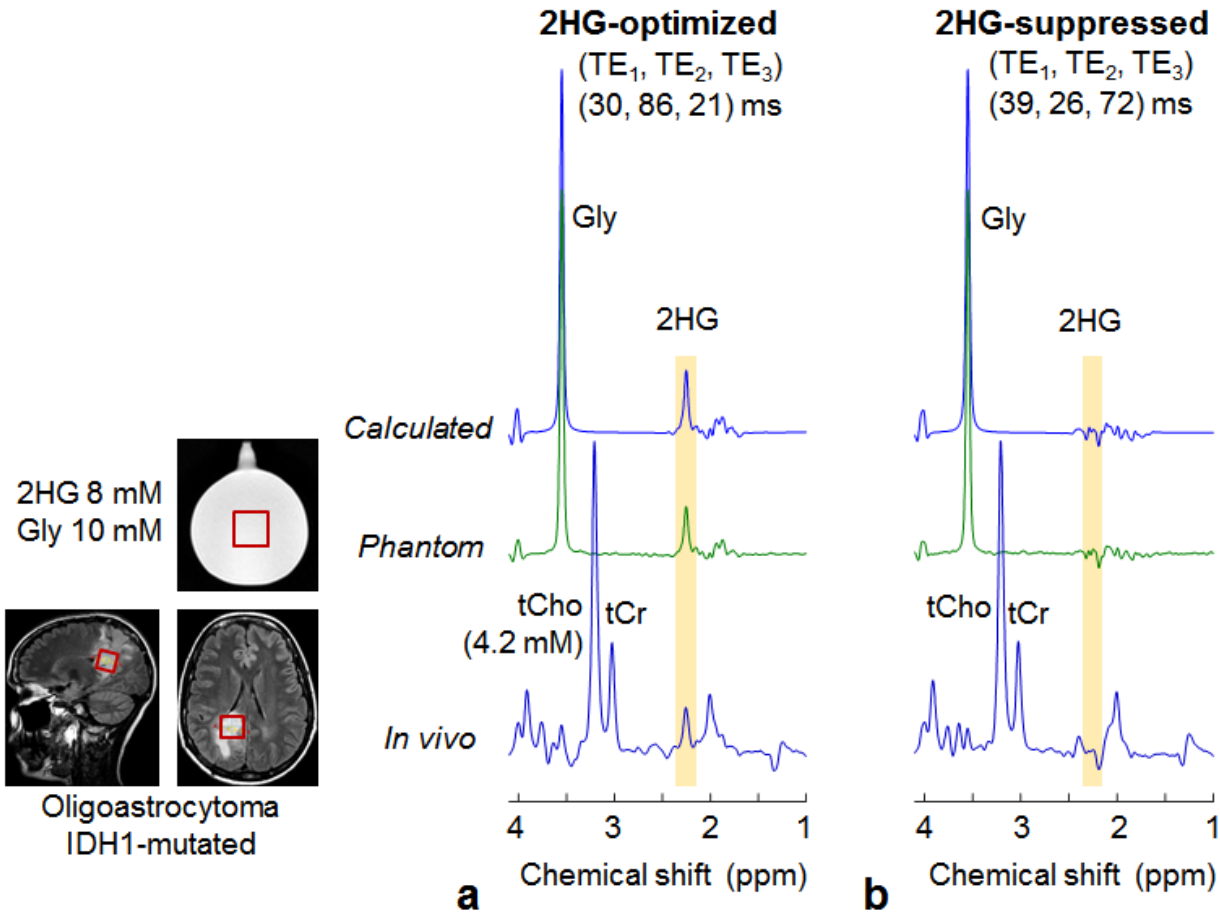

Figure 3.5 Calculated, in-vitro and in-vivo spectra of triple-refocusing sequences

In addition, we tested the 2HG-optimized MRS in a subject with a lesion in the brainstem. The patient did not undergo biopsy and thus the lesion was clinically undefined. A regular clinical MR scan (which had been done independently of the present study) showed increases in tCho and Lac and decreases in tCr and tNAA, which is commonly observed in many tumors. Given that these metabolic alterations also occur in other neurological diseases such as stroke, multiple sclerosis, demyelination, etc, the abnormal levels of those metabolites did not provide useful biological information. Our triple-

refocusing MRS data showed elevated 2HG, indicating the lesion was an IDH-mutated glioma. A 2HG signal at 2.25 ppm was clearly discernible without considerable interferences in the proximity (Fig. 3.8). A composite signal at ~4.05 ppm was well decomposed into 2HG (4.02 ppm) and mI (4.06 ppm) signal in the spectral fitting. The 2HG level was estimated to be 4.7 mM with CRLB of 5%. GABA was undetectable, which was likely due to the decrease of the low-concentration neurotransmitter in the tumor in the white-matter dominant region.

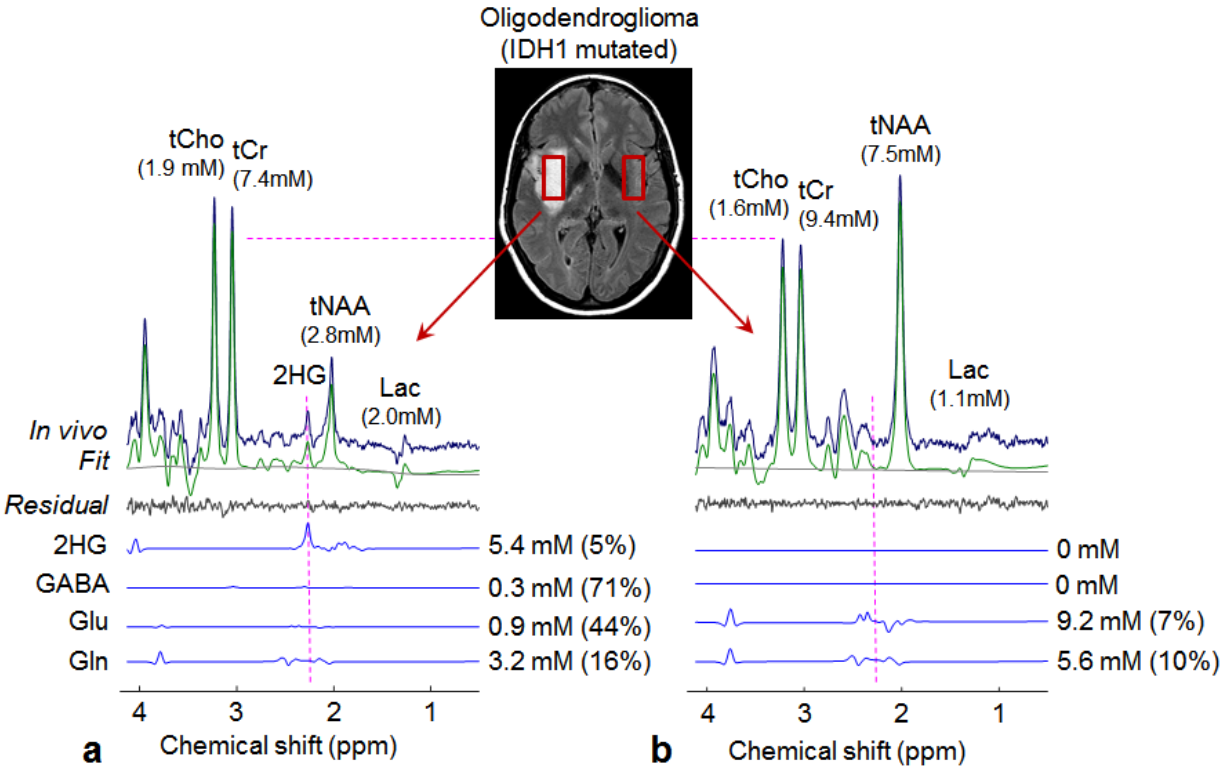

Figure 3.6 In-vivo spectra from an IDH1-mutated oligodendroglioma (a) and the contralateral voxel (b), obtained with the 2HG-optimized triple-refocusing sequence

For the MRS scans in the 15 patients in this study, the mean voxel size was 7.0±2.5 mL, with mean linewidth of the tCho singlet at 6.7±1.7 Hz. With an average scan time of 7.3±2.5 min, the ratio of the tCho peak amplitude to noise was 171±79, where the noise standard deviation was calculated from the spectral region between -5 and 0 ppm. 2HG was measurable in all 14 patients. The estimated 2HG levels ranged from 2.5 to 15.0 mM (mean = 5.5±3.3 mM), with CRLBs between 2% and 11% (mean = 5.7±2.4%).

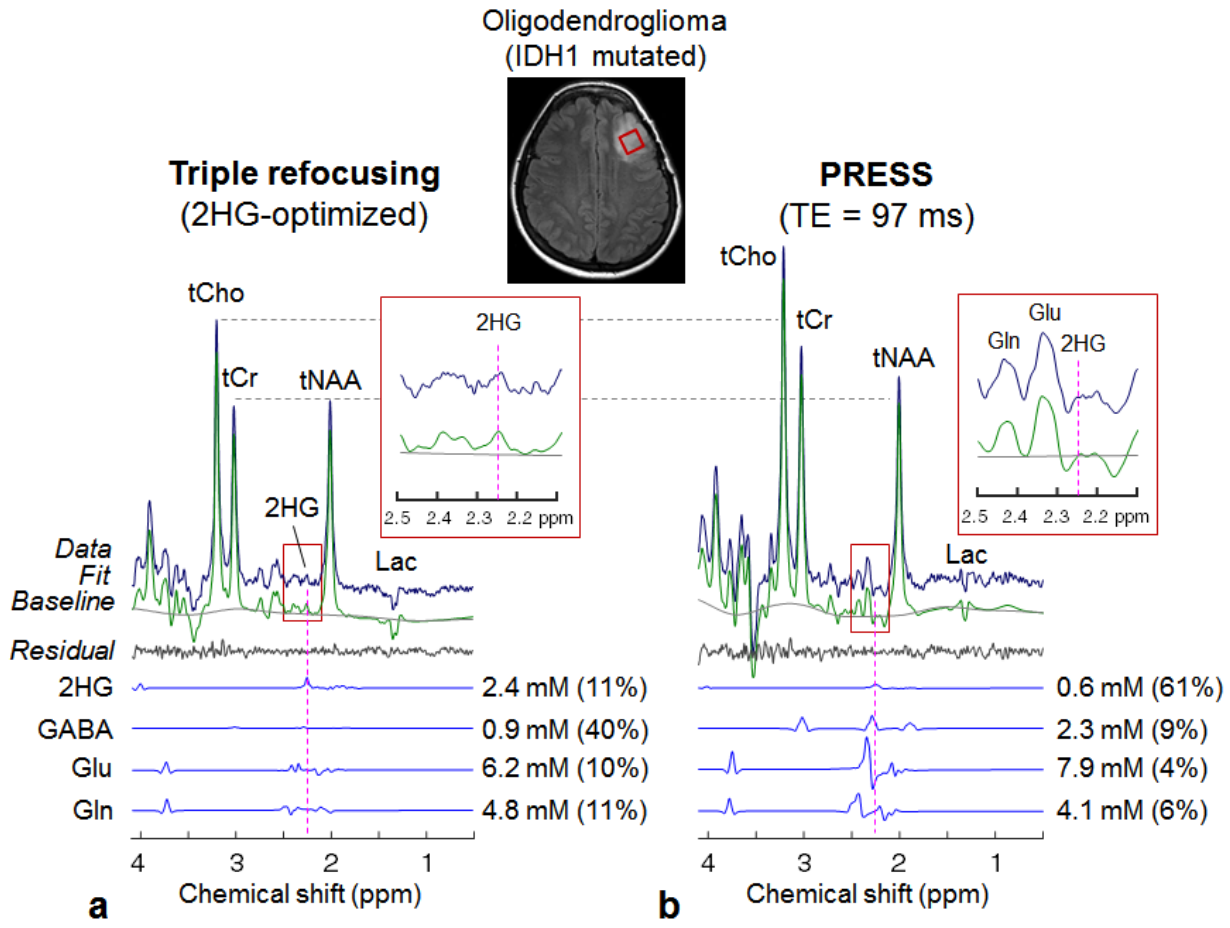

Figure 3.7 In-vivo spectra from an IDH1-mutated oligodendroglioma, obtained with (a) triple refocusing and (b) PRESS TE = 97 ms

The GABA estimation was relatively less reliable. Excluding 3 cases with zero GABA estimates, the mean GABA level was obtained as 0.3±0.2 mM, with mean CRLB of 61±21%. The LCModel-returned correlation coefficient between 2HG and GABA signals ranged from -0.32 to -0.08 (mean = -0.18±0.07). The correlation coefficients of 2HG signal with respect to Glu and Gln were relatively small (i.e., ranging from -0.08 to 0.13 and from -0.08 to 0.17 respectively), which may be due to the Glu and Gln signal suppression. tCho was elevated in all the tumors studied, with a mean level at 3.9±2.4 mM (CRLB = 1% for all). tNAA was substantially decreased (mean = 2.6±2.3 mM). Lastly, we evaluated potential correlation between 2HG and tCho levels in our data set (all with IDH1 R132H mutations). Figure 3.9

presents the 2HG and tCho estimates from the 14 patients with biopsy-confirmed IDH1 R132H mutated gliomas (excluding a brainstem tumor). There was no evidence of significant correlation between the metabolite concentrations (p = 0.28).

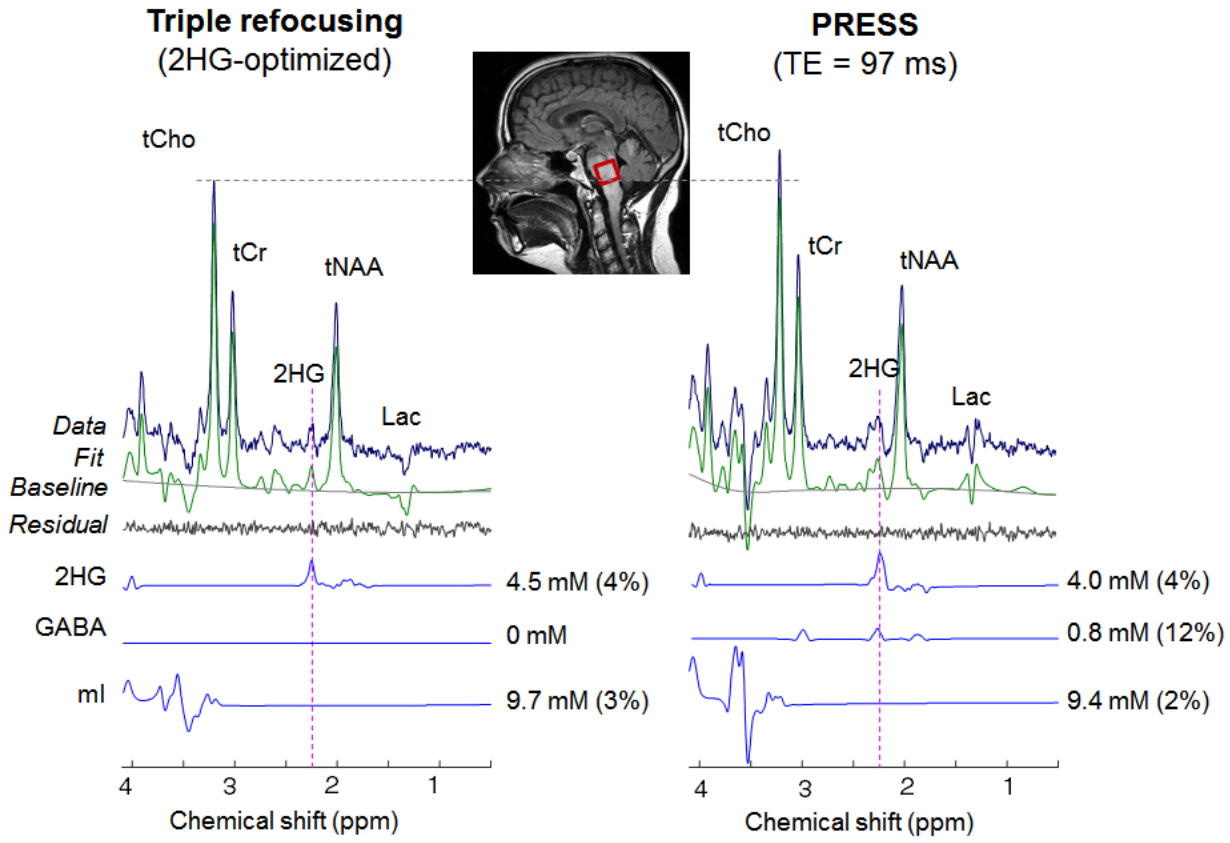

Figure 3.8 An in-vivo triple-refocused spectrum from a brainstem lesion

Benefits from this signal suppression were observed in terms of CRLB and LCModel-returned correlation coefficient, which is a measure of the dependency (or interference) between metabolite signal estimates. For the 14 tumors studied, the mean 2HG CRLB was clearly smaller in triple refocusing than in PRESS TE=97 ms (6% vs. 9%). The correlation coefficients of 2HG with respect to GABA, Glu and Gln ranged from -0.08 to -0.32, -0.08 to 0.13, -0.08 to 0.17 for triple refocusing, and -0.28 to -0.62, 0.18 to 0.42,

-0.11 to -0.22 for PRESS TE=97 ms, respectively. These results indicate that the 2HG-optimized triple refocusing approach provides more reliable estimation of 2HG than the PRESS short- and long-TE methods.

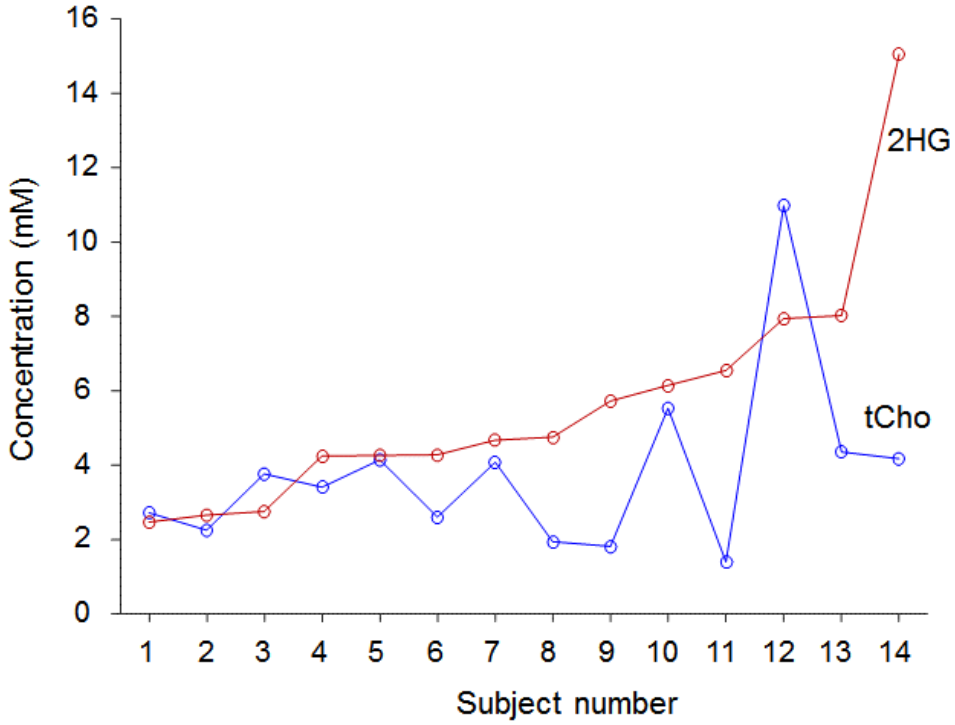

Figure 3.9 The estimated concentrations of 2HG and tCho in 14 glioma patients with IDH1 mutated gliomas

3.4 DISCUSSION

The current paper reports a new triple-refocusing approach for 2HG detection at 3T. Taking advantage of the high variability of J-coupled spin signals with changes of the three subecho times, the signals of 2HG, GABA, Glu and Gln were effectively manipulated for improving the 2HG detectability *in vivo*. With the 2HG-optimized triple-refocusing scheme, considerable line narrowing of the 2HG 2.25-ppm multiplet was achieved with good signal yield. Moreover, the signals of Glu and Gln were extensively suppressed, giving nearly no interferences with 2HG measurement. The GABA 2.29-ppm resonance was also suppressed. Assuming that GABA is decreased in brain tumors similarly to NAA and Glu, the

interference of residual GABA signals with 2HG evaluation may not be considerable. When the GABA 2.29 ppm signal is not negligible compared to the 2HG 2.25 ppm peak, separation of 2HG from GABA may be somewhat achievable by the 2HG 4.0 ppm signal whose intensity is ~40% of the 2HG 2.25 ppm signal.

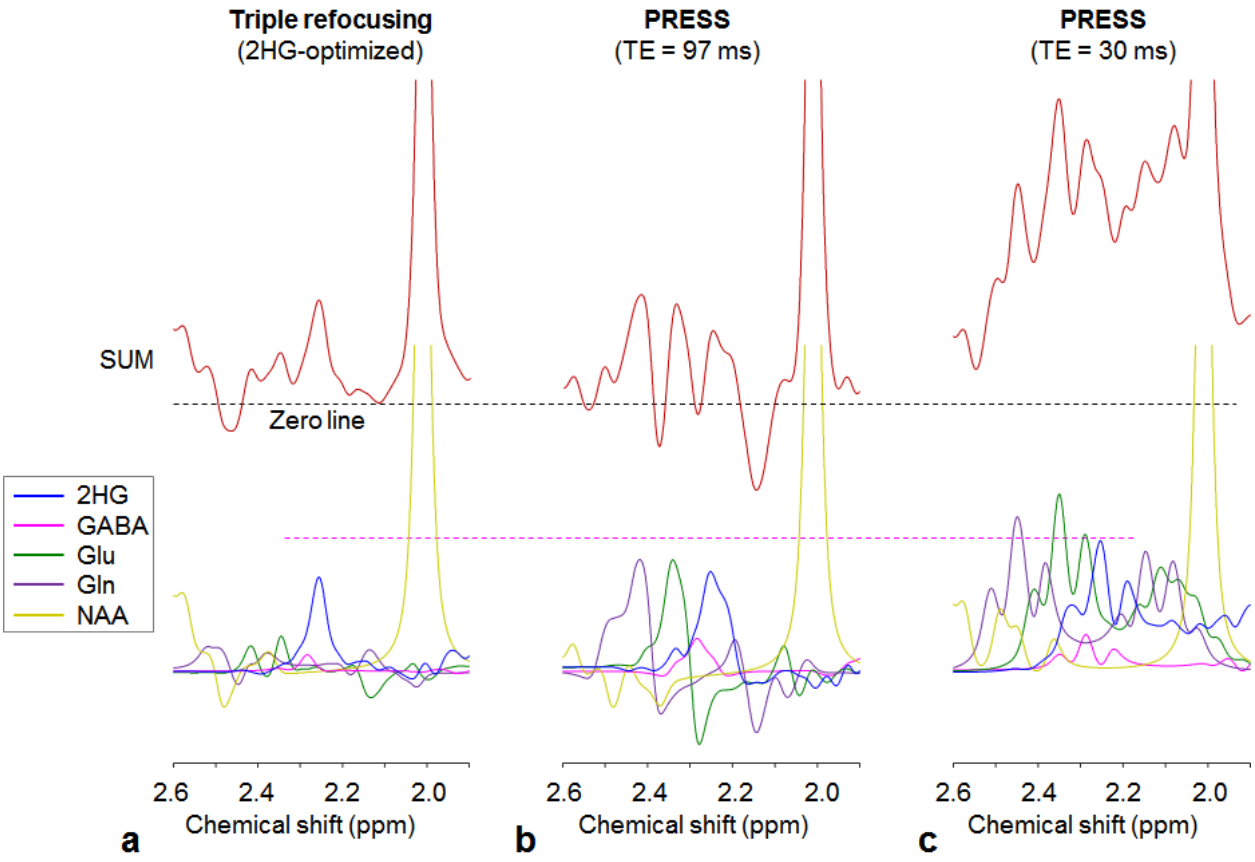

Figure 3.10 Spectra of 2HG, GABA, Glu, Gln and NAA at a concentration ratio of 5:1:5:5:5, numerically calculated for (a) the 2HG-optimized triple refocusing, (b) PRESS TE = 97 ms, and (c) PRESS TE = 30 ms at 3T

Compared to PRESS short-TE (30 ms) and TE=97 ms (9), the 2HG-optimized triple refocusing gives a smaller 2HG 2.25-ppm signal due to the J-coupling effects (Fig. 3.10). The 2HG 2.25-ppm peak amplitude ratio between the triple refocusing, PRESS TE=97 ms, and PRESS TE=30 ms was calculated to be 72:76:100. The signal reduction at the long TEs will be more extensive *in vivo* because of

the T2 relaxation effect. However, high signal selectivity is important for reliable measurement of 2HG. While the signals of 2HG, Glu and Gln are extensively overlapped with each other at short TE, PRESS TE=97 ms provides signal narrowing and consequently improved spectral resolution between 2HG, Glu and Gln (Fig. 3.10b,c). However, this PRESS TE=97 ms does not fully differentiate the 2HG signal from the adjacent resonances and thus 2HG evaluation will be compromised when the Glu and Gln signals are much larger than the 2HG signal (as shown in Fig. 3.7). The triple refocusing provides excellent suppression of these major interference signals between 2.2 and 2.3 ppm and suppression of the GABA 2.29-ppm resonance by ~50% with respect to the PRESS TE=97 ms method (Fig. 2.10a,b). Benefits from this signal suppression were observed in terms of CRLB and LCModel-returned correlation coefficient, which is a measure of the dependency (or interference) between metabolite signal estimates. For the 15 tumors studied, the mean 2HG CRLB was clearly smaller in triple refocusing than in PRESS TE=97 ms (6±2% vs. 9±15%) although the mean 2HG estimate was about the same between the methods (5.4±3.2 vs. 5.5±3.7 mM). The correlation coefficients of 2HG with respect to GABA, Glu and Gln ranged from -0.32 to -0.08, -0.08 to 0.13, -0.08 to 0.17 for triple refocusing, and -0.28 to -0.62, 0.18 to 0.42, -0.11 to 0.22 for PRESS TE=97 ms, respectively. It is noteworthy that the tCho singlet amplitude to noise ratio was about the same between the triple refocusing TE=137 ms and PRESS TE=97 ms (171±68 vs. 172±81) largely due to difference in the tCho singlet line width between the methods (FWHM 6.7±1.7 vs. 7.1±2.0 Hz, $p = 0.02$). Among the 14 IDH-mutated tumors, triple refocusing gave all meaningful 2HG measures while the long-TE PRESS failed in one case (Fig. 3.7). These results indicate that Taken together, the 2HG-optimized triple refocusing approach may provide more reliable estimation of 2HG than the PRESS short- and long-TE methods.

In the present triple-refocusing study, the carrier frequency of the non-slice selective 180□RF pulse (NS180), ν_c^{NS180}, was set to 2.5 ppm throughout the experiments. It is noteworthy that the J-coupled spin metabolite signals following the triple-refocusing sequence is affected by ν_c^{NS180}. For the 26-ms long RF pulse used, the 180˚ action is equally uniform over the 2HG resonances for ν_c^{NS180}= 3.5, 3.0 and 2.5 ppm. The resulting 2HG signal for the 2HG-optimized triple refocusing is quite different between these

carrier frequencies, while the singlet intensity is identical. The 2HG 2.25-ppm signal intensity was calculated to be 81:86:100 for ν_c^{NS180}= 3.5, 3.0 and 2.5 ppm, respectively, ignoring T2 relaxation effects. The overall pattern of the 2HG signal was also influenced by the NS180 carrier frequency. The triple-refocusing scheme used for experiments in this study had an NS180 as the second 180˚ pulse. This triple-refocusing scheme is likely advantageous over the scheme with an NS180 as the first or third 180□pulse. A computer simulation indicated that the 2HG signal is overall smaller and broader in the scheme with an NS180 as the first 180˚ pulse compared to the triple-refocusing sequence of the present study. For the scheme with an NS180 as the third 180˚ pulse, the 2HG signals were similar as in the scheme used for experiments, but with the presence of a non-slice selective RF action at the end of the sequence, the volume localization performance may be low.

There are several pitfalls in the 2HG estimation in the present study. First, due to the use of long TE (137 ms), accurate evaluation of 2HG requires a 2HG T2 value in tumors, which has not been reported to date. Potential 2HG T2 variations between tumors will cause errors in 2HG estimation. Second, use of STEAM water as reference causes some errors because the frequency profiles of the slice-selective 90□ and 180□ RF pulses used were not identical (i.e., transition width / bandwidth ≈ 10% and 12% respectively (*151*)). The discrepancy between the STEAM and PRESS voxel shapes was ignored in this study. Given that water T2 is quite different between tumors (*99*), the errors arising from the profile discrepancy may be smaller than the errors that can be introduced when triple-refocused water signal at the shortest possible TE (~70 ms) is used as reference. Lastly, metabolites were quantified with reference to water at 48 M, which was determined based on proton density images from 7 tumors (data not shown) that showed the tumor water signal higher by 19% than the white-matter water concentration (40 M) (27). Use of a constant water concentration will cause errors in metabolite quantification when the water concentration differs between tumors.

Lastly, our in-vivo 2HG data from IDH1 mutated gliomas did not show significant correlation with tCho, in contrast to a prior *ex-vivo* ^{1}H MRS study (*152*). The tCho elevation was moderate to high in our data, with concentrations ranging from 1.5 to 11 mM. tCho is elevated in brain tumors due to increased

phospholipid metabolism (*113, 114*). Specifically, elevation of tCho in IDH1-mutant gliomas may be attributed to membrane synthesis of mitochondria which is increased to compensate for the utilization of α-ketoglutarate and NADPH for the α-ketoglutarate to 2HG conversion in the cytosol (*115*). IDH wild-type and IDH2-mutated tumors may not exhibit increased mitochondrial number (*115*), but shows marked elevation of tCho, which may be due to rapidly proliferating tumor cells (*113*). Thus increased phospholipid metabolism may not provide definitive identification of IDH1 mutation status, as opposed to a proposal in a pre-clinical 31P MRS study (*114*). Further study is required to find a potential causal relationship amongst phospholipid metabolism, tCho increase, and 2HG production.

3.5 CONCLUSION

2HG is well established as a diagnostic and prognostic imaging biomarker for IDH-mutated gliomas and thus the capability of MRS to analyze this oncometabolite in patients noninvasively has significant relevance in patient care. Diagnostic and prognostic information offered by noninvasive detection of 2HG may significantly impact treatment decision in glioma patients, especially when the tumor is located in the brain region where a biopsy is associated with a risk of permanent neurological injury (e.g., brainstem). This requires precise evaluation of 2HG. Our proposed triple-refocusing method provides a new tool for improved measurement of 2HG with good suppression of adjacent resonances, making it possible to evaluate 2HG in small tumors with low cellularity. Importantly, several therapeutic studies targeting mutated forms of IDH1 and IDH2 (*153*) are currently underway. Reliable measurement of 2HG may also have significant potential for drug development.

CHAPTER FOUR

IN VIVO 2D ECHO-PLANAR SPECTROSCOPIC IMAGING OF 2HG AND OTHER METABOLITES IN GLIOMA PATIENTS WITH DUAL-READOUT ALTERNATED GRADIENTS (DRAG-EPSI) AT 7T

4.1 INTRODUCTION

The majority of World Health Organization (WHO) grade II and III gliomas and secondary glioblastomas harbor isocitrate dehydrogenase (IDH) mutations in cytosol (IDH1) and mitochondria (IDH2), and the mutations are associated with longer survival and better response to therapy compared to IDH wildtype tumors (*3, 4, 142*). The IDH mutation gives rise to NADPH-dependent reduction of α-ketoglutarate to 2-hydroxyglutatrate (2HG), leading to elevation of 2HG by orders of magnitude (*7, 8, 107*). Thus 2HG provides a novel imaging biomarker for identifying IDH mutant gliomas noninvasively. *In-vivo* detection of 2HG was reported in many recent studies, which included single-voxel ^{1}H MRS 3T and 7T (*9, 21, 34, 35, 88-90, 154*) and multi-voxel MRS imaging (MRSI) at 3T (*9, 34, 155*). The spatial resolution in these 2HG imaging studies was relatively low (voxel size ≥ 1.5 mL). Gliomas are highly heterogeneous and infiltrative in malignant transformation. The capability to image 2HG with high resolution rapidly has great potential for patient care and cancer research.

^{1}H echo planar spectroscopic imaging (EPSI) (*156*) has been widely used for fast and high-resolution mapping of brain metabolites at 3T and 4T (*11, 12*). Imaging of J-coupled spin metabolites at these intermediate filed strengths remains challenging largely because of the low signal strengths and spectral overlaps (*13*). Recent studies showed that EPSI at 7T confers significantly improved signal gain and spectral resolution (*18, 157*), but the *in-vivo* applicability in human MR scanners is quite limited due to small spectral widths, insufficient for covering the spectral regions of interest (*14*).

Several EPSI approaches were proposed for data acquisition and reconstruction. First, odd/even echo editing was conventionally used for neuro-metabolic imaging at 1.5T, 3T and 4T (*11-14*).

The echo editing results in a halved spectral width with respect to the acquisition dwell time. Second, the interlaced Fourier transformation approach maintained the full spectral width (*15, 16*), but this was achieved ignoring the prevailing gradient delay artifacts. Third, a dual-readout EPSI with flyback gradients (*158*) was proposed to increase the spectral width. Data acquired using two sets of interleaved readout gradients with flyback gradients were combined to a single set of data, leading to a spectral width greater by two fold with respect to the acquisition dwell time. This approach was used recently for brain tumor metabolic imaging at 7T, with in-plane resolution of 10×10 mm^2 (*18*). Lastly, time-shift EPSI was proposed for increasing spectral width (*20, 159*).

In this paper, we propose a new EPSI approach, which was designed from the conventional bipolar readout gradient and dual-readout approaches. Taking advantage of the two published schemes, this new method provides increased spectral width, high signal-to-noise ratio (SNR), and small burden on the gradient system, compared to the published EPSI methods. The new EPSI scheme, combined with our previously-reported 2HG-optimized MRS sequence (*21*), is demonstrated for high-resolution imaging of 2HG and other metabolites at 7T. Following phantom validation of the performance, preliminary data from five brain tumor patients are presented.

4.2 THEORY

Conventional EPSI: In conventional EPSI, data acquisition may undergo using an alternated-gradient readout with a dwell time of Δt, as shown in Figure 4.1A. The data acquired during the positive- and negative-polarity gradients are separated into odd- and even-echo sets and each data set is processed for eddy current compensation and phase correction. The two sets of data may then be averaged to improve SNR. Ghost artifacts due to asymmetries in gradient switching can be removed with the odd/even echo editing (*53*). The dwell time of the reconstructed data is twice ($2\Delta t$) the acquisition dwell time, resulting in spectral width of $1/(2\Delta t)$. The spectral width of this conventional EPSI in human MR scanners is typically about 1 kHz (*12, 14*), which is ~3.3 ppm at 7T.

Dual-readout alternated gradients EPSI (DRAG-EPSI): Figure 4.1B depicts a new EPSI readout scheme. The scheme consists of two sets of readouts; one using the conventional alternated-gradient and the other using a polarity-reversed gradient. The data are then sorted into two data sets according to the gradient polarity (*i.e.*, positive-gradient data and negative-gradient data). Following eddy current compensation and phase correction, the two sets of data are averaged, leading to a set of EPSI data with spectral width of $1/\Delta t$, greater by 2 fold compared to conventional EPSI.

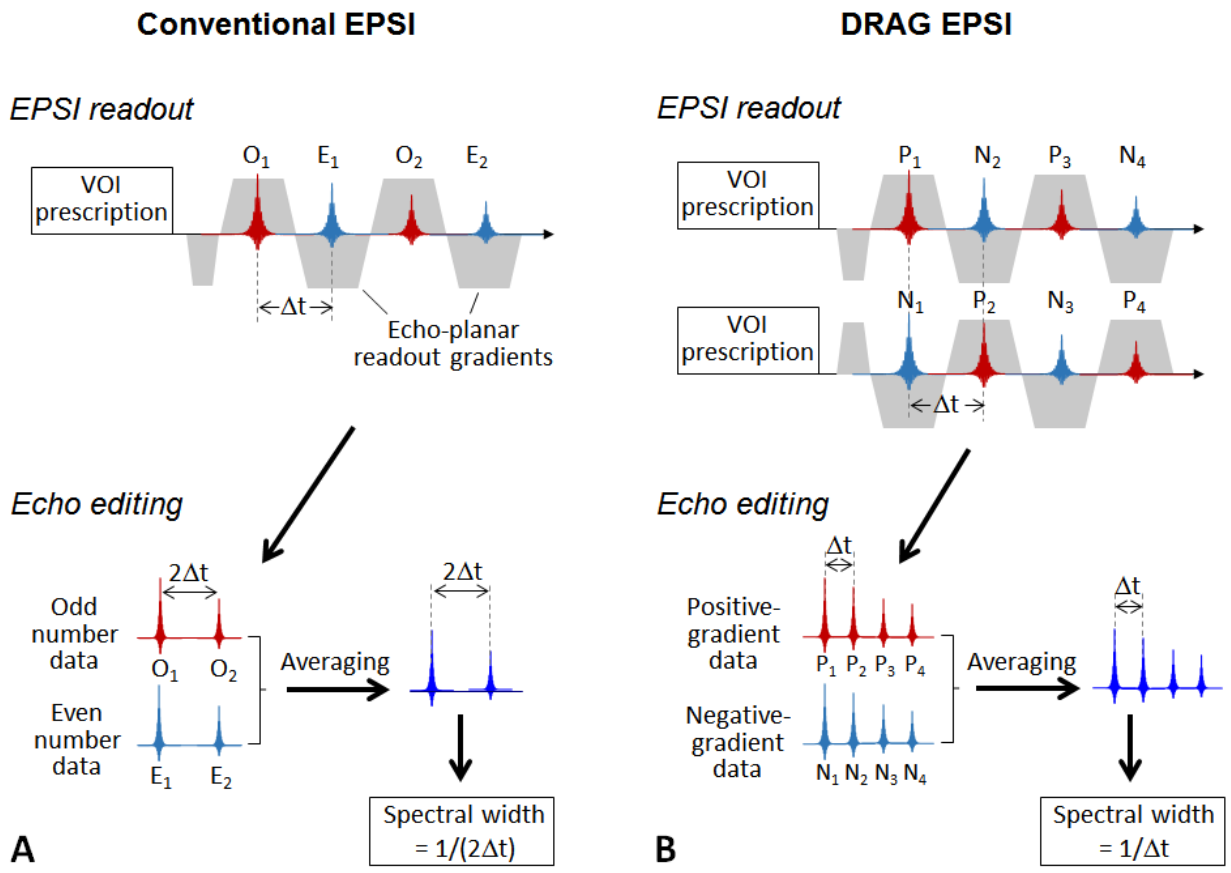

Figure 4.1 (A) Conventional EPSI and (B) Newly-designed EPSI readout scheme

4.3 METHODS

MR experiments were carried out in a human whole-body 7T MR scanner (Philips Medical Systems, Cleveland, OH) using a quadrature transmit (4 kW RF amplifier) and 32-channel receive head coil (Nova Medical, Wilmington, MA). The gradient system offered maximum amplitude of 40 mT/m, with maximum slew rate of 200 mT/m/ms. *In-vitro* MRSI experiments were performed in a GE braino phantom (10 cm diameter) and a 6-cm diameter spherical phantom with 2HG (10 mM) and Gly (20 mM). The phantom scans included conventional phase-encoded MRSI, conventional EPSI, and DRAG-EPSI.

Five glioma patients were enrolled, who included a 60-year old male with IDH1-mutated grade-II oligodendroglioma (Patient 1), a 47-year old female with IDH1-mutated grade-II oligodendroglioma (Patient 2), a 58-year old male with IDH1-mutated grade-II oligoastrocytoma (Patient 3), a 50-year old male with radiographically-suggested glioma (Patient 4), and a 40-year old male with IDH wildtype glioblastoma (Patient 5). Other than Patient 4, the four patients had biopsy or surgery after the

MR scans, from which the tumor type and IDH mutational status were obtained. MR scans were conducted prior to chemotherapy and/or radiation treatments.

2D MRS imaging was obtained with 1D imaging by DRAG-EPSI (Figure 4.1B) and another 1D imaging using phase encoding gradients. DRAG-EPSI was preceded by prescription of a volume of interest (VOI) using our previously-reported 7T 2HG-optimized PRESS sequence (*21*), which had the RF pulse envelopes of our 3T 2HG MRS study (*90*). The PRESS sequence included an 8.8 ms 90° RF pulse (bandwidth 4.7 kHz) and two 12 ms 180° RF pulses (bandwidth 1.4 kHz) at RF field intensity (B_1) of 15 μT. The echo-planar readout gradient consisted of 512 alternating trapezoidal gradients with amplitude of 9.5 mT/m and slope of 90 mT/m/ms (slope length of 105 μs and plateau length of 400 μs). The data of opposed-polarity readouts were acquired in an interleaved fashion. The spectral width of the DRAG-EPSI was 1638 Hz (5.5 ppm at 7T). Flip angle calibration was performed on the PRESS-prescribed VOI using a vendor-supplied T_1 insensitive double-stimulated-echo method (*160*). Water suppression was obtained with VAPOR (variable power and optimized relaxation delays). Up to second order B_0 shimming was carried out on the VOI using a vendor-supplied tool. Water-suppressed DRAG-EPSI was acquired with the following parameters: PRESS TE = 78 ms (TE_1 = 58 ms and TE_2 = 20 ms), TR = 2 s, field of view = 198×180 mm^2, slice thickness = 14 mm, spatial resolution = 0.5 mL (6×6×14 mm^3), data matrix size = 33×30×512, and number of signal averages = 16. The scan time was 16 min, of which 8 min was spent for each of the two readouts. Depending on the tumor size, the VOI ranged from 60×60 to 90×90 mm^2. Unsuppressed-water imaging data were acquired with VOI prescription by TE 78 ms PRESS using DRAG-EPSI and by TE 13 ms STEAM using conventional EPSI (scan times of 2 and 1 min respectively). T2w-FLAIR (T2-weighted fluid attenuated inversion recovery imaging) was acquired for tumor identification (TR/TE/TI = 11,000/93/2800ms; field of view = 230×230 mm^2; slice thickness of 5 mm; 20 transverse slices). B_1 map was obtained using a dual flip angle method (*17*).

The 2D k-space data was zero filled to 66×60 matrix and subsequently apodized with a 2D Hamming function. The time domain data was zero-filled to 2048 points and apodized with a 3 Hz exponential function. Eddy-current compensation and multi-channel combination were conducted, with in-house computer scripts, using the unsuppressed PRESS DRAG-EPSI water as reference, after which the interleaved data were summed without additional phase correction. About 10% of the spectra in the margin of VOI were discarded in subsequent analyses, which had the chemical-shift displacement effects arising from the use of PRESS 180º RF pulses with 1.4 kHz bandwidth. Spectral fitting was performed between 1.0 and 3.85 ppm, with LCModel software, using in-house calculated basis spectra of 14 metabolites, which included 2HG, Glu (glutamate), Gln (glutamine), NAA (N-acetylaspartate), tCr (creatine + phosphocreatine), Gly (glycine), mI (myo-inositol), GSH (glutathione), Ace (acetate), Lac (lactate), Asp

(aspartate), sI (scyllo-inositol), NAAG (N-acetylaspartylglutamate), tCho (glycerophosphorylcholine + phosphorylcholine). The metabolite signal estimates from LCModel were normalized to the unsuppressed TE 13 ms STEAM water for individual voxels, which was to correct for potential B_{1+} and B_{1-} variations, and subsequently the metabolite concentrations were calculated by scaling the normalized metabolite signal estimates with reference to tCr in normal-appearing gray-matter region at 8 mM. Metabolite estimates with CRLB > 20% were discarded, similarly as in prior EPSI studies (*11, 18, 155*). Paired t-test was performed for comparison of metabolite estimates between tumor and contralateral regions, with Bonferroni correction, using SAS software version 9.3 (SAS Institute, Cary, North Carolina). Data are presented as mean ± standard deviation (SD).

4.4 RESULTS

The imaging performance of DRAG-EPSI was compared with conventional phase-encoded MRSI and conventional EPSI in a GE Braino phantom (10 cm diameter). VOI prescription was obtained with TE 78 ms PRESS for all imaging scans. The result is presented in Figure 4.2, together with the spatial resolution (15×15 mm^2), scan time (7 min) and spectral widths of the scans. The intensity and pattern of metabolite signals were in excellent agreement between the three methods, but SNR was notably different between the methods, as shown in NAA SNR maps. Compared to phase-encoded MRSI, the NAA SNR was 60% and 51% for DRAG-EPSI and conventional EPSI respectively, in good agreement with theoretical values that were calculated from the plateau period and ramp time of the readout gradients (*158*). Also, we compared the DRAG-EPSI performance with conventional phase-encoded MRSI for a higher resolution (6×6 mm^2), which was the same resolution as in our *in-vivo* study. The readout gradients and consequently the spectral width of DRAG-EPSI were also same as in the *in-vivo* study. The data is shown in Figure 4.3. With the high-resolution imaging, both methods showed fairly uniform metabolite signals inside the phantom, without considerable signals from outside the phantom. Compared to the 15×15 mm^2 resolution case, the NAA SNR in DRAG-EPSI was increased to 81% with respect to phase-encoded MRSI, which was due to the longer plateau period of the readout gradients. The overall spectral pattern and signal strength were both essentially identical between DRAG-EPSI and phase-encoded MRSI.

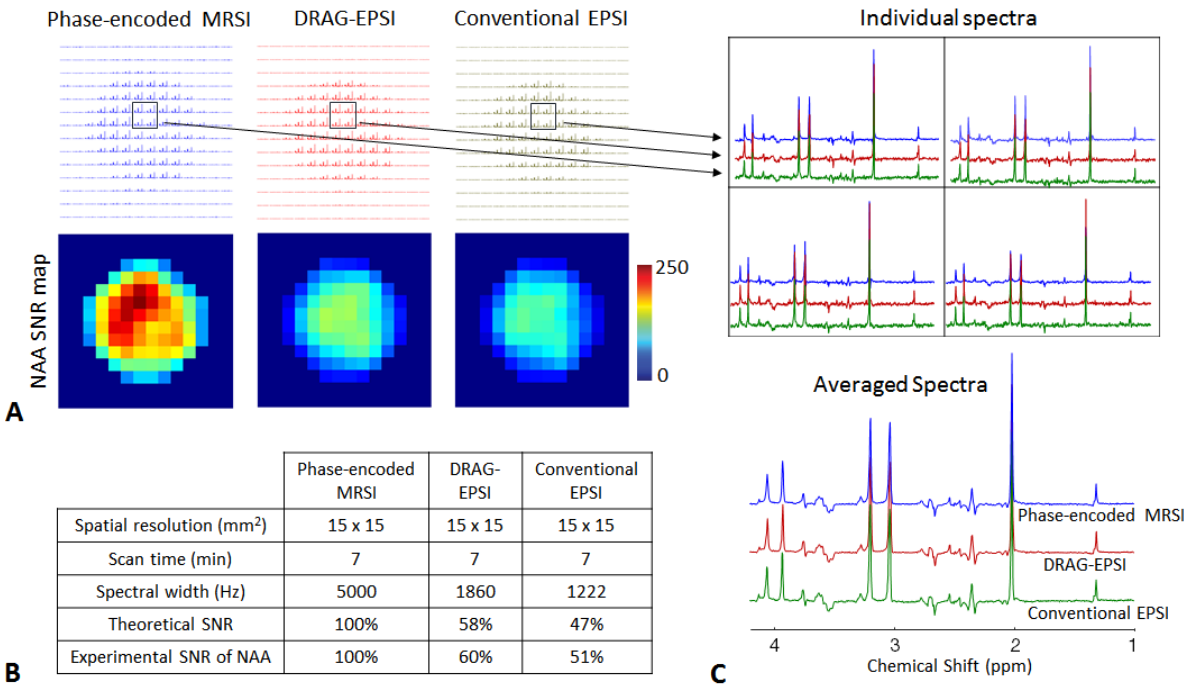

	Phase-encoded MRSI	DRAG-EPSI	Conventional EPSI
Spatial resolution (mm^2)	15 x 15	15 x 15	15 x 15
Scan time (min)	7	7	7
Spectral width (Hz)	5000	1860	1222
Theoretical SNR	100%	58%	47%
Experimental SNR of NAA	100%	60%	51%

B

Figure 4.2 Comparison between conventional phase-encoded MRSI (blue), DRAG-EPSI (red) and conventional EPSI (green) in a GE Braino phantom (10 cm diameter) at 7T

We evaluated potential B_0 drifts induced by the readout gradients of DRAG-EPSI and conventional EPSI in a phantom (6 cm diameter sphere). In each of the EPSI scans, 30 images were acquired, with scan time of 1 min for each image. Figure 4.4 presents the result, together with readout gradient parameters of the scans, which were set for equal resolution (6×6 mm^2). The frequency drift was increased with time in each of the methods, but the drift was much smaller in DRAG-EPSI than in conventional EPSI. The average drifts over the voxels within the phantom in DRAG-EPSI and conventional EPSI were measured as 0.12±0.16 Hz and 1.00±0.16 Hz at 16 min, and 0.38±0.17 Hz and 1.64±0.21 Hz at 30 min, respectively.

The performance of DRAG-EPSI for 2HG detection was tested in a 6-cm diameter spherical phantom with 2HG (10 mM) and Gly (20 mM). The result is shown in Figure 4.5. The spectra of individual voxels showed fairly uniform Gly peaks across the VOI. With the use of PRESS TE 78 ms (TE_1 = 58 ms and TE_2 = 20 ms), the J-coupled C4-proton resonances of 2HG exhibited a negative-polarity signal at 2.25 ppm while the C3-proton signals between 1.8 and 2.0 ppm were diminished. When displayed for 1.8 - 2.4 ppm, the 2HG C4-proton signal was apparently uniform within the VOI. Spectral fitting by LCModel

reproduced all spectra well. The 2HG-to-Gly ratio was estimated to be 0.49±0.02 within the phantom, reproducing the prepared concentration ratio of 1/2. The maps of 2HG and Gly estimates showed fairly uniform estimates within the phantom, giving coefficient of variation of 2HG and Gly estimates at 3.7% and 4.2% respectively.

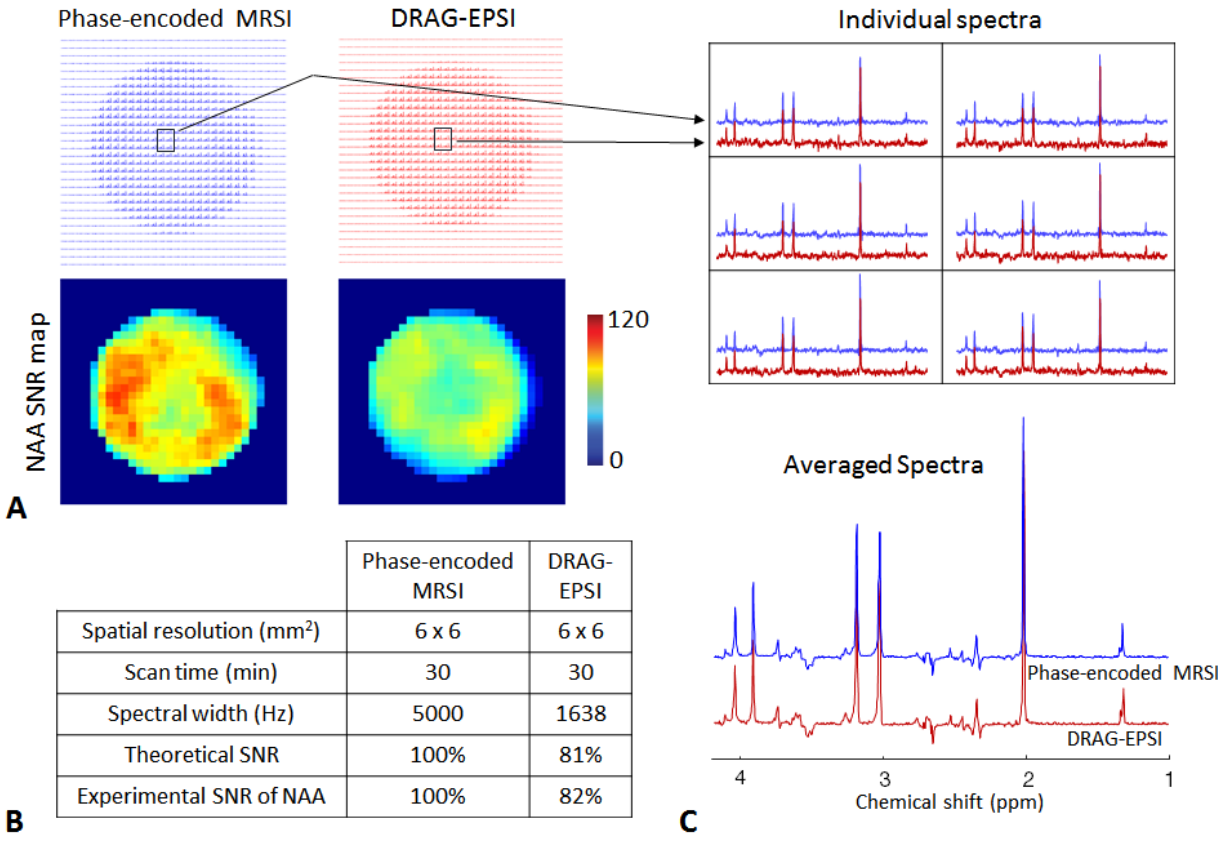

	Phase-encoded MRSI	DRAG-EPSI
Spatial resolution (mm²)	6 x 6	6 x 6
Scan time (min)	30	30
Spectral width (Hz)	5000	1638
Theoretical SNR	100%	81%
Experimental SNR of NAA	100%	82%

Figure 4.3 Comparison between conventional phase-encoded MRSI (blue) and DRAG-EPSI (red) in a GE Braino phantom at 7T at high resolution

The DRAG-EPSI method was used for imaging 2HG in five glioma patients (3 IDH mutated, 1 unknown IDH mutational status, and 1 IDH wildtype). Figure 4.6 shows the data from a patient with IDH1 mutant oligodendroglioma (Patient 1). T2w-FLAIR identified a solid tumor mass in the left frontal region. VOI was set at 60×60 mm^2, which included the tumor and contralateral volume. The RF field intensity was fairly homogeneous within the VOI (see B_1 map). The coefficient of variation (CV = SD/mean) of B_1 within the VOI was 6.2%. The signals of NAA, tCr and tCho were uniform outside the tumor region. The spectra from the tumor (upper right region within VOI) were dominated by increased tCho signals. An inverted peak was clearly discernible at 2.25 ppm in spectra from the tumor (see the

spectrum from location B), which should be attributed to 2HG given that the adjacent signals of Glu, Gln and GABA are all positive at the PRESS echo-time condition (*21*). 2HG was estimated to be up to 5 mM in the tumor and was undetectable in the normal-appearing regions. The metabolite maps showed increase in tCho and decreases in NAA and tCr.

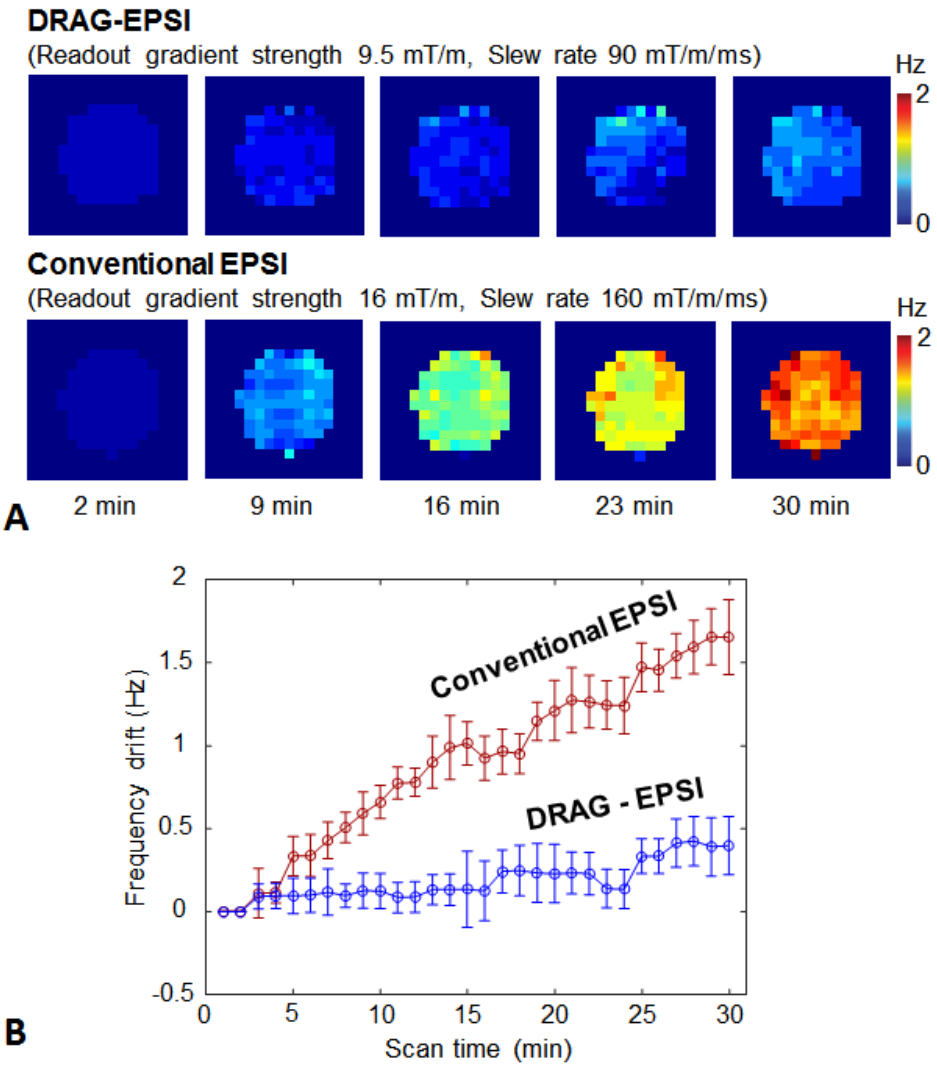

Figure 4.4 Comparison of frequency drifts with time in DRAG-EPSI vs. conventional EPSI

Data from another subject with IDH1 mutant oligodendroglioma is presented in Figure 4.7. A tumor mass was identified in the right parietal region. The CV of B_1 within VOI was 6.6%. Many spectra within the tumor left-top to right-down exhibited relatively small metabolite signals, indicating that the region may be largely cystic. 2HG was clearly detectable with CRLB < 10% in most of the spectra from the tumor. The center of the tumor mass (location C) showed high 2HG (4.6 mM, CRLB 6%) and the right upper part of the tumor (location A) showed somewhat lower 2HG (3.1 mM, CRLB 6%). In contrast, the

tCho level in this tumor was lower than normal (see tCho map). The tCho level was as low as 0.7 mM in the tumor (see spectrum from location C), quite lower than the levels in the normal-appearing brain regions (~1.5 mM; see spectra from locations B and D). With reduction of NAA in tumors, the tCho/NAA ratio was higher in the tumor than in contralateral (0.5 - 0.7 *vs.* ~0.1).

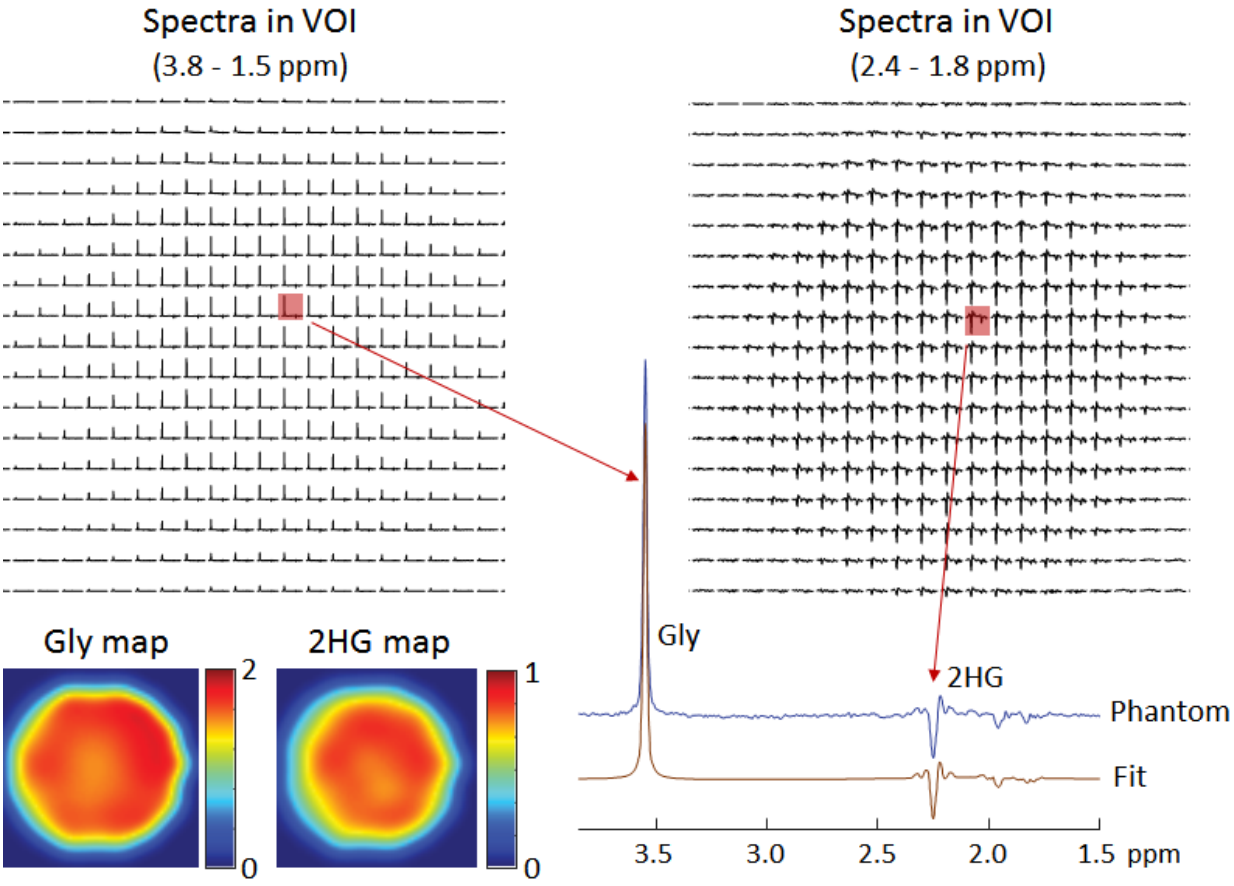

Figure 4.5 In vitro validation of DRAG-EPSI at 7T, with by TE 78 ms PRESS

For the five patients of the present study, we calculated the mean value and SD of B_1 within VOI. The coefficient of variation (CV) of B_1 was 3.8, 5.3, 6.2, 6.6 and 7.3%, giving a mean CV of 5.8±1.4%. The CV of B_0 was estimated to be 2.5, 3.6, 6.6, 13 and 16 Hz in the patients, with a mean CV at 8.3±5.9 Hz. For each of the five patients, the estimated concentrations of seven metabolites were averaged over the tumor volume and the normal-appearing contralateral volume. The result is shown in Figure 4.8. 2HG was detectable in the three patients with biopsy-proven IDH mutant tumors (3.0±0.9, 3.3±0.4 and 2.3±0.6 mM in Patients 1, 2 and 3 respectively). 2HG was also clearly detected in a subject with radiographically-suggested glioma (2.3±0.2 mM in Patient 4), indicating this tumor may be an IDH mutant glioma. For these four tumors, the 2HG estimate difference between tumor and contralateral was significant ($p < 0.001$).

In contrast, 2HG was undetectable in Patient 5, indicating that the lesion had wildtype IDH. After the MRS scan, the patient underwent a surgery and the lesion was found to be a primary glioblastoma, in which the incidence rate of IDH mutation is very low (< 5%) (*3*, *4*). In four tumors other than Patient 2, the tCho level was estimated to be higher in tumors than in contralateral. The concentration of NAA was significantly lower in tumor than in contralateral brain in all cases. For Glx (Glu+Gln), the concentration was significantly lower in tumor tissue than in contralateral brain in Patients 1, 2 and 3, but significantly elevated in the glioblastoma (Patient 5) (Gln ~8 mM and Glu ~3 mM).

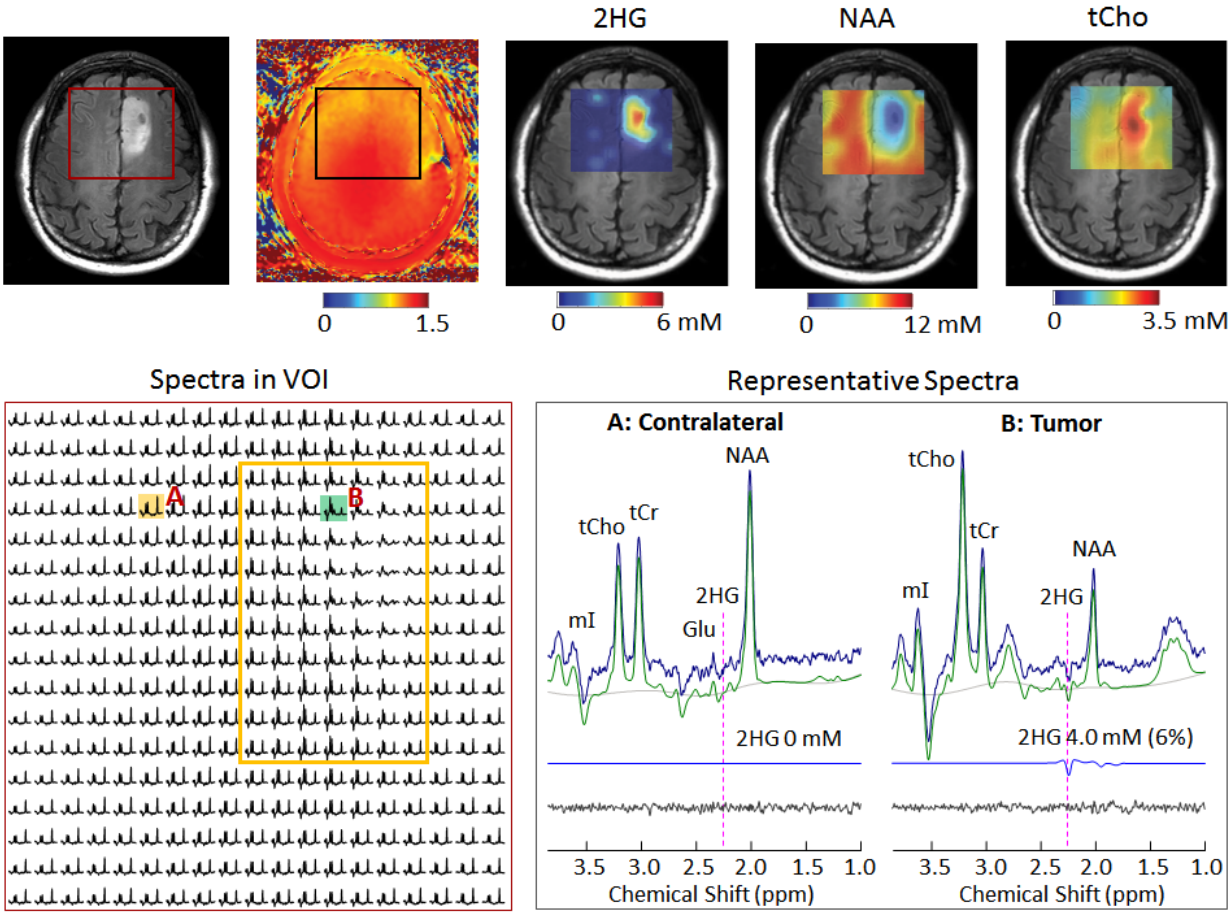

Figure 4.6 In vivo 2D DRAG-EPSI data from a patient with IDH1-mutated grade-II oligodendroglioma at 7T

4.5 DISCUSSION

We present high-resolution imaging of 2HG and other metabolites in brain tumor patients at 7T, achieved using a newly-designed EPSI scheme (DRAG-EPSI). To our best knowledge, this is the first report of *in-vivo* 7T imaging of 2HG in brain tumor patients, obtained with 6×6 mm^2 in-plane resolution.

A spectral width of 1638 Hz was achieved with relatively low gradient strengths. This spectral width with 6×6 mm^2 in-plane resolution was not achievable using conventional EPSI even when the slew rate was maximized to 200 mT/m/ms in our 7T MR scanner, which may cause coil overheating and high acoustic noise and consequently can aggravate data quality and patient compliance (*161*). However, DRAG-EPSI allowed to use a readout gradient strength of 9.5 mT/m and a slew rate of 90 mT/m/ms, enjoying a decrease of acoustic noise level from 120 dB (conventional EPSI) to 80 dB (DRAG-EPSI), as measured with a microphone placed inside the magnet. In addition, it is noteworthy that the data processing in DRAG-EPSI is relatively straightforward. Since the data acquisition time points are identical between the positive and negative gradient data, these interleaved data can be directly summed following the eddy-current compensation using the DRAG-EPSI water data, without need of first-order phase correction, which may be required in time-shift EPSI (*20, 159*).

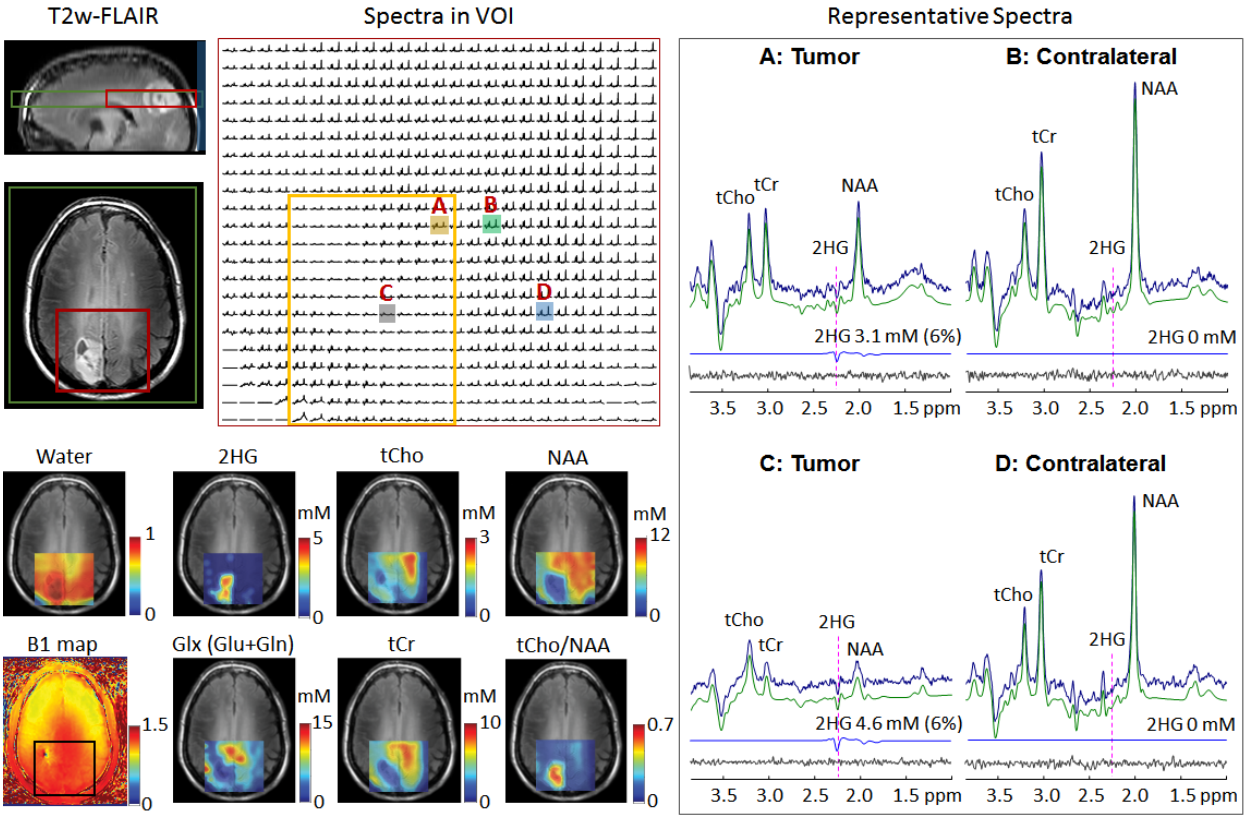

Figure 4.7 In vivo 2D DRAG-EPSI data from a patient with IDH1-mutated grade-II oligodendroglioma at 7T

When EPSI data are recorded only during the plateau period of readout gradients, SNR penalty may occur relative to the usual continuous sampling and the SNR efficiency, E_{SNR}, can be calculated from

the gradient plateau and ramp periods, as described in a prior study (*158*). For the readout gradient strength and slew rate used in the present study and for in-plane resolution of 6×6 mm^2, E_{SNR} of DRAG-EPSI may be identical to that of conventional EPSI (81%) and is expected to be higher by ~33% compared to the dual-readout flyback EPSI, whose spectral width can be as high as 1865 Hz with a very large peak flyback gradient strength (−20 mT/m). E_{SNR} can be increased using a high slew rate. When the slew rate is increased to 150 mT/m/ms, which was used in the Cunningham et al. study (*158*), the E_{SNR} of DRAG-EPSI will be increased to 92% with readout gradient strength of 7.4 mT/m and spectral width of 1638 Hz. This spectral width may be easily achievable by dual-readout flyback EPSI using readout gradient strength of 4.6 mT/m and peak flyback gradient strength of −25 mT/m, and E_{SNR} will be 83%, lower compared to DRAG-EPSI. For conventional EPSI, the maximum-achievable spectral width will be 1110 Hz using readout gradient strength of 16 mT/m, and E_{SNR} will be 73%. Taken together, DRAG-EPSI has advantages over conventional EPSI and dual-readout flyback EPSI in terms of E_{SNR} and gradient stress.

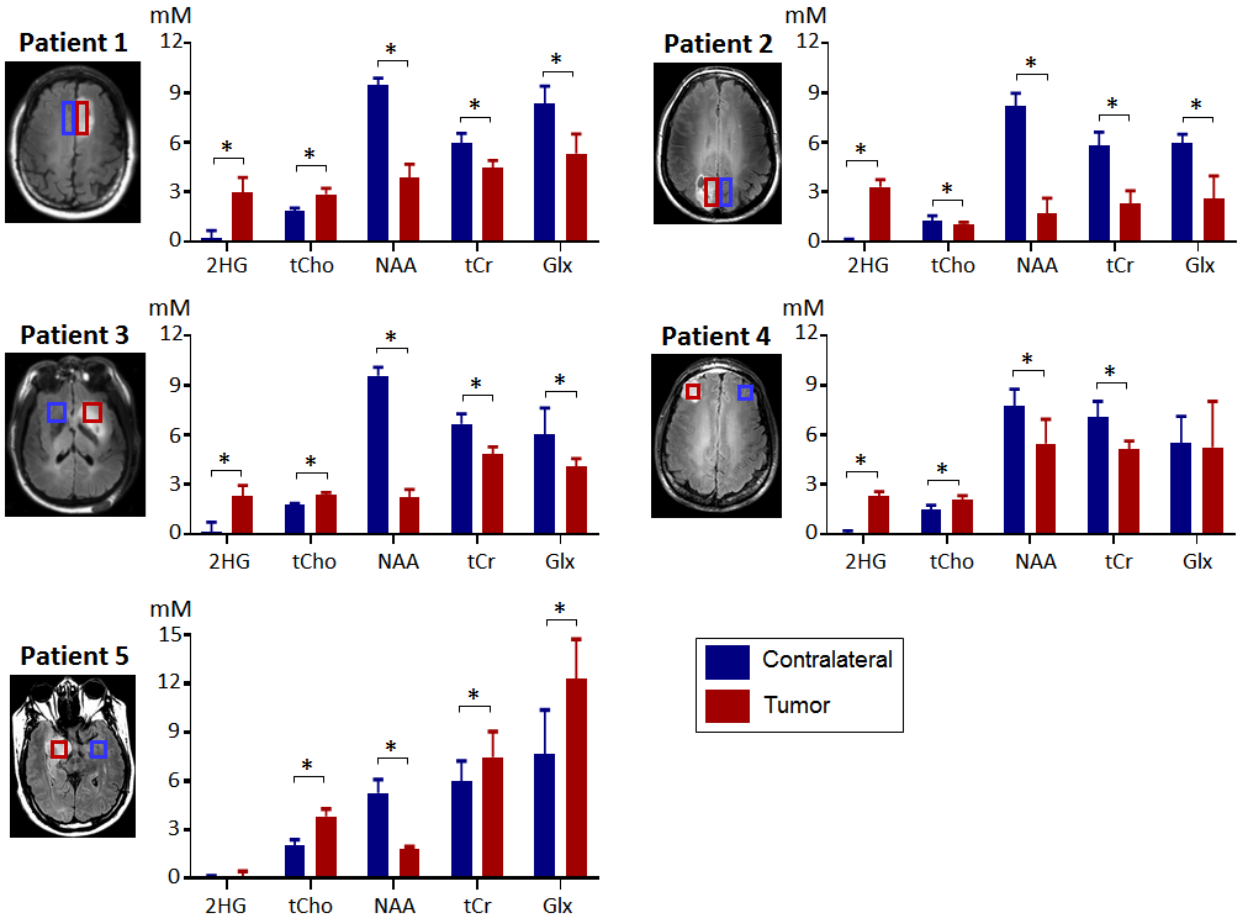

Figure 4.8 Comparison of the estimated concentrations of 2HG and 4 other metabolites in tumor vs. normal-appearing contralateral brain in five glioma patients at 7T

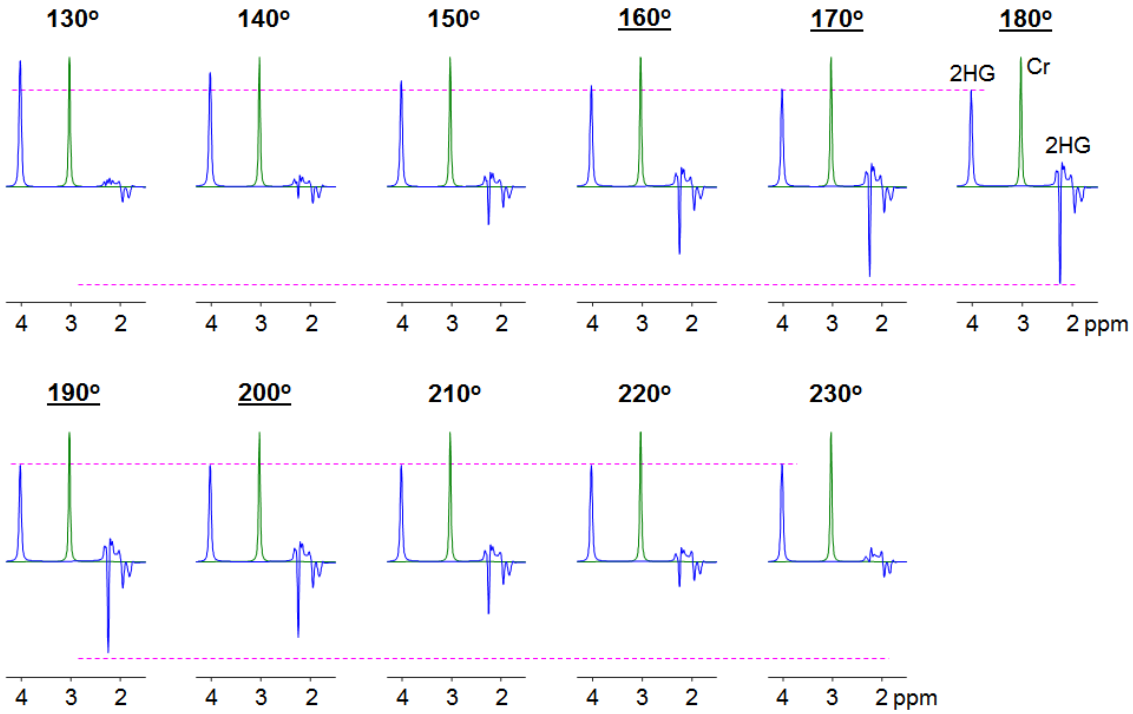

Figure 4.9 Numerically-calculated PRESS spectra of 2HG for various flip angles of the refocusing RF pulses at 7T

In the present study, field inhomogeneities were minimized by performing B_0 shimming and B_1 calibration on the VOI. For the 5 subjects, the B_0 variation within VOI was 3 - 16 Hz and the B_1 variations within VOI was 4 - 7% with respect to the mean B_1. The average coefficient of variation of B_1 over 5 patients was 5.8%. For PRESS, the spectral pattern and strength of J-coupled resonances are sensitive to the flip angle of the refocusing RF pulses, whilst the flip angle variation of the excitation RF pulse may have equal effects on the coupled and uncoupled spin signal strengths without altering the coupled-spin signal pattern. The effect of the refocusing pulse flip angle is more pronounced in strongly-coupled resonances than in weakly-coupled resonances. A refocusing pulse flip angle range of 160° - 200° may correspond to 95% confidence interval of the B_1 variation in this study (*i.e.*, 1.96×5.8% = 11.4%). A simulation indicated that, when normalized to a singlet, the 2HG C2-proton signal at 4.02 ppm remains about the same for the flip angle range, but the 2HG C4-proton signal is reduced as the flip angle deviates from 180° (see Figure 4.9). The 2HG 2.25 ppm signal to singlet ratios at flip angles of 160° and 200° were respectively 70% and 78% with respect to that at the 180° flip angle. The average singlet linewidth over five subjects was 9 Hz. With 3 Hz apodization, the SNR was improved and the resulting linewidth was 12 Hz. Our prior study using the 2HG-optimized PRESS (*21*) showed that the 2HG 2.25-ppm signal can be

reliably separated from adjacent signals up to singlet linewidth of 12 Hz. Achievement of high B_1 homogeneity is challenging at 7T. Uniform RF excitation may be achievable with adiabatic RF pulses for VOI prescription, similarly as in a prior single-voxel 2HG MRS study at 7T (*35*), in which 5-6 s TR was used. Use of long TR, which is needed to meet the specific absorption rate (SAR) requirement, hampers fast imaging of 2HG, whose signal is relatively small. In our study, without use of adiabatic RF pulse, the B_1 issue was alleviated with VOI-specific B_1 optimization.

The benefit of EPSI may be fully realized when metabolites are imaged with a much shorter scan time for a much higher matrix size imaging compared to conventional phase-encoded MRSI. In our study, the data matrix size was 33×30 with a scan time of 16 min. We chose to use a 2 s TR for metabolite quantification with relatively small variations in T_1 saturation effects across the brain metabolites, since the metabolite T_1s are fairly long at 7T (~1.8 s) (*162*). For 33×30 matrix size and 2 s TR, elliptically phase-encoded MRSI with single average may require ~26 min scan time (= $\pi/4\times33$ min), 1.6 fold longer than our DRAG-EPSI scan time. Scan time reduction benefit of DRAG-EPSI with respect to conventional phase-encoded MRSI can be further realized in higher matrix imaging of 2HG (*e.g.*, 3D imaging).

Since DRAG-EPSI requires dual readouts, the method has a loss in acceleration by a factor of 2 in such cases that conventional EPSI with single signal averaging per k-space point is sufficient. However, when multiple signal averaging is required for increasing SNR (as in the present study for measuring 2HG whose signals are relatively small), the data acquisitions may be split into two readouts without losing the acceleration factor compared to conventional EPSI.

Given the high clinical significance of 2HG, establishing a 2HG detection threshold may be clinically useful. It may require a rigorous analysis of many patient data from IDH mutant or wildtype tumors. With the limited number of patient data in the present study, we did not attempt to define the lower limit of 2HG detection, focusing on demonstration of new EPSI readout. Since detection of a metabolite depends on several factors, which include SNR, linewidth, interfering signals, overall spectral baseline, *etc*., a 2HG concentration threshold may not be easily definable. A most reliable threshold may be whether a 2HG signal is visually discernible in the spectrum or not. In this regard, the opposite signal polarity of 2HG with respect to the neighboring resonances of GABA and Glu, accomplished using the TE 78 ms PRESS at 7T, may help improve 2HG detection compared to short-TE MRS at 7T, as shown in our prior study (*21*). In this prior study, 2HG at 1 mM or higher was detectable with CRLBs smaller than 7%. In the present study, we discarded metabolite estimates with CRLB > 20%, which usually corresponded to 2HG estimates < 0.5 mM.

Lastly, the 2HG concentration was similar in Patients 1 and 2 (*i.e.*, 3.0 and 3.3 mM), but tCho, which is considered to be a marker of membrane turnover (*113*), was ~3 fold higher in Patient 1 than in

Patient 2 (2.9 *vs*. 1.0 mM). A prior 2HG MRS study showed correlation of 2HG level with tumor cellularity in gliomas (*34*). Lack of correlation between 2HG and tCho was reported in a prior 2HG study of 14 patients with IDH mutant gliomas (*154*). These lines of observation suggest that 2HG production may be related to tumor cellularity but may also be attributed to the differential competency of IDH mutant gliomas to produce 2HG.

4.6 CONCLUSION

In vivo high-resolution imaging of 2HG in glioma patients was achieved using a new ^{1}H EPSI approach at 7T. DRAG-EPSI, with dual bipolar readout alternated gradients and simple data processing, offered increased spectral window and SNR compared to published EPSI methods. As a well-established biomarker for IDH mutant gliomas, high-resolution imaging of the oncometabolite 2HG has high diagnostic and prognostic value. The proposed 2HG imaging technique has potential application to monitor the 2HG levels in therapeutic drug trials targeting IDH inhibition in gliomas (*153, 163, 164*).

CHAPTER FIVE

IN VIVO 3D 2HG IMAGING IN GLIOMA PATIENTS USING ECHO-PLANAR SPECTROSCOPIC IMAGING WITH DUAL-READOUT ALTERNATED GRADIENTS (DRAG-EPSI) AT 3T

5.1 INTRODUCTION

The identification of 2-hydroxyglutarate (2HG) by ^{1}H MRS in patients with isocitrate dehydrogenase (IDH) mutant gliomas is a major breakthrough in neuro-oncology imaging. 2HG is the first imaging biomarker that is specific to a genetic mutation in gliomas (*107*), making the diagnosis of IDH mutant gliomas possible without surgery. 2HG also has a significant predictive value with respect to the stage and survival in gliomas because IDH mutation carries a favorable prognosis (*3, 4*). Gliomas are highly heterogeneous and infiltrative in malignant transformation and recur beyond the borders of the initial tumor mass. The need of a surveillance technique for use in extended areas of the tumor is a high priority. The tumor cellularity and the 2HG level may be non-uniform within a tumor mass, and their spatial distributions may vary. A high-resolution 3D imaging platform to measure 2HG rapidly is an outstanding strength for monitoring IDH-mutant tumors. With the ability to detect 2HG by high-resolution 3D MRS imaging, this metabolite could be used to follow patients with much greater accuracy.

While several single-voxel MRS methods were proposed for in-vivo detection of 2HG in patients at 3T (*9, 88, 154*) and the methods are translated into many hospitals and used for patient care, multi-voxel MRS imaging of 2HG, in particular 3D high-resolution imaging, remains as a challenge. In 2012, Choi et al. presented 2HG mapping in a glioma patient using phase-encoded chemical shift imaging (CSI) (*9*). Although this prior study showed that 2HG can be imaged at clinically acceptable resolution

(voxel size 10×10×15 mm^3) with similar detectability as in single-voxel MRS, the application was limited to 2D imaging since 3D imaging by CSI modality is not practically feasible due to its long scan time. Recently Andronesi et al. reported 3D imaging of 2HG using a spiral spectroscopic imaging technique combined with J-difference editing (*91, 165*). The resolution was relatively low (voxel size 20×20×20 mm^3). The image data processing could be complicated with need of much efforts for off-resonance correction for spiral reconstruction (*14*) and additionally estimation of the 2HG target resonance (4.0 ppm), which is close to the water resonance, may be very susceptible to subtraction errors.

Recently, we reported a new MRS imaging scheme, dubbed DRAG-EPSI (echo-planar spectroscopic imaging with dual-readout alternated gradients) (*93*). In this prior study, the method was used for 2D imaging of 2HG at 7T, with in-plane resolution of 6×6 mm^2. In DRAG-EPSI, the time-domain MRS signals are constructed with combined analysis of data obtained with two sets of bipolar echo-planar readout gradients. Compared to conventional EPSI, the dwell time of DRAG-EPSI is smaller by 50% and consequently the spectral width is twofold larger for identical readout-gradient strengths between the methods, as shown in the 7T study. The increase in spectral width may be highly beneficial for imaging at 7T, reducing signal aliasing substantially. As an alternative, when the spectral width of conventional EPSI is large enough for covering the spectral region of interest (e.g., MRS imaging at 3T), DRAG-EPSI can be utilized for similar-quality imaging using reduced readout-gradient strengths, which may alleviate frequency drifts and acoustic noise and possibly improving the data quality and subject compliance. When compared to CSI, the benefit of EPSI may be fully realized when metabolites are imaged for large data matrix size (e.g., 3D imaging). In the present study, we demonstrate the fidelity of DRAG-EPSI for 3D high-resolution imaging of 2HG and other brain metabolites using subject-friendly readout-gradient strengths. Following in-vitro validation of the method, preliminary data from a healthy subject and four brain tumor patients with IDH-mutant gliomas are presented.

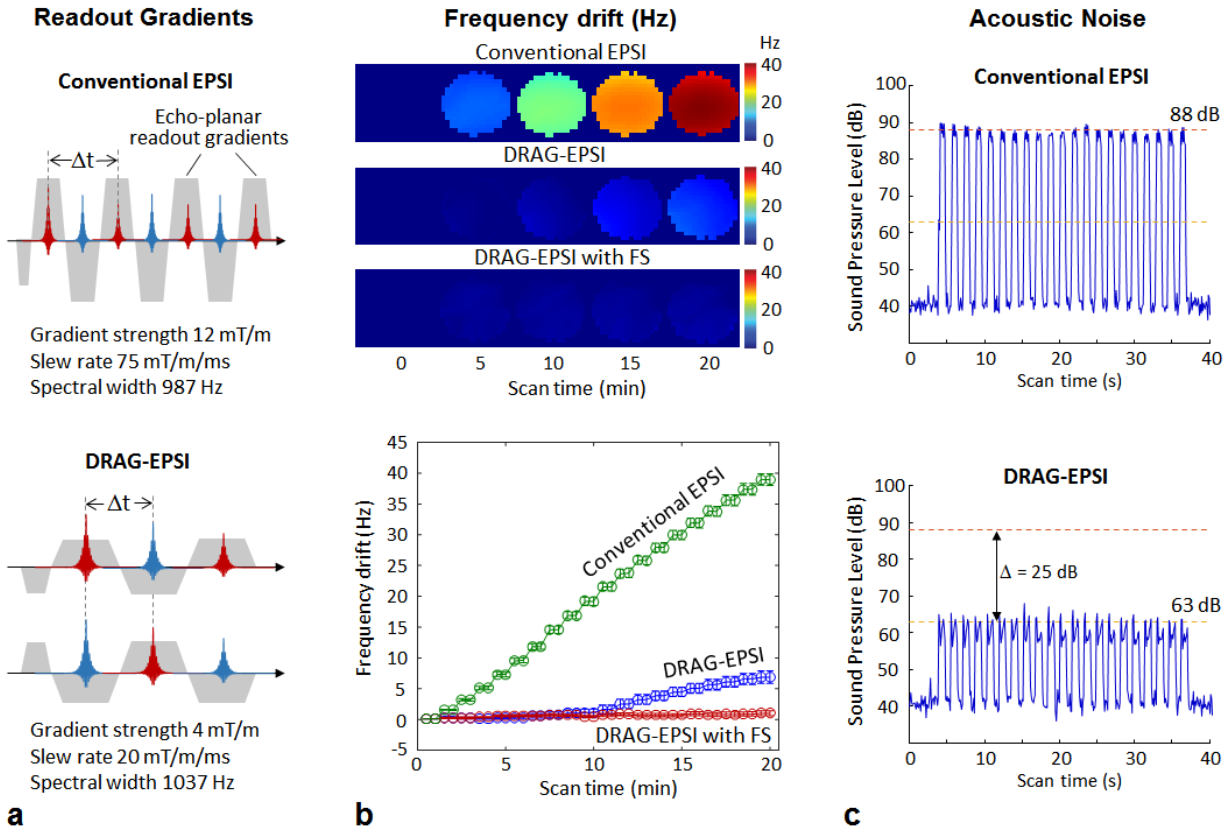

Figure 5.1 Comparison of frequency drifts and sound pressure level induced by conventional EPSI, DRAG-EPSI, and DRAG-EPSI with Frequency Stabilization

5.2 METHOD

MR experiments were carried out in a human whole-body 3T MR scanner (Philips Medical Systems, Best, The Netherlands) using a whole-body quadrature transmit coil and a 32-channel receive head coil (Nova Medical, Wilmington, MA). The gradient system offered maximum amplitude of 40 mT/m, with maximum slew rate of 200 mT/m/ms. In-vitro EPSI experiments were performed in a 17-cm diameter GE Braino phantom and a 10-cm diameter spherical phantom with 2HG (4 mM), choline (2mM), glutamate (Glu) (4 mM), lactate (Lac) (2 mM), N-acetylaspartate (NAA) (4 mM), creatine (Cr) (4 mM), and myo-inositol (mI) (4 mM).

One healthy subject (27-year old female) and four glioma patients were enrolled, who included an IDH1-mutated grade-II mixed glioma (26-year old female), an IDH1-mutated grade-II

oligodendroglioma (43-year old male), an IDH1-mutated grade-III astrocytoma (38-year old male), and an IDH2-mutated grade-IV glioblastoma (31-year-old male). The protocol was approved by the Institutional Review Board of the University of Texas Southwestern Medical Center. Written informed consent was obtained from subjects prior to MR scans.

3D DRAG-EPSI was preceded by prescription of a volume of interest (VOI) using a previously-reported 3T 2HG-optimized TE 97ms PRESS sequence (*9*). The PRESS sequence included a 5.8 ms 73° excitation RF pulse (bandwidth 2.5 kHz) and two 13.2 ms 180° RF pulses (bandwidth 1.3 kHz) at RF field intensity (B_1) of 13.5 μT. The echo-planar readout gradient consisted of 1024 alternating trapezoidal gradients with amplitude of 4 mT/m and slope of 20 mT/m/ms (slope length of 200 μs and plateau length of 563 μs). Two sets of data were acquired with opposed-polarity readouts in an interleaved fashion (see **Fig. 5.1b** for gradient strength and slew rate). The spectral width of the DRAG-EPSI was 1037 Hz (8.1 ppm at 3T). Water suppression was obtained with a vendor-supplied four various-flip angle pulse scheme (MOIST). Up to second order B_0 shimming was carried out on the VOI using a vendor-supplied tool. Water-suppressed DRAG-EPSI was acquired with the following parameters: PRESS TE = 97 ms (TE_1 = 32 ms and TE_2 = 65 ms), TR = 1.6 s, field of view (FOV) = 240×180×80 mm^2, spatial resolution = 1 mL (10×10×10 mm^3), data matrix size = 24×18×8×1024, number of signal averages = 4, and slice-selective RF pulse carrier = 2.7 ppm. The scan time was 19.2 min. Unsuppressed-water imaging data were acquired with VOI prescription by TE 97 ms PRESS using DRAG-EPSI and by TE 14 ms STEAM using conventional EPSI (scan times of 2.4 and 1.2 min respectively, and slice-selective RF pulse carrier at 4.68 ppm for both). T_2w-FLAIR (T_2-weighted fluid attenuated inversion recovery imaging) was acquired for tumor identification (TR/TE/TI = 9000/125/2600ms; FOV = 230×200 mm^2; slice thickness = 4 mm; 45 transverse slices).

The 3D k-space data were zero filled to 48×36 matrix and subsequently apodized with a 3D Hamming function. The time domain data were zero filled to 2048 points and apodized with a 2 Hz exponential function. Eddy-current compensation and multi-channel combination were conducted using

the unsuppressed PRESS DRAG-EPSI water as reference, after which the two sets of interleaved data were combined without additional phase correction, similarly as in our prior study (*93*). Spectral fitting was performed between 1.1 and 3.7 ppm, with LCModel software, using in-house calculated basis spectra of 14 metabolites, which included 2HG, Glu, NAA, mI, Lac, Gln (glutamine), tCr (Cr + phosphocreatine), Gly (glycine), GSH (glutathione), Ace (acetate), Asp (aspartate), sI (scyllo-inositol), NAAG (N-acetylaspartylglutamate), tCho (glycerophosphorylcholine + phosphorylcholine). The metabolite signal estimates from LCModel were normalized to the unsuppressed TE 14 ms STEAM water for individual voxels, which was to correct for potential B_1 variations, and subsequently the metabolite concentrations were calculated by scaling the normalized metabolite signal estimates with reference to tCr in normal-appearing gray-matter region at 8 mM (*166, 167*). Metabolite estimates with CRLB > 20% were discarded, similarly as in prior EPSI studies (*11, 18, 91*). All data are presented as mean ± standard deviation (SD).

5.3 RESULTS

We compared the frequency drifts induced by DRAG-EPSI with those of conventional EPSI in a phantom solution. The spectral width was set to be similar between conventional EPSI and DRAG-EPSI (987 Hz vs. 1037 Hz). Since the spectral width in DRAG-EPSI is determined by the time interval between the adjacent odd and even number echoes, the readout gradient strength and slew rate of DRAG-EPSI were much lower than those of conventional EPSI, as shown in **Figure 5.1a**. For each of the EPSIs, 40 images were acquired for 20 min and subsequently the drifts of water resonance frequency were calculated with reference to the first imaging scan. The frequency drift averaged over the voxels within the phantom was much smaller (5.5 fold) in DRAG-EPSI than in conventional EPSI (7.0±1.0 vs. 38.8±1.0 Hz) (**Fig. 5.1b**), which was most likely due to the differences in readout gradient strength and slew rate. With a real-time frequency-drift correction tool (Frequency Stabilization (FS); supplied by the vendor), the frequency drift in DRAG-EPSI was further reduced to 1.1±0.4 Hz (indicated by DRAG-EPSI with FS). Due to the difference in the readout gradients, the DRAG-EPSI scan was much more quite than

conventional EPSI. When measured by a microphone placed within the head coil, the sound pressure level was 63 dB in DRAG-EPSI, 25 dB smaller compared to conventional EPSI (88 dB) (**Fig. 5.1c**).

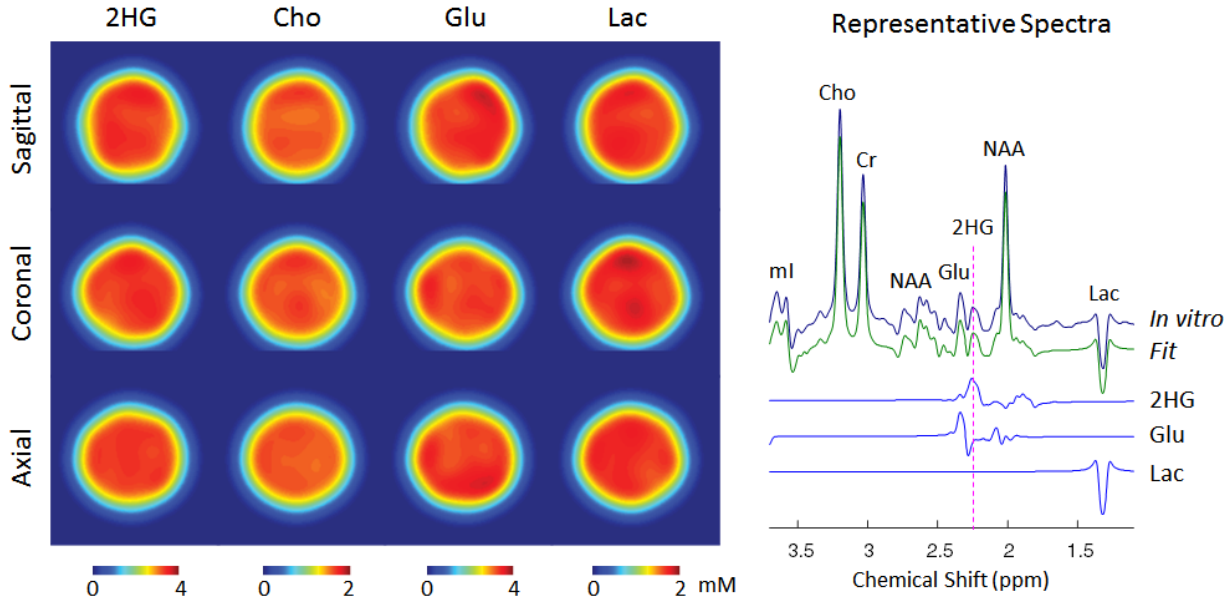

Figure 5.2 In-vitro validation of 3D DRAG-EPSI in a 10-cm diameter spherical phantom

The performance of DRAG-EPSI for 2HG detection was tested in a 10-cm diameter spherical phantom with 2HG, Glu, and five additional compounds that may be well detectable in brain tumors. Using TE 97 ms PRESS (TE_1 = 32 ms and TE_2 = 65 ms), the J-coupled C4-proton resonances of 2HG exhibited a positive-polarity signal at 2.25 ppm, well separated from the Glu 2.35 ppm resonance (singlet FWHM 5 Hz) (**Fig. 5.2**). Spectral fitting by LCModel reproduced all spectra well. The 2HG-to-Cho ratio was estimated to be 2.04±0.08, in good agreement with the prepared concentration ratio of 2:1. The maps of 2HG, Cho, Glu, and Lac estimates showed fairly uniform estimates in the sagittal, coronal, and axial directions within the phantom. The coefficient of variation of concentration estimates was 2 - 3% for the six compounds in the phantom.

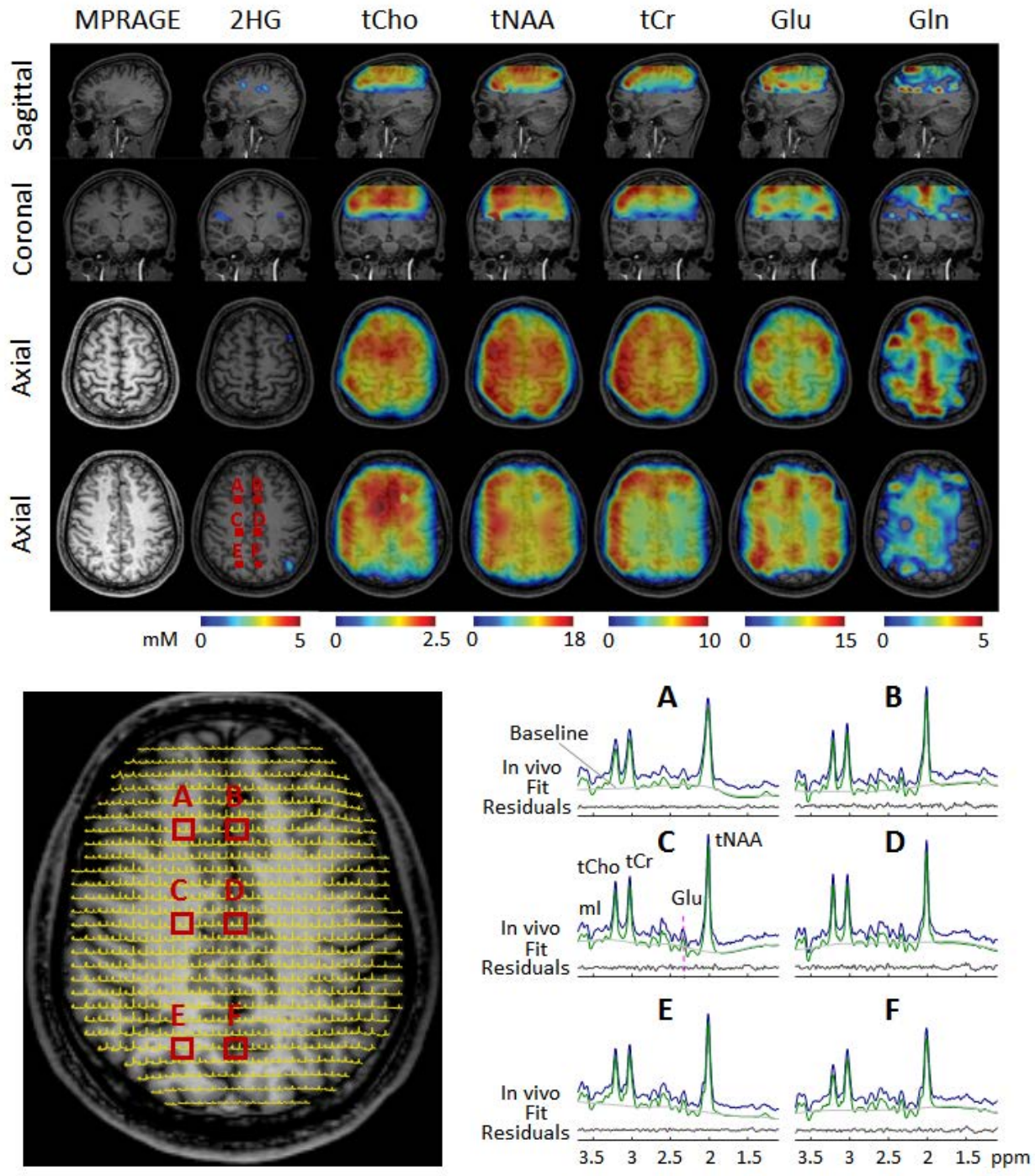

Figure 5.3 3D DRAG-EPSI in a healthy subject in vivo.

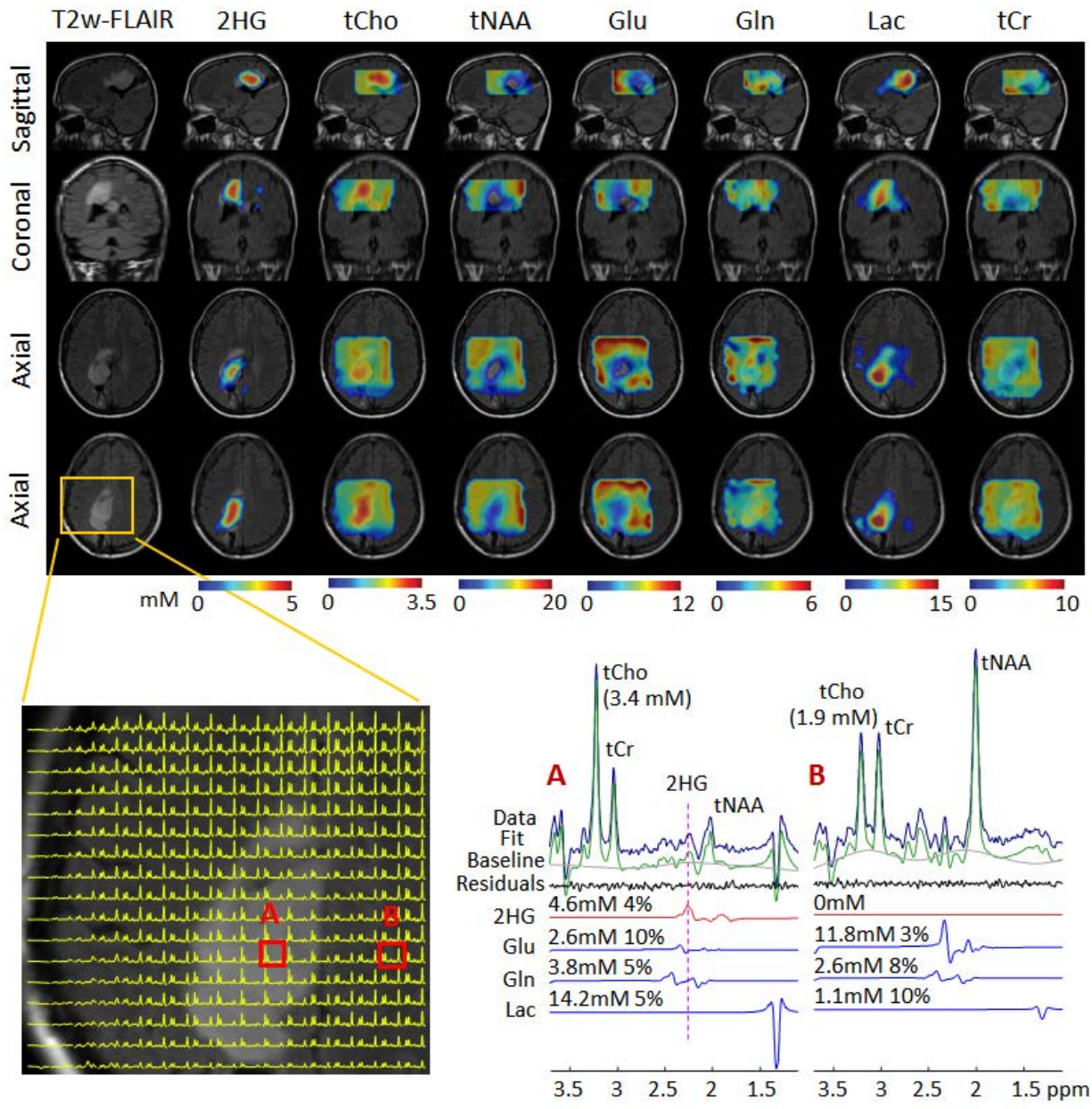

Figure 5.4 In-vivo 3D DRAG-EPSI in a pre-surgery patient with IDH1-mutant glioma (Grade II oligoastrocytoma)

The DRAG-EPSI, combined with TE 97 ms PRESS, was tested in a healthy subject (27-year old). A VOI of 140×120×65 mm^3 was set to cover the whole brain. 2HG was unmeasurable across the brain (< 0.5 mM with CRLB > 100%) (**Fig. 5.3**). The map of tCho showed that the concentration was significantly higher in the anterior brain than in the posterior brain (1.8 vs. 1.3 mM; $p < 0.001$). tNAA was fairly uniform

within the brain whilst tCr, Glu, and Gln were clearly higher in gray-matter dominant regions than white-matter dominant regions, in agreement with prior studies (*96, 151*).

The DRAG-EPSI with 2HG-tailored PRESS prescription was used for imaging of 2HG and other metabolites in 4 patients with IDH-mutant gliomas. For a patient with IDH1-mutant grade-II oligoastrocytoma (26-year old; female), T_2w-FLAIR identified a solid tumor mass in the left medial-occipital region (**Fig. 5.4**). For a VOI of 100×100×65 mm^3, which included the tumor and contralateral normal-appearing brain, the maps of 2HG showed that the volume with elevated 2HG agreed well with that of T_2w-FLAIR hyperintensity. The 2HG estimate was as high as 5 mM in the center of the tumor while normal-appearing brain showed essentially null 2HG (< 0.5 mM). tCho was substantially high in the tumor compared to normal-appearing brain regions (1.9 vs. 1.5 Mm; $p < 0.001$). Lac was highly elevated (> 10 fold) in the tumor, indicating markedly increased glycolysis in the tumor.

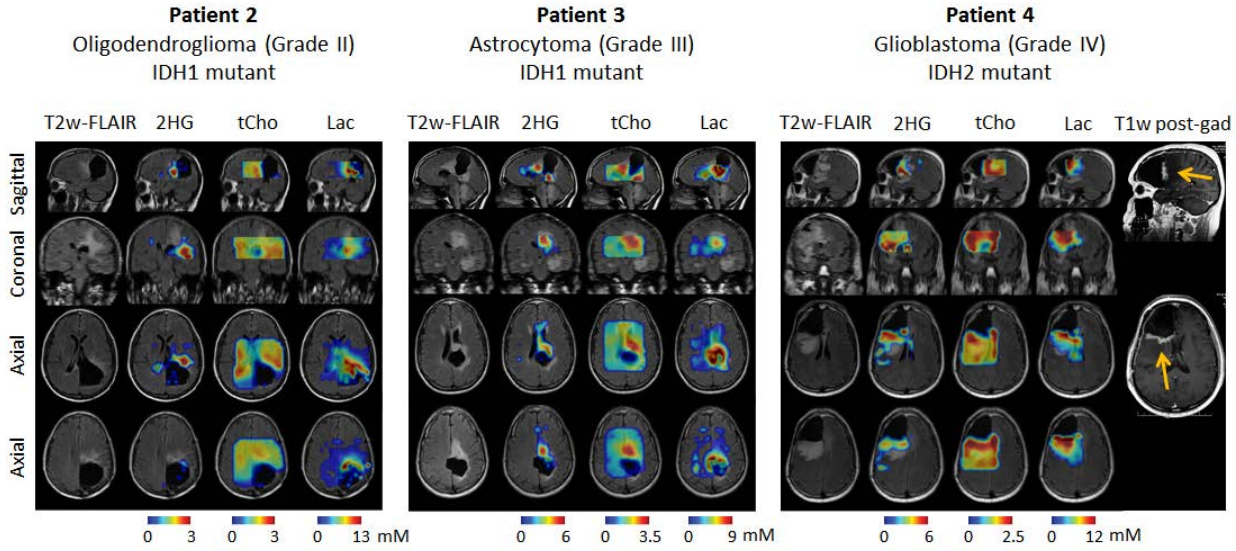

Figure 5.5 In-vivo 3D DRAG-EPSI data from three post-surgery patients with IDH-mutant gliomas

Figure 5.5 presents DRAG-EPSI data from three post-surgery patients with IDH mutant gliomas. T_2w-FLAIR imaging showed lesions outside the resection cavities in all three cases. 2HG was measured to be up to 3, 6, and 6 mM in the lesions of the three patients (CRLB of 6%, 5% and 6%,

respectively), indicating the lesions were all recurrent tumors. In all three cases, the tumors also showed increased tCho and Lac (as shown in the 3D maps). For patient 2, the coronal T_2w-FLAIR images showed two distinct tumor masses, among which 2HG was clearly detectable only in the lower part. In contrast, for patient 3 who also had two distinct tumor masses, 2HG was measurable in both anterior and posterior regions of the tumor mass, as seen in the sagittal image. In patient 4, the 2HG level was higher in the anterior part of the tumor mass compared to other regions within the tumor, and the high-2HG regions were consistent with enhancement in T_1w post-gadolinium imaging. In all three post-surgery cases, the regions with null metabolite signals showed excellent agreement with the resection cavities indicated in T_2w-FLAIR images.

5.4 DISCUSSION

We demonstrate 3D high-resolution imaging of 2HG and other metabolites in brain tumor subjects at 3T, which was achieved using a newly-developed 3D DRAG-EPSI scheme together with a previously-reported 2HG-tailored TE 97 ms PRESS sequence. To our best knowledge, this is the first report of 3D imaging of 2HG with resolution of $10\times10\times10$ mm^3, which is the same resolution as in prior EPSI studies of relatively large metabolite signals (e.g., NAA, tCr and tCho). As shown in our phantom study, the frequency drift induced by DRAG-EPSI was much smaller compared to conventional EPSI (7 vs. 39 Hz during a 20-min scan). This was most likely due to the use of relatively low gradient strengths in DRAG-EPSI given that gradient pulses cause heating in the shimming coil and consequently changes in the B_0 fields (*161*). It is noteworthy that in our case, the frequency drift was further reduced and essentially negligible ($\leq$ 1 Hz) with the use of a vendor-supplied real-time frequency-drift correction tool (Frequency Stabilization), and thus our 3D imaging data may not have considerable artifacts associated with frequency drifts. Also, the reduction in acoustic noise in DRAG-EPSI is highly beneficial for patient scans. Brain tumor patients often show seizure activities. The seizure incidence can be increased by extensive noise during an imaging scan. In practice, at the beginning of our development of high-resolution 2HG imaging,

when we were using a conventional EPSI scheme shown in **Fig. 5.1a**, a tumor patient who was sensitive to acoustic noise showed a seizure immediately after the scan. This incidence suggested conventional EPSI was not ideally applicable in tumor patients and we were urged to develop a new imaging tool that has much lower acoustic noise level. We believe improvement in patient comfort by reduced acoustic noise may also be helpful for minimizing potential subject motions and eventually improving the imaging data quality. In reality, the reduction of acoustic noise by 25 dB using DRAG-EPSI (**Fig. 5.1c**) was greatly beneficial for 2HG imaging, without an adverse event during the study and without any concerning remarks on acoustic noise from patient volunteers.

Several researchers reported imaging of 2HG in patients with IDH-mutant gliomas at 3T. In two of Choi et al. studies which used 2D phase-encoded chemical shift imaging with $10\times10\times15$ mm^3 (1.5 mL) voxel size (*9, 168*), the volumes with elevated 2HG were similar to or somewhat smaller than the volumes with T_2w-FLAIR hyperintensity. Using a 3D spiral spectroscopic imaging method with $20\times20\times20$ mm^3 voxel size (8 mL), Jafari-Khouzani et al. reported larger volumes with elevated 2HG than T_2w-FLAIR volumes and partial agreement on the locations of the two volumes in more than half of the patients (*165*). The discrepancy in tumor volumes and locations between 2HG imaging and T_2w-FLAIR could be due to the large difference in spatial resolution of images (8 mL vs. 0.001 mL). Andronesi et al., from the same group, used the same method for assessing treatment response in IDH mutant glioma patients (*91*). It is likely that 2HG is closely related to the clinical behavior of ID-mutant tumors. Published data suggest great potential of 2HG mapping for monitoring disease progression (*168*) and treatment effects (*91, 168*) in IDH-mutant gliomas. Gliomas are very diffusive. Following an open-resection surgery, tumors can recur in small volumes in the periphery of the resection cavity. The capability to image 2HG at high resolution in three-dimensional space can provide a tool for following IDH-mutant glioma patients with much greater accuracy, which was the primary goal of the present study.

EPSI has been successfully implemented and studied across three major vendors (Philips, Siemens and GE) for time-efficient imaging of metabolites in human brain (*12*). The imaging performance

was reportedly similar between the vendors. The PRESS scheme, which was used for 2HG signal manipulation in this study, is available in most of clinical scanners. Although the vendor-supplied RF pulses and subecho times of PRESS are somewhat different and consequently the signal intensities and patterns of 2HG, Glu and Gln differ slightly between the vendors, the 2HG detectability appears to be optimal at TE 90 - 100 ms across the major vendors (*169*). Therefore, 3D DRAG-EPSI can be easily implemented together with 2HG-optimized PRESS in clinical scanners and used for high-resolution imaging of 2HG.

A major drawback of DRAG-EPSI is requirement of two excitations per k-space point at minimum. This may be acceptable for imaging of 2HG whose signal is relatively small and may require some averaging for achieving acceptable SNR in many cases. Imaging of unsuppressed water, which is often used for eddy-current compensation, may be prolonged because of the two-excitation requirement. In the present study, the voxel size of unsuppressed-water DRAG-EPSI imaging was set to $20\times20\times10$ mm^3 (scan time 2.4 min) and the water signal of each voxel was used for correcting the eddy-current effects in 4 voxels of 2HG imaging data, similarly as in prior studies (*64*). We believe that the eddy-current effects were properly corrected as the effects in the four neighboring voxels were very similar. For whole-brain imaging, FOV may be set to be larger than that of the present study ($240\times180\times160$ mm^3 vs. $240\times180\times80$ mm^3). The increased FOV requires twofold larger number of phase-encoding gradients. One may consider changing the number of signal averages per k-space point from 4 to 2, which may maintain both the 2HG imaging scan length and the SNR. The water imaging scan time may be kept acceptable by reducing the TR and/or the spatial resolution. Another limitation in this imaging study was that the VOIs in patient scans were $120\times120\times65$ mm^3 or smaller and thus, the VOI may not be ideally applicable for large tumor masses. Although whole-brain imaging is in general preferable, imaging on relatively small volumes may be practically beneficial for improving the spectral quality, which may include proper B_1 calibration and B_0 shimming, acceptable water suppression, and minimal lipid contamination across the voxels within the VOI.

For these reasons, we chose to use relatively small, clinically acceptable VOI in patient scans, similarly as in several prior studies (*91, 170, 171*).

5.5 CONCLUSION

In conclusion, we demonstrated in-vivo imaging of 2HG in glioma patients using EPSI with dual bipolar readout alternated gradients. 3D imaging of 2HG with acquisition resolution of 10×10×10 mm^3 was a major accomplishment relative to prior 2HG imaging studies. Compared to conventional EPSI, the method needed much smaller readout gradient strengths and showed much less frequency drifts and lower acoustic noise, which may be preferable for quality imaging in patient populations. 2HG is an unprecedented diagnostic and prognostic biomarker in brain tumors. 3D high-resolution imaging of 2HG using DRAG-EPSI may confer an integrated view across the tumor and surrounding normal brain and may provide novel biological insights that could drive therapeutic development for IDH-mutant brain cancers.

BIBLIOGRAPHY

1. D. Hanahan, R. A. Weinberg, Hallmarks of cancer: the next generation. *Cell* **144**, 646-674 (2011).
2. R. J. DeBerardinis, C. B. Thompson, Cellular metabolism and disease: what do metabolic outliers teach us? *Cell* **148**, 1132-1144 (2012).
3. D. W. Parsons, S. Jones, X. Zhang, J. C. Lin, R. J. Leary, P. Angenendt, P. Mankoo, H. Carter, I. M. Siu, G. L. Gallia, A. Olivi, R. McLendon, B. A. Rasheed, S. Keir, T. Nikolskaya, Y. Nikolsky, D. A. Busam, H. Tekleab, L. A. Diaz, Jr., J. Hartigan, D. R. Smith, R. L. Strausberg, S. K. Marie, S. M. Shinjo, H. Yan, G. J. Riggins, D. D. Bigner, R. Karchin, N. Papadopoulos, G. Parmigiani, B. Vogelstein, V. E. Velculescu, K. W. Kinzler, An integrated genomic analysis of human glioblastoma multiforme. *Science* **321**, 1807-1812 (2008).
4. H. Yan, D. W. Parsons, G. Jin, R. McLendon, B. A. Rasheed, W. Yuan, I. Kos, I. Batinic-Haberle, S. Jones, G. J. Riggins, H. Friedman, A. Friedman, D. Reardon, J. Herndon, K. W. Kinzler, V. E. Velculescu, B. Vogelstein, D. D. Bigner, IDH1 and IDH2 mutations in gliomas. *The New England journal of medicine* **360**, 765-773 (2009).
5. J. Balss, J. Meyer, W. Mueller, A. Korshunov, C. Hartmann, A. Deimling, Analysis of the IDH1 codon 132 mutation in brain tumors. *Acta Neuropathol* **116**, 597-602 (2008).
6. L. Dang, D. W. White, S. Gross, B. D. Bennett, M. A. Bittinger, E. M. Driggers, V. R. Fantin, H. G. Jang, S. Jin, M. C. Keenan, K. M. Marks, R. M. Prins, P. S. Ward, K. E. Yen, L. M. Liau, J. D. Rabinowitz, L. C. Cantley, C. B. Thompson, M. G. Vander Heiden, S. M. Su, Cancer-associated IDH1 mutations produce 2-hydroxyglutarate. *Nature* **462**, 739-744 (2009).
7. M. E. Figueroa, O. Abdel-Wahab, C. Lu, P. S. Ward, J. Patel, A. Shih, Y. Li, N. Bhagwat, A. Vasanthakumar, H. F. Fernandez, M. S. Tallman, Z. Sun, K. Wolniak, J. K. Peeters, W. Liu, S. E. Choe, V. R. Fantin, E. Paietta, B. Lowenberg, J. D. Licht, L. A. Godley, R. Delwel, P. J. Valk, C. B. Thompson, R. L. Levine, A. Melnick, Leukemic IDH1 and IDH2 mutations result in a hypermethylation phenotype, disrupt TET2 function, and impair hematopoietic differentiation. *Cancer Cell* **18**, 553-567 (2010).
8. P. S. Ward, J. Patel, D. R. Wise, O. Abdel-Wahab, B. D. Bennett, H. A. Coller, J. R. Cross, V. R. Fantin, C. V. Hedvat, A. E. Perl, J. D. Rabinowitz, M. Carroll, S. M. Su, K. A. Sharp, R. L. Levine, C. B. Thompson, The common feature of leukemia-associated IDH1 and IDH2 mutations is a neomorphic enzyme activity converting alpha-ketoglutarate to 2-hydroxyglutarate. *Cancer Cell* **17**, 225-234 (2010).
9. C. Choi, S. K. Ganji, R. J. DeBerardinis, K. J. Hatanpaa, D. Rakheja, Z. Kovacs, X. L. Yang, T. Mashimo, J. M. Raisanen, I. Marin-Valencia, J. M. Pascual, C. J. Madden, B. E. Mickey, C. R. Malloy, R. M. Bachoo, E. A. Maher, 2-hydroxyglutarate detection by magnetic resonance spectroscopy in IDH-mutated patients with gliomas. *Nature medicine* **18**, 624-629 (2012).
10. P. Mansfield, Spatial-Mapping of the Chemical-Shift in Nmr. *J Phys D Appl Phys* **16**, L235-L238 (1983).
11. S. Posse, R. Otazo, A. Caprihan, J. Bustillo, H. Chen, P. G. Henry, M. Marjanska, C. Gasparovic, C. Zuo, V. Magnotta, B. Mueller, P. Mullins, P. Renshaw, K. Ugurbil, K. O. Lim, J. R. Alger, Proton echo-planar spectroscopic imaging of J-coupled resonances in human brain at 3 and 4 Tesla. *Magn Reson Med* **58**, 236-244 (2007).

12. M. Sabati, S. Sheriff, M. Gu, J. Wei, H. Zhu, P. B. Barker, D. M. Spielman, J. R. Alger, A. A. Maudsley, Multivendor implementation and comparison of volumetric whole-brain echo-planar MR spectroscopic imaging. *Magn Reson Med* **74**, 1209-1220 (2015).

13. A. A. Maudsley, R. K. Gupta, R. Stoyanova, N. A. Parra, B. Roy, S. Sheriff, N. Hussain, S. Behari, Mapping of glycine distributions in gliomas. *AJNR. American journal of neuroradiology* **35**, S31-36 (2014).

14. S. Posse, R. Otazo, S. R. Dager, J. Alger, MR spectroscopic imaging: principles and recent advances. *Journal of magnetic resonance imaging : JMRI* **37**, 1301-1325 (2013).

15. G. Metzger, X. Hu, Application of interlaced Fourier transform to echo-planar spectroscopic imaging. *J Magn Reson* **125**, 166-170 (1997).

16. A. Ebel, A. A. Maudsley, M. W. Weiner, N. Schuff, Achieving sufficient spectral bandwidth for volumetric ^{1}H echo-planar spectroscopic imaging at 4 Tesla. *Magnetic resonance in medicine : official journal of the Society of Magnetic Resonance in Medicine / Society of Magnetic Resonance in Medicine* **54**, 697-701 (2005).

17. C. H. Cunningham, J. M. Pauly, K. S. Nayak, Saturated double-angle method for rapid B1+ mapping. *Magn Reson Med* **55**, 1326-1333 (2006).

18. Y. Li, P. Larson, A. P. Chen, J. M. Lupo, E. Ozhinsky, D. Kelley, S. M. Chang, S. J. Nelson, Short-echo three-dimensional H-1 MR spectroscopic imaging of patients with glioma at 7 Tesla for characterization of differences in metabolite levels. *Journal of magnetic resonance imaging : JMRI* **41**, 1332-1341 (2015).

19. S. Matsui, K. Sekihara, H. Kohno, High-Speed Spatially Resolved Nmr-Spectroscopy Using Phase-Modulated Spin-Echo Trains - Expansion of the Spectral Bandwidth by Combined Use of Delayed Spin-Echo Trains. *J Magn Reson* **64**, 167-171 (1985).

20. K. Kuroda, R. V. Mulkern, K. Oshio, L. P. Panych, T. Nakai, T. Moriya, S. Okuda, K. Hynynen, F. A. Jolesz, Temperature mapping using the water proton chemical shift: self-referenced method with echo-planar spectroscopic imaging. *Magn Reson Med* **43**, 220-225 (2000).

21. S. K. Ganji, Z. An, V. Tiwari, S. McNeil, M. C. Pinho, E. Pan, B. E. Mickey, E. A. Maher, C. Choi, In vivo detection of 2-hydroxyglutarate in brain tumors by optimized point-resolved spectroscopy (PRESS) at 7T. *Magn Reson Med* **77**, 936-944 (2017).

22. S. Ramadan, A. Lin, P. Stanwell, Glutamate and Glutamine: A Review of In Vivo MRS in the Human Brain. *NMR Biomed* **26**, 10.1002/nbm.3045 (2013).

23. F. Yamasaki, T. Takayasu, R. Nosaka, V. J. Amatya, A. Doskaliyev, Y. Akiyama, A. Tominaga, Y. Takeshima, K. Sugiyama, K. Kurisu, Magnetic resonance spectroscopy detection of high lipid levels in intraaxial tumors without central necrosis: a characteristic of malignant lymphoma. *Journal of neurosurgery* **122**, 1370-1379 (2015).

24. D. E. Befroy, G. I. Shulman, Magnetic Resonance Spectroscopy Studies of Human Metabolism. *Diabetes* **60**, 1361-1369 (2011).

25. L. N. Manganas, X. Zhang, Y. Li, R. D. Hazel, S. D. Smith, M. E. Wagshul, F. Henn, H. Benveniste, P. M. Djurić, G. Enikolopov, M. Maletić-Savatić, Magnetic Resonance Spectroscopy Identifies Neural Progenitor Cells in the Live Human Brain. *Science (New York, N.Y.)* **318**, 980-985 (2007).

26. M.-C. Pardon, M. Yanez Lopez, D. Yuchun, M. Marjańska, M. Prior, C. Brignell, S. Parhizkar, A. Agostini, L. Bai, D. P. Auer, H. M. Faas, Magnetic Resonance Spectroscopy discriminates the response to microglial stimulation of wild type and Alzheimer's disease models. *Scientific Reports* **6**, 19880 (2016).

27. M. Marjanska, G. L. Curran, T. M. Wengenack, P.-G. Henry, R. L. Bliss, J. F. Poduslo, C. R. Jack, K. Uğurbil, M. Garwood, Monitoring disease progression in transgenic mouse models of Alzheimer's disease with proton magnetic resonance spectroscopy. *Proceedings of the National Academy of Sciences of the United States of America* **102**, 11906-11910 (2005).

28. D. P. Soares, M. Law, Magnetic resonance spectroscopy of the brain: review of metabolites and clinical applications. *Clinical Radiology* **64**, 12-21 (2009).

29. G. Öz, J. R. Alger, P. B. Barker, R. Bartha, A. Bizzi, C. Boesch, P. J. Bolan, K. M. Brindle, C. Cudalbu, A. Dinçer, U. Dydak, U. E. Emir, J. Frahm, R. G. González, S. Gruber, R. Gruetter, R. K. Gupta, A. Heerschap, A. Henning, H. P. Hetherington, F. A. Howe, P. S. Hüppi, R. E. Hurd, K. Kantarci, D. W. J. Klomp, R. Kreis, M. J. Kruiskamp, M. O. Leach, A. P. Lin, P. R. Luijten, M. Marjańska, A. A. Maudsley, D. J. Meyerhoff, C. E. Mountford, S. J. Nelson, M. N. Pamir, J. W. Pan, A. C. Peet, H. Poptani, S. Posse, P. J. W. Pouwels, E.-M. Ratai, B. D. Ross, T. W. J. Scheenen, C. Schuster, I. C. P. Smith, B. J. Soher, I. Tkáč, D. B. Vigneron, R. A. Kauppinen, M. R. S. C. G. For the, Clinical Proton MR Spectroscopy in Central Nervous System Disorders. *Radiology* **270**, 658-679 (2014).

30. P. B. Barker, A. Bizzi, N. De Stefano, D. D. Lin, *Clinical MR spectroscopy: techniques and applications*. (Cambridge University Press, 2010).

31. J. Kurhanewicz, R. Bok, S. J. Nelson, D. B. Vigneron, Current and Potential Applications of Clinical (13)C MR Spectroscopy. *Journal of nuclear medicine : official publication, Society of Nuclear Medicine* **49**, 341-344 (2008).

32. K. R. Thulborn, Quantitative sodium MR imaging: A review of its evolving role in medicine. *NeuroImag* **168**, 250-268 (2018).

33. E. A. Lopez-Beltran, M. J. Mate, S. Cerdan, Dynamics and environment of mitochondrial water as detected by ^{1}H NMR. *The Journal of biological chemistry* **271**, 10648-10653 (1996).

34. C. Choi, J. M. Raisanen, S. K. Ganji, S. Zhang, S. S. McNeil, Z. An, A. Madan, K. J. Hatanpaa, V. Vemireddy, C. A. Sheppard, D. Oliver, K. M. Hulsey, V. Tiwari, T. Mashimo, J. Battiste, S. Barnett, C. J. Madden, T. R. Patel, E. Pan, C. R. Malloy, B. E. Mickey, R. M. Bachoo, E. A. Maher, Prospective Longitudinal Analysis of 2-Hydroxyglutarate Magnetic Resonance Spectroscopy Identifies Broad Clinical Utility for the Management of Patients With IDH-Mutant Glioma. *J Clin Oncol* **34**, 4030-4039 (2016).

35. U. E. Emir, S. J. Larkin, N. de Pennington, N. Voets, P. Plaha, R. Stacey, K. Al-Qahtani, J. McCullagh, C. J. Schofield, S. Clare, P. Jezzard, T. Cadoux-Hudson, O. Ansorge, Noninvasive Quantification of 2-Hydroxyglutarate in Human Gliomas with IDH1 and IDH2 Mutations. *Cancer research* **76**, 43-49 (2016).

36. D. G. Gadian, G. K. Radda, NMR studies of tissue metabolism. *Annual review of biochemistry* **50**, 69-83 (1981).

37. Y. Zhang, E. Taub, N. Salibi, G. Uswatte, A. A. Maudsley, S. Sheriff, B. Womble, V. W. Mark, D. C. Knight, Comparison of reproducibility of single voxel spectroscopy and whole-brain magnetic resonance spectroscopy imaging at 3T. *NMR Biomed* **31**, e3898 (2018).

38. P. Bottomley, 4480228 Selective volume method for performing localized NMR spectroscopy. *Magn Reson Imag* **3**, iv-v (1985).

39. J. Frahm, H. Bruhn, M. L. Gyngell, K. D. Merboldt, W. Hanicke, R. Sauter, Localized high-resolution proton NMR spectroscopy using stimulated echoes: initial applications to human brain in vivo. *Magn Reson Med* **9**, 79-93 (1989).

40. C. T. Moonen, M. von Kienlin, P. C. van Zijl, J. Cohen, J. Gillen, P. Daly, G. Wolf, Comparison of single-shot localization methods (STEAM and PRESS) for in vivo proton NMR spectroscopy. *NMR Biomed* **2**, 201-208 (1989).

41. T. R. Brown, B. M. Kincaid, K. Ugurbil, NMR chemical shift imaging in three dimensions. *Proceedings of the National Academy of Sciences of the United States of America* **79**, 3523-3526 (1982).

42. O. A. Petroff, G. D. Graham, A. M. Blamire, M. al-Rayess, D. L. Rothman, P. B. Fayad, L. M. Brass, R. G. Shulman, J. W. Prichard, Spectroscopic imaging of stroke in humans: histopathology correlates of spectral changes. *Neurology* **42**, 1349-1354 (1992).

43. D. Bertholdo, A. Watcharakorn, M. Castillo, Brain proton magnetic resonance spectroscopy: introduction and overview. *Neuroimaging clinics of North America* **23**, 359-380 (2013).

44. U. Dydak, M. Weiger, K. P. Pruessmann, D. Meier, P. Boesiger, Sensitivity-encoded spectroscopic imaging. *Magn Reson Med* **46**, 713-722 (2001).

45. S. Posse, B. Schuknecht, M. E. Smith, P. C. van Zijl, N. Herschkowitz, C. T. Moonen, Short echo time proton MR spectroscopic imaging. *J Comput Assist Tomogr* **17**, 1-14 (1993).

46. S. Posse, C. DeCarli, D. Le Bihan, Three-dimensional echo-planar MR spectroscopic imaging at short echo times in the human brain. *Radiology* **192**, 733-738 (1994).

47. E. Adalsteinsson, P. Irarrazabal, S. Topp, C. Meyer, A. Macovski, D. M. Spielman, Volumetric spectroscopic imaging with spiral-based k-space trajectories. *Magn Reson Med* **39**, 889-898 (1998).

48. C. V. Schirda, T. Zhao, O. C. Andronesi, Y. Lee, J. W. Pan, J. M. Mountz, H. P. Hetherington, F. E. Boada, In vivo brain rosette spectroscopic imaging (RSI) with LASER excitation, constant gradient strength readout, and automated LCModel quantification for all voxels. *Magn Reson Med* **76**, 380-390 (2016).

49. S. Hu, M. Lustig, A. Balakrishnan, P. E. Larson, R. Bok, J. Kurhanewicz, S. J. Nelson, A. Goga, J. M. Pauly, D. B. Vigneron, 3D compressed sensing for highly accelerated hyperpolarized (13)C MRSI with in vivo applications to transgenic mouse models of cancer. *Magn Reson Med* **63**, 312-321 (2010).

50. F. H. Lin, S. Y. Tsai, R. Otazo, A. Caprihan, L. L. Wald, J. W. Belliveau, S. Posse, Sensitivity-encoded (SENSE) proton echo-planar spectroscopic imaging (PEPSI) in the human brain. *Magn Reson Med* **57**, 249-257 (2007).

51. E. Ozturk-Isik, A. P. Chen, J. C. Crane, W. Bian, D. Xu, E. T. Han, S. M. Chang, D. B. Vigneron, S. J. Nelson, 3D sensitivity encoded ellipsoidal MR spectroscopic imaging of gliomas at 3T. *Magn Reson Imaging* **27**, 1249-1257 (2009).

52. S. Bhave, R. Eslami, M. Jacob, Sparse spectral deconvolution algorithm for noncartesian MR spectroscopic imaging. *Magn Reson Med* **71**, 469-476 (2014).

53. S. Posse, G. Tedeschi, R. Risinger, R. Ogg, D. Le Bihan, High speed ^{1}H spectroscopic imaging in human brain by echo planar spatial-spectral encoding. *Magn Reson Med* **33**, 34-40 (1995).

54. M. K. Brix, L. Ersland, K. Hugdahl, R. Grüner, M.-B. Posserud, Å. Hammar, A. R. Craven, R. Noeske, C. J. Evans, H. B. Walker, T. Midtvedt, M. K. Beyer, "Brain MR spectroscopy in autism spectrum disorder—the GABA excitatory/inhibitory imbalance theory revisited". *Frontiers in human neuroscience* **9**, 365 (2015).

55. J. Horder, T. Lavender, M. A. Mendez, R. O'Gorman, E. Daly, M. C. Craig, D. J. Lythgoe, G. J. Barker, D. G. Murphy, Reduced subcortical glutamate/glutamine in adults with autism spectrum disorders: a [(1)H]MRS study. *Translational psychiatry* **4**, e364 (2014).

56. J. D. Port, N. Agarwal, MR spectroscopy in schizophrenia. *Journal of magnetic resonance imaging : JMRI* **34**, 1251-1261 (2011).

57. A. Marsman, R. C. W. Mandl, D. W. J. Klomp, M. M. Bohlken, V. O. Boer, A. Andreychenko, W. Cahn, R. S. Kahn, P. R. Luijten, H. E. Hulshoff Pol, GABA and glutamate in schizophrenia: A 7 T (1)H-MRS study. *NeuroImage : Clinical* **6**, 398-407 (2014).

58. P. B. Barker, D. O. Hearshen, M. D. Boska, Single-voxel proton MRS of the human brain at 1.5T and 3.0T. *Magn Reson Med* **45**, 765-769 (2001).

59. T. Murata, H. Kimura, M. Omori, H. Kado, H. Kosaka, T. Iidaka, H. Itoh, Y. Wada, MRI white matter hyperintensities, ^{1}H-MR spectroscopy and cognitive function in geriatric depression: a comparison of early- and late-onset cases. *International Journal of Geriatric Psychiatry* **16**, 1129-1135 (2001).

60. S. Posse, X. Hu, in *eMagRes*. (John Wiley & Sons, Ltd, 2007).

61. H. Zhu, R. Ouwerkerk, P. B. Barker, Dual-Band Water and Lipid Suppression for MR Spectroscopic Imaging at 3 Tesla. *Magnetic resonance in medicine : official journal of the Society of Magnetic Resonance in Medicine / Society of Magnetic Resonance in Medicine* **63**, 1486-1492 (2010).

62. V. O. Boer, D. W. J. Klomp, C. Juchem, P. R. Luijten, R. A. de Graaf, Multi-slice (1)H MRSI of the human brain at 7 Tesla using dynamic B(0) and B(1) shimming. *Magnetic resonance in medicine : official journal of the Society of Magnetic Resonance in Medicine / Society of Magnetic Resonance in Medicine* **68**, 662-670 (2012).

63. C. I. Haupt, N. Schuff, M. W. Weiner, A. A. Maudsley, Removal of lipid artifacts in ^{1}H spectroscopic imaging by data extrapolation. *Magn Reson Med* **35**, 678-687 (1996).

64. A. Ebel, A. A. Maudsley, Improved spectral quality for 3D MR spectroscopic imaging using a high spatial resolution acquisition strategy. *Magn Reson Imag* **21**, 113-120 (2003).

65. M. Donadieu, Y. Le Fur, A. Lecocq, A. A. Maudsley, S. Gherib, E. Soulier, S. Confort-Gouny, F. Pariollaud, M. P. Ranjeva, J. Pelletier, M. Guye, W. Zaaraoui, B. Audoin, J. P. Ranjeva, Metabolic voxel-based analysis of the complete human brain using fast 3D-MRSI: Proof of concept in multiple sclerosis. *Journal of magnetic resonance imaging : JMRI* **44**, 411-419 (2016).

66. H. S. Gutowsky, D. W. McCall, C. P. Slichter, Nuclear Magnetic Resonance Multiplets in Liquids. *The Journal of chemical physics* **21**, 279-292 (1953).

67. D. Ziessow, R. R. Ernst, G. Bodenhausen u. A. Wokaun: Principles of Nuclear Magnetic Resonance in One and Two Dimensions, Clarendon Press, Oxford 1987. 610 Seiten. *Berichte der Bunsengesellschaft für physikalische Chemie* **92**, 1563-1565 (1988).

68. R. B. Thompson, P. S. Allen, Sources of variability in the response of coupled spins to the PRESS sequence and their potential impact on metabolite quantification. *Magn Reson Med* **41**, 1162-1169 (1999).

69. T. W. M. Fan, Metabolite profiling by one- and two-dimensional NMR analysis of complex mixtures. *Progress in Nuclear Magnetic Resonance Spectroscopy* **28**, 161-219 (1996).

70. V. Govindaraju, K. Young, A. A. Maudsley, Proton NMR chemical shifts and coupling constants for brain metabolites. *NMR Biomed* **13**, 129-153 (2000).

71. D. Bal, A. Gryff-Keller, ^{1}H and ^{13}C NMR study of 2-hydroxyglutaric acid and its lactone. *Magnetic Resonance in Chemistry* **40**, 533-536 (2002).

72. O. W. Sørensen, G. W. Eich, M. H. Levitt, G. Bodenhausen, R. R. Ernst, Product operator formalism for the description of NMR pulse experiments. *Progress in Nuclear Magnetic Resonance Spectroscopy* **16**, 163-192 (1984).

73. M. H. Levitt, R. Freeman, NMR population inversion using a composite pulse. *Journal of Magnetic Resonance (1969)* **33**, 473-476 (1979).

74. R. Freeman, S. P. Kempsell, M. H. Levitt, Radiofrequency pulse sequences which compensate their own imperfections. *Journal of Magnetic Resonance (1969)* **38**, 453-479 (1980).

75. J. Jeener, B. H. Meier, P. Bachmann, R. R. Ernst, Investigation of exchange processes by two-dimensional NMR spectroscopy. *The Journal of chemical physics* **71**, 4546-4553 (1979).

76. G. Bodenhausen, R. R. Ernst, Direct determination of rate constants of slow dynamic processes by two-dimensional "accordion" spectroscopy in nuclear magnetic resonance. *Journal of the American Chemical Society* **104**, 1304-1309 (1982).

77. H. R. Brooker, NMR imaging in biomedicine: P. Mansfield and P. G. Morris. Academic Press, New York, 1982. 337 pages. $49.50. *Journal of Magnetic Resonance (1969)* **53**, 167 (1983).

78. G. A. Morris, R. Freeman, Enhancement of nuclear magnetic resonance signals by polarization transfer. *Journal of the American Chemical Society* **101**, 760-762 (1979).

79. D. P. Burum, R. R. Ernst, Net polarization transfer via a J-ordered state for signal enhancement of low-sensitivity nuclei. *Journal of Magnetic Resonance (1969)* **39**, 163-168 (1980).

80. G. A. Morris, Sensitivity enhancement in nitrogen-15 NMR: polarization transfer using the INEPT pulse sequence. *Journal of the American Chemical Society* **102**, 428-429 (1980).

81. T. Tong, Z. Yang, J. W. Chen, J. Zhu, Z. Yao, Dynamic ^{1}H-MRS assessment of brain tumors: a novel approach for differential diagnosis of glioma. *Oncotarget* **6**, 32257-32265 (2015).

82. E. Roldan-Valadez, C. Rios, D. Motola-Kuba, J. Matus-Santos, A. R. Villa, S. Moreno-Jimenez, Choline-to-N-acetyl aspartate and lipids-lactate-to-creatine ratios together with age assemble a significant Cox's proportional-hazards regression model for prediction of survival in high-grade gliomas. *The British journal of radiology* **89**, 20150502 (2016).

83. S. Salice, R. Esposito, D. Ciavardelli, S. Delli Pizzi, R. di Bastiano, A. Tartaro, Combined 3 Tesla MRI Biomarkers Improve the Differentiation between Benign vs Malignant Single Ring Enhancing Brain Masses. *PloS one* **11**, e0159047 (2016).

84. Y. J. Xu, Y. Cui, H. X. Li, W. Q. Shi, F. Y. Li, J. Z. Wang, Q. S. Zeng, Noninvasive evaluation of radiation-enhanced glioma cells invasiveness by ultra-high-field (1)H-MRS in vitro. *Magn Reson Imaging* **34**, 1121-1127 (2016).

85. D. Carlin, B. Babourina-Brooks, N. P. Davies, M. Wilson, A. C. Peet, Variation of T2 relaxation times in pediatric brain tumors and their effect on metabolite quantification. *Journal of magnetic resonance imaging : JMRI*, (2018).

86. A. Horska, P. B. Barker, Imaging of brain tumors: MR spectroscopy and metabolic imaging. *Neuroimaging clinics of North America* **20**, 293-310 (2010).

87. S. S. Lu, S. J. Kim, H. S. Kim, C. G. Choi, Y. M. Lim, E. J. Kim, D. Y. Kim, S. H. Cho, Utility of proton MR spectroscopy for differentiating typical and atypical primary central nervous system lymphomas from tumefactive demyelinating lesions. *AJNR. American journal of neuroradiology* **35**, 270-277 (2014).

88. O. C. Andronesi, G. S. Kim, E. Gerstner, T. Batchelor, A. A. Tzika, V. R. Fantin, M. G. Vander Heiden, A. G. Sorensen, Detection of 2-hydroxyglutarate in IDH-mutated glioma patients by in

vivo spectral-editing and 2D correlation magnetic resonance spectroscopy. *Science translational medicine* **4**, 116ra114 (2012).

89. W. B. Pope, R. M. Prins, M. Albert Thomas, R. Nagarajan, K. E. Yen, M. A. Bittinger, N. Salamon, A. P. Chou, W. H. Yong, H. Soto, N. Wilson, E. Driggers, H. G. Jang, S. M. Su, D. P. Schenkein, A. Lai, T. F. Cloughesy, H. I. Kornblum, H. Wu, V. R. Fantin, L. M. Liau, Non-invasive detection of 2-hydroxyglutarate and other metabolites in IDH1 mutant glioma patients using magnetic resonance spectroscopy. *Journal of neuro-oncology* **107**, 197-205 (2012).

90. C. Choi, S. Ganji, K. Hulsey, A. Madan, Z. Kovacs, I. Dimitrov, S. Zhang, K. Pichumani, D. Mendelsohn, B. Mickey, C. Malloy, R. Bachoo, R. Deberardinis, E. Maher, A comparative study of short- and long-TE (1)H MRS at 3 T for in vivo detection of 2-hydroxyglutarate in brain tumors. *NMR Biomed* **26**, 1242-1250 (2013).

91. O. C. Andronesi, F. Loebel, W. Bogner, M. Marjańska, M. G. Vander Heiden, A. J. Iafrate, J. Dietrich, T. T. Batchelor, E. R. Gerstner, W. G. Kaelin, A. S. Chi, B. R. Rosen, D. P. Cahill, Treatment Response Assessment in IDH-Mutant Glioma Patients by Noninvasive 3D Functional Spectroscopic Mapping of 2-Hydroxyglutarate. *Clinical Cancer Research* **22**, 1632-1641 (2016).

92. C. H. Choi, J. M. Raisanen, S. K. Ganji, S. Zhang, S. S. McNeil, Z. X. An, A. Madan, K. J. Hatanpaa, V. Vemireddy, C. A. Sheppard, D. Oliver, K. M. Hulsey, V. Tiwari, T. Mashimo, J. Battiste, S. Barnett, C. J. Madden, T. R. Patel, E. Pan, C. R. Malloy, B. E. Mickey, R. M. Bachoo, E. A. Maher, Prospective Longitudinal Analysis of 2-Hydroxyglutarate Magnetic Resonance Spectroscopy Identifies Broad Clinical Utility for the Management of Patients With IDH-Mutant Glioma. *J Clin Oncol* **34**, 4030-U4157 (2016).

93. Z. An, V. Tiwari, S. K. Ganji, J. Baxter, M. Levy, M. C. Pinho, E. Pan, E. A. Maher, T. R. Patel, B. E. Mickey, C. Choi, Echo-planar spectroscopic imaging with dual-readout alternated gradients (DRAG-EPSI) at 7 T: Application for 2-hydroxyglutarate imaging in glioma patients. *Magn Reson Med* **79**, 1851-1861 (2018).

94. C. Choi, S. K. Ganji, R. J. DeBerardinis, I. E. Dimitrov, J. M. Pascual, R. Bachoo, B. E. Mickey, C. R. Malloy, E. A. Maher, Measurement of glycine in the human brain in vivo by ^{1}H-MRS at 3 T: application in brain tumors. *Magn Reson Med* **66**, 609-618 (2011).

95. A. Banerjee, S. Ganji, K. Hulsey, I. Dimitrov, E. Maher, S. Ghose, C. Tamminga, C. Choi, Measurement of glycine in gray and white matter in the human brain in vivo by ^{1}H MRS at 7.0 T. *Magn Reson Med* **68**, 325-331 (2012).

96. S. K. Ganji, E. A. Maher, C. Choi, In vivo (1)H MR Spectroscopic Imaging of Glycine in Brain Tumors at 3T. *Magn Reson Med* **75**, 52-62 (2016).

97. V. Tiwari, Z. An, S. K. Ganji, J. Baxter, T. R. Patel, E. Pan, B. E. Mickey, E. A. Maher, M. C. Pinho, C. Choi, Measurement of glycine in healthy and tumorous brain by triple-refocusing MRS at 3 T in vivo. *NMR Biomed* **30**, (2017).

98. C. Choi, N. J. Coupland, S. Kalra, P. P. Bhardwaj, N. Malykhin, P. S. Allen, Proton spectral editing for discrimination of lactate and threonine 1.31 ppm resonances in human brain in vivo. *Magn Reson Med* **56**, 660-665 (2006).

99. A. Madan, S. K. Ganji, Z. An, K. S. Choe, M. C. Pinho, R. M. Bachoo, E. M. Maher, C. Choi, Proton T2 measurement and quantification of lactate in brain tumors by MRS at 3 Tesla in vivo. *Magn Reson Med* **73**, 2094-2099 (2015).

100. C. Choi, S. K. Ganji, A. Madan, K. M. Hulsey, Z. An, S. Zhang, M. C. Pinho, R. J. DeBerardinis, R. M. Bachoo, E. A. Maher, In vivo detection of citrate in brain tumors by ^{1}H magnetic resonance spectroscopy at 3T. *Magn Reson Med* **72**, 316-323 (2014).

101. S. Bluml, A. Panigrahy, M. Laskov, G. Dhall, M. D. Krieger, M. D. Nelson, J. L. Finlay, F. H. Gilles, Elevated citrate in pediatric astrocytomas with malignant progression. *Neuro-oncology* **13**, 1107-1117 (2011).

102. Z. A. Seymour, A. Panigrahy, J. L. Finlay, M. D. Nelson, Jr., S. Bluml, Citrate in pediatric CNS tumors? *AJNR. American journal of neuroradiology* **29**, 1006-1011 (2008).

103. H. Nagashima, T. Sasayama, K. Tanaka, K. Kyotani, N. Sato, M. Maeyama, M. Kohta, J. Sakata, Y. Yamamoto, K. Hosoda, T. Itoh, R. Sasaki, E. Kohmura, Myo-inositol concentration in MR spectroscopy for differentiating high grade glioma from primary central nervous system lymphoma. *Journal of neuro-oncology* **136**, 317-326 (2018).

104. M. Gottschalk, I. Tropres, L. Lamalle, S. Grand, J. F. Le Bas, C. Segebarth, Refined modelling of the short-T2 signal component and ensuing detection of glutamate and glutamine in short-TE, localised, (1) H MR spectra of human glioma measured at 3 T. *NMR Biomed* **29**, 943-951 (2016).

105. H. Nagashima, K. Tanaka, T. Sasayama, Y. Irino, N. Sato, Y. Takeuchi, K. Kyotani, A. Mukasa, K. Mizukawa, J. Sakata, Y. Yamamoto, K. Hosoda, T. Itoh, R. Sasaki, E. Kohmura, Diagnostic value of glutamate with 2-hydroxyglutarate in magnetic resonance spectroscopy for IDH1 mutant glioma. *Neuro-oncology* **18**, 1559-1568 (2016).

106. S. Ramadan, A. Lin, P. Stanwell, Glutamate and glutamine: a review of in vivo MRS in the human brain. *NMR Biomed* **26**, 1630-1646 (2013).

107. L. Dang, D. W. White, S. Gross, B. D. Bennett, M. A. Bittinger, E. M. Driggers, V. R. Fantin, H. G. Jang, S. Jin, M. C. Keenan, K. M. Marks, R. M. Prins, P. S. Ward, K. E. Yen, L. M. Liau, J. D. Rabinowitz, L. C. Cantley, C. B. Thompson, M. G. Vander Heiden, S. M. Su, Cancer-associated IDH1 mutations produce 2-hydroxyglutarate. *Nature* **462**, 739-744 (2009).

108. D. J. Brat, R. G. Verhaak, K. D. Aldape, W. K. Yung, S. R. Salama, L. A. Cooper, E. Rheinbay, C. R. Miller, M. Vitucci, O. Morozova, A. G. Robertson, H. Noushmehr, P. W. Laird, A. D. Cherniack, R. Akbani, J. T. Huse, G. Ciriello, L. M. Poisson, J. S. Barnholtz-Sloan, M. S. Berger, C. Brennan, R. R. Colen, H. Colman, A. E. Flanders, C. Giannini, M. Grifford, A. Iavarone, R. Jain, I. Joseph, J. Kim, K. Kasaian, T. Mikkelsen, B. A. Murray, B. P. O'Neill, L. Pachter, D. W. Parsons, C. Sougnez, E. P. Sulman, S. R. Vandenberg, E. G. Van Meir, A. von Deimling, H. Zhang, D. Crain, K. Lau, D. Mallery, S. Morris, J. Paulauskis, R. Penny, T. Shelton, M. Sherman, P. Yena, A. Black, J. Bowen, K. Dicostanzo, J. Gastier-Foster, K. M. Leraas, T. M. Lichtenberg, C. R. Pierson, N. C. Ramirez, C. Taylor, S. Weaver, L. Wise, E. Zmuda, T. Davidsen, J. A. Demchok, G. Eley, M. L. Ferguson, C. M. Hutter, K. R. Mills Shaw, B. A. Ozenberger, M. Sheth, H. J. Sofia, R. Tarnuzzer, Z. Wang, L. Yang, J. C. Zenklusen, B. Ayala, J. Baboud, S. Chudamani, M. A. Jensen, J. Liu, T. Pihl, R. Raman, Y. Wan, Y. Wu, A. Ally, J. T. Auman, M. Balasundaram, S. Balu, S. B. Baylin, R. Beroukhim, M. S. Bootwalla, R. Bowlby, C. A. Bristow, D. Brooks, Y. Butterfield, R. Carlsen, S. Carter, L. Chin, A. Chu, E. Chuah, K. Cibulskis, A. Clarke, S. G. Coetzee, N. Dhalla, T. Fennell, S. Fisher, S. Gabriel, G. Getz, R. Gibbs, R. Guin, A. Hadjipanayis, D. N. Hayes, T. Hinoue, K. Hoadley, R. A. Holt, A. P. Hoyle, S. R. Jefferys, S. Jones, C. D. Jones, R. Kucherlapati, P. H. Lai, E. Lander, S. Lee, L. Lichtenstein, Y. Ma, D. T. Maglinte, H. S. Mahadeshwar, M. A. Marra, M. Mayo, S. Meng, M. L. Meyerson, P. A. Mieczkowski, R. A. Moore, L. E. Mose, A. J. Mungall, A. Pantazi, M. Parfenov, P. J. Park, J. S. Parker, C. M. Perou, A. Protopopov, X. Ren, J. Roach, T. S. Sabedot, J. Schein, S. E. Schumacher, J. G. Seidman, S. Seth, H. Shen, J. V. Simons, P. Sipahimalani, M. G. Soloway, X. Song, H. Sun, B. Tabak, A. Tam, D. Tan, J. Tang, N. Thiessen, T. Triche, Jr., D. J. Van Den Berg, U. Veluvolu, S. Waring, D. J. Weisenberger, M. D. Wilkerson, T. Wong, J. Wu, L. Xi, A. W. Xu, L. Yang, T. I. Zack, J. Zhang, B. A. Aksoy, H. Arachchi, C. Benz, B. Bernard, D. Carlin, J. Cho, D. DiCara, S. Frazer, G. N. Fuller, J. Gao, N. Gehlenborg, D. Haussler, D. I. Heiman, L. Iype, A. Jacobsen, Z. Ju, S. Katzman, H. Kim, T. Knijnenburg, R. B.

Kreisberg, M. S. Lawrence, W. Lee, K. Leinonen, P. Lin, S. Ling, W. Liu, Y. Liu, Y. Liu, Y. Lu, G. Mills, S. Ng, M. S. Noble, E. Paull, A. Rao, S. Reynolds, G. Saksena, Z. Sanborn, C. Sander, N. Schultz, Y. Senbabaoglu, R. Shen, I. Shmulevich, R. Sinha, J. Stuart, S. O. Sumer, Y. Sun, N. Tasman, B. S. Taylor, D. Voet, N. Weinhold, J. N. Weinstein, D. Yang, K. Yoshihara, S. Zheng, W. Zhang, L. Zou, T. Abel, S. Sadeghi, M. L. Cohen, J. Eschbacher, E. M. Hattab, A. Raghunathan, M. J. Schniederjan, D. Aziz, G. Barnett, W. Barrett, D. D. Bigner, L. Boice, C. Brewer, C. Calatozzolo, B. Campos, C. G. Carlotti, Jr., T. A. Chan, L. Cuppini, E. Curley, S. Cuzzubbo, K. Devine, F. DiMeco, R. Duell, J. B. Elder, A. Fehrenbach, G. Finocchiaro, W. Friedman, J. Fulop, J. Gardner, B. Hermes, C. Herold-Mende, C. Jungk, A. Kendler, N. L. Lehman, E. Lipp, O. Liu, R. Mandt, M. McGraw, R. McLendon, C. McPherson, L. Neder, P. Nguyen, A. Noss, R. Nunziata, Q. T. Ostrom, C. Palmer, A. Perin, B. Pollo, A. Potapov, O. Potapova, W. K. Rathmell, D. Rotin, L. Scarpace, C. Schilero, K. Senecal, K. Shimmel, V. Shurkhay, S. Sifri, R. Singh, A. E. Sloan, K. Smolenski, S. M. Staugaitis, R. Steele, L. Thorne, D. P. Tirapelli, A. Unterberg, M. Vallurupalli, Y. Wang, R. Warnick, F. Williams, Y. Wolinsky, S. Bell, M. Rosenberg, C. Stewart, F. Huang, J. L. Grimsby, A. J. Radenbaugh, J. Zhang, Comprehensive, Integrative Genomic Analysis of Diffuse Lower-Grade Gliomas. *The New England journal of medicine* **372**, 2481-2498 (2015).

109. J. E. Eckel-Passow, D. H. Lachance, A. M. Molinaro, K. M. Walsh, P. A. Decker, H. Sicotte, M. Pekmezci, T. Rice, M. L. Kosel, I. V. Smirnov, G. Sarkar, A. A. Caron, T. M. Kollmeyer, C. E. Praska, A. R. Chada, C. Halder, H. M. Hansen, L. S. McCoy, P. M. Bracci, R. Marshall, S. Zheng, G. F. Reis, A. R. Pico, B. P. O'Neill, J. C. Buckner, C. Giannini, J. T. Huse, A. Perry, T. Tihan, M. S. Berger, S. M. Chang, M. D. Prados, J. Wiemels, J. K. Wiencke, M. R. Wrensch, R. B. Jenkins, Glioma Groups Based on 1p/19q, IDH, and TERT Promoter Mutations in Tumors. *The New England journal of medicine* **372**, 2499-2508 (2015).

110. H. Suzuki, K. Aoki, K. Chiba, Y. Sato, Y. Shiozawa, Y. Shiraishi, T. Shimamura, A. Niida, K. Motomura, F. Ohka, T. Yamamoto, K. Tanahashi, M. Ranjit, T. Wakabayashi, T. Yoshizato, K. Kataoka, K. Yoshida, Y. Nagata, A. Sato-Otsubo, H. Tanaka, M. Sanada, Y. Kondo, H. Nakamura, M. Mizoguchi, T. Abe, Y. Muragaki, R. Watanabe, I. Ito, S. Miyano, A. Natsume, S. Ogawa, Mutational landscape and clonal architecture in grade II and III gliomas. *Nature genetics* **47**, 458-468 (2015).

111. D. N. Louis, A. Perry, G. Reifenberger, A. von Deimling, D. Figarella-Branger, W. K. Cavenee, H. Ohgaki, O. D. Wiestler, P. Kleihues, D. W. Ellison, The 2016 World Health Organization Classification of Tumors of the Central Nervous System: a summary. *Acta Neuropathol* **131**, 803-820 (2016).

112. J. Mondesir, C. Willekens, M. Touat, S. de Botton, IDH1 and IDH2 mutations as novel therapeutic targets: current perspectives. *Journal of blood medicine* **7**, 171-180 (2016).

113. F. A. Howe, K. S. Opstad, ^{1}H MR spectroscopy of brain tumours and masses. *NMR Biomed* **16**, 123-131 (2003).

114. M. Esmaeili, B. C. Hamans, A. C. Navis, R. van Horssen, T. F. Bathen, I. S. Gribbestad, W. P. Leenders, A. Heerschap, IDH1 R132H mutation generates a distinct phospholipid metabolite profile in glioma. *Cancer research* **74**, 4898-4907 (2014).

115. A. C. Navis, S. P. Niclou, F. Fack, D. Stieber, S. van Lith, K. Verrijp, A. Wright, J. Stauber, B. Tops, I. Otte-Holler, R. A. Wevers, A. van Rooij, S. Pusch, A. von Deimling, W. Tigchelaar, C. J. van Noorden, P. Wesseling, W. P. Leenders, Increased mitochondrial activity in a novel IDH1-R132H mutant human oligodendroglioma xenograft model: in situ detection of 2-HG and alpha-KG. *Acta neuropathologica communications* **1**, 18 (2013).

116. M. L. Simmons, C. G. Frondoza, J. T. Coyle, Immunocytochemical localization of N-acetyl-aspartate with monoclonal antibodies. *Neuroscience* **45**, 37-45 (1991).

117. N. De Stefano, S. Narayanan, G. S. Francis, R. Arnaoutelis, M. C. Tartaglia, J. P. Antel, P. M. Matthews, D. L. Arnold, Evidence of axonal damage in the early stages of multiple sclerosis and its relevance to disability. *Archives of neurology* **58**, 65-70 (2001).

118. P. Legendre, The glycinergic inhibitory synapse. *Cellular and molecular life sciences : CMLS* **58**, 760-793 (2001).

119. V. Eulenburg, W. Armsen, H. Betz, J. Gomeza, Glycine transporters: essential regulators of neurotransmission. *Trends in biochemical sciences* **30**, 325-333 (2005).

120. D. C. Javitt, Glutamate and schizophrenia: phencyclidine, N-methyl-D-aspartate receptors, and dopamine-glutamate interactions. *International review of neurobiology* **78**, 69-108 (2007).

121. B. Bobek-Billewicz, A. Hebda, G. Stasik-Pres, K. Majchrzak, E. Zmuda, A. Trojanowska, Measurement of glycine in a brain and brain tumors by means of ^{1}H MRS. *Folia neuropathologica* **48**, 190-199 (2010).

122. T. L. Perry, N. Urquhart, S. Hansen, Studies of the glycine cleavage enzyme system in brain from infants with glycine encephalopathy. *Pediatric research* **11**, 1192-1197 (1977).

123. F. G. Lehnhardt, C. Bock, G. Rohn, R. I. Ernestus, M. Hoehn, Metabolic differences between primary and recurrent human brain tumors: a ^{1}H NMR spectroscopic investigation. *NMR Biomed* **18**, 371-382 (2005).

124. E. Hattingen, H. Lanfermann, J. Quick, K. Franz, F. E. Zanella, U. Pilatus, ^{1}H MR spectroscopic imaging with short and long echo time to discriminate glycine in glial tumours. *Magma* **22**, 33-41 (2009).

125. M. Jain, R. Nilsson, S. Sharma, N. Madhusudhan, T. Kitami, A. L. Souza, R. Kafri, M. W. Kirschner, C. B. Clish, V. K. Mootha, Metabolite profiling identifies a key role for glycine in rapid cancer cell proliferation. *Science* **336**, 1040-1044 (2012).

126. M. Tomita, K. Kami, Cancer. Systems biology, metabolomics, and cancer metabolism. *Science* **336**, 990-991 (2012).

127. A. P. Prescot, B. F. B. de, L. Wang, J. Brown, J. E. Jensen, M. J. Kaufman, P. F. Renshaw, In vivo detection of brain glycine with echo-time-averaged (1)H magnetic resonance spectroscopy at 4.0 T. *Magn Reson Med* **55**, 681-686 (2006).

128. C. Choi, P. P. Bhardwaj, P. Seres, S. Kalra, P. G. Tibbo, N. J. Coupland, Measurement of glycine in human brain by triple refocusing ^{1}H-MRS in vivo at 3.0T. *Magn Reson Med* **59**, 59-64 (2008).

129. S. K. Ganji, E. A. Maher, C. Choi, In vivo (1)H MRSI of glycine in brain tumors at 3T. *Magn Reson Med* **75**, 52-62 (2016).

130. O. Warburg, The Metabolism of Carcinoma Cells. *The Journal of Cancer Research* **9**, 148-163 (1925).

131. O. Warburg, F. Wind, E. Negelein, THE METABOLISM OF TUMORS IN THE BODY. *The Journal of General Physiology* **8**, 519-530 (1927).

132. F. Hirschhaeuser, U. G. Sattler, W. Mueller-Klieser, Lactate: a metabolic key player in cancer. *Cancer research* **71**, 6921-6925 (2011).

133. T. Ziebart, S. Walenta, M. Kunkel, T. E. Reichert, W. Wagner, W. Mueller-Klieser, Metabolic and proteomic differentials in head and neck squamous cell carcinomas and normal gingival tissue. *Journal of cancer research and clinical oncology* **137**, 193-199 (2011).

134. S. Walenta, W. F. Mueller-Klieser, Lactate: mirror and motor of tumor malignancy. *Seminars in radiation oncology* **14**, 267-274 (2004).

135. D. A. Kelley, L. L. Wald, J. M. Star-Lack, Lactate detection at 3T: compensating J coupling effects with BASING. *Journal of magnetic resonance imaging : JMRI* **9**, 732-737 (1999).

136. R. E. Hurd, D. Freeman, Proton editing and imaging of lactate. *NMR Biomed* **4**, 73-80 (1991).

137. H. Hu, N. Takano, L. Xiang, D. M. Gilkes, W. Luo, G. L. Semenza, Hypoxia-inducible factors enhance glutamate signaling in cancer cells. *Oncotarget* **5**, 8853-8868 (2014).

138. A. Blanchart, R. Fernando, M. Haring, N. Assaife-Lopes, R. A. Romanov, M. Andang, T. Harkany, P. Ernfors, Endogenous GABAA receptor activity suppresses glioma growth. *Oncogene* **36**, 777-786 (2017).

139. V. Tiwari, Z. An, Y. Wang, C. Choi, Distinction of the GABA 2.29 ppm resonance using triple refocusing at 3 T in vivo. *Magn Reson Med*, (2018).

140. A. R. Mullen, W. W. Wheaton, E. S. Jin, P. H. Chen, L. B. Sullivan, T. Cheng, Y. Yang, W. M. Linehan, N. S. Chandel, R. J. DeBerardinis, Reductive carboxylation supports growth in tumour cells with defective mitochondria. *Nature* **481**, 385-388 (2011).

141. P. Icard, L. Poulain, H. Lincet, Understanding the central role of citrate in the metabolism of cancer cells. *Biochimica et biophysica acta* **1825**, 111-116 (2012).

142. J. Balss, J. Meyer, W. Mueller, A. Korshunov, C. Hartmann, A. von Deimling, Analysis of the IDH1 codon 132 mutation in brain tumors. *Acta Neuropathol* **116**, 597-602 (2008).

143. M. I. de la Fuente, R. J. Young, J. Rubel, M. Rosenblum, J. Tisnado, S. Briggs, J. Arevalo-Perez, J. R. Cross, C. Campos, K. Straley, D. Zhu, C. Dong, A. Thomas, A. A. Omuro, C. P. Nolan, E. Pentsova, T. J. Kaley, J. H. Oh, R. Noeske, E. Maher, C. Choi, P. H. Gutin, A. I. Holodny, K. Yen, L. M. DeAngelis, I. K. Mellinghoff, S. B. Thakur, Integration of 2-hydroxyglutarate-proton magnetic resonance spectroscopy into clinical practice for disease monitoring in isocitrate dehydrogenase-mutant glioma. *Neuro-oncology* **18**, 283-290 (2016).

144. A. Henning, A. Fuchs, J. B. Murdoch, P. Boesiger, Slice-selective FID acquisition, localized by outer volume suppression (FIDLOVS) for (1)H-MRSI of the human brain at 7 T with minimal signal loss. *NMR Biomed* **22**, 683-696 (2009).

145. D. Bal, W. Gradowska, A. Gryff-Keller, Determination of the absolute configuration of 2-hydroxyglutaric acid and 5-oxoproline in urine samples by high-resolution NMR spectroscopy in the presence of chiral lanthanide complexes. *Journal of pharmaceutical and biomedical analysis* **28**, 1061-1071 (2002).

146. L. G. Kaiser, K. Young, D. J. Meyerhoff, S. G. Mueller, G. B. Matson, A detailed analysis of localized J-difference GABA editing: theoretical and experimental study at 4 T. *NMR Biomed* **21**, 22-32 (2008).

147. S. W. Provencher, Estimation of metabolite concentrations from localized in vivo proton NMR spectra. *Magn Reson Med* **30**, 672-679 (1993).

148. S. K. Ganji, A. Banerjee, A. M. Patel, Y. D. Zhao, I. E. Dimitrov, J. D. Browning, E. S. Brown, E. A. Maher, C. Choi, T2 measurement of J-coupled metabolites in the human brain at 3T. *NMR Biomed* **25**, 523-529 (2012).

149. V. Mlynarik, S. Gruber, E. Moser, Proton T (1) and T (2) relaxation times of human brain metabolites at 3 Tesla. *NMR Biomed* **14**, 325-331 (2001).

150. F. Traber, W. Block, R. Lamerichs, J. Gieseke, H. H. Schild, ^{1}H metabolite relaxation times at 3.0 tesla: Measurements of T1 and T2 values in normal brain and determination of regional differences in transverse relaxation. *Journal of magnetic resonance imaging : JMRI* **19**, 537-545 (2004).

151. S. K. Ganji, Z. An, A. Banerjee, A. Madan, K. M. Hulsey, C. Choi, Measurement of regional variation of GABA in the human brain by optimized point-resolved spectroscopy at 7 T in vivo. *NMR Biomed* **27**, 1167-1175 (2014).

152. A. Elkhaled, L. E. Jalbert, J. J. Phillips, H. A. I. Yoshihara, R. Parvataneni, R. Srinivasan, G. Bourne, M. S. Berger, S. M. Chang, S. Cha, S. J. Nelson, Magnetic resonance of 2-hydroxyglutarate in IDH1-mutated low-grade gliomas. *Science translational medicine* **4**, 116ra115 (2012).

153. D. Rohle, J. Popovici-Muller, N. Palaskas, S. Turcan, C. Grommes, C. Campos, J. Tsoi, O. Clark, B. Oldrini, E. Komisopoulou, K. Kunii, A. Pedraza, S. Schalm, L. Silverman, A. Miller, F. Wang, H. Yang, Y. Chen, A. Kernytsky, M. K. Rosenblum, W. Liu, S. A. Biller, S. M. Su, C. W. Brennan, T. A. Chan, T. G. Graeber, K. E. Yen, I. K. Mellinghoff, An inhibitor of mutant IDH1 delays growth and promotes differentiation of glioma cells. *Science* **340**, 626-630 (2013).

154. Z. An, S. K. Ganji, V. Tiwari, M. C. Pinho, T. Patel, S. Barnett, E. Pan, B. E. Mickey, E. A. Maher, C. Choi, Detection of 2-hydroxyglutarate in brain tumors by triple-refocusing MR spectroscopy at 3T in vivo. *Magn Reson Med* **78**, 40-48 (2017).

155. O. C. Andronesi, F. Loebel, W. Bogner, M. Marjanska, M. G. Vander Heiden, A. J. Iafrate, J. Dietrich, T. T. Batchelor, E. R. Gerstner, W. G. Kaelin, A. S. Chi, B. R. Rosen, D. P. Cahill, Treatment Response Assessment in IDH-Mutant Glioma Patients by Noninvasive 3D Functional Spectroscopic Mapping of 2-Hydroxyglutarate. *Clinical cancer research : an official journal of the American Association for Cancer Research* **22**, 1632-1641 (2016).

156. P. Masnsfield, Spatial mapping of the chemical shift in NMR. *Magn Reson Chem* **1**, 370-386 (1984).

157. R. Otazo, B. Mueller, K. Ugurbil, L. Wald, S. Posse, Signal-to-noise ratio and spectral linewidth improvements between 1.5 and 7 Tesla in proton echo-planar spectroscopic imaging. *Magn Reson Med* **56**, 1200-1210 (2006).

158. C. H. Cunningham, D. B. Vigneron, A. P. Chen, D. Xu, S. J. Nelson, R. E. Hurd, D. A. Kelley, J. M. Pauly, Design of flyback echo-planar readout gradients for magnetic resonance spectroscopic imaging. *Magn Reson Med* **54**, 1286-1289 (2005).

159. S. Matsui, K. Sekihara, H. Kohno, Spatially resolved NMR spectroscopy using phase-modulated spin-echo trains. *Journal of magnetic resonance* **67**, 476-490 (1986).

160. M. J. Versluis, H. E. Kan, M. A. van Buchem, A. G. Webb, Improved signal to noise in proton spectroscopy of the human calf muscle at 7 T using localized B1 calibration. *Magnetic resonance in medicine : official journal of the Society of Magnetic Resonance in Medicine / Society of Magnetic Resonance in Medicine* **63**, 207-211 (2010).

161. A. Ebel, A. A. Maudsley, Detection and correction of frequency instabilities for volumetric ^{1}H echo-planar spectroscopic imaging. *Magn Reson Med* **53**, 465-469 (2005).

162. L. Xin, B. Schaller, V. Mlynarik, H. Lu, R. Gruetter, Proton T1 relaxation times of metabolites in human occipital white and gray matter at 7 T. *Magn Reson Med* **69**, 931-936 (2013).

163. C. J. Pirozzi, Z. J. Reitman, H. Yan, Releasing the block: setting differentiation free with mutant IDH inhibitors. *Cancer cell* **23**, 570-572 (2013).

164. L. Dang, K. Yen, E. C. Attar, IDH mutations in cancer and progress toward development of targeted therapeutics. *Annals of oncology : official journal of the European Society for Medical Oncology* **27**, 599-608 (2016).

165. K. Jafari-Khouzani, F. Loebel, W. Bogner, O. Rapalino, G. R. Gonzalez, E. Gerstner, A. S. Chi, T. T. Batchelor, B. R. Rosen, J. Unkelbach, H. A. Shih, D. P. Cahill, O. C. Andronesi, Volumetric

relationship between 2-hydroxyglutarate and FLAIR hyperintensity has potential implications for radiotherapy planning of mutant IDH glioma patients. *Neuro-oncology* **18**, 1569-1578 (2016).

166. I. Tkac, G. Oz, G. Adriany, K. Ugurbil, R. Gruetter, In vivo ^{1}H NMR spectroscopy of the human brain at high magnetic fields: metabolite quantification at 4T vs. 7T. *Magn Reson Med* **62**, 868-879 (2009).

167. R. Mekle, V. Mlynarik, G. Gambarota, M. Hergt, G. Krueger, R. Gruetter, MR spectroscopy of the human brain with enhanced signal intensity at ultrashort echo times on a clinical platform at 3T and 7T. *Magn Reson Med* **61**, 1279-1285 (2009).

168. C. Choi, J. M. Raisanen, S. K. Ganji, S. Zhang, S. S. McNeil, Z. An, A. Madan, K. J. Hatanpaa, V. Vemireddy, C. A. Sheppard, D. Oliver, K. M. Hulsey, V. Tiwari, T. Mashimo, J. Battiste, S. Barnett, C. J. Madden, T. R. Patel, E. Pan, C. R. Malloy, B. E. Mickey, R. M. Bachoo, E. A. Maher, Prospective Longitudinal Analysis of 2-Hydroxyglutarate Magnetic Resonance Spectroscopy Identifies Broad Clinical Utility for the Management of Patients With IDH-Mutant Glioma. *Journal of Clinical Oncology* **34**, 4030-4039 (2016).

169. C. Choi, T. Huber, A. Tietze, B. S. Choi, J. H. Lee, S. K. Lee, A. Lin, S. Thakur, in *24th Annual Meeting of International Society of Magnetic Resonance in Medicine*. (24th Annual Meeting of International Society of Magnetic Resonance in Medicine, Singapore, 2016), pp. 227.

170. M. L. Zierhut, E. Ozturk-Isik, A. P. Chen, I. Park, D. B. Vigneron, S. J. Nelson, (1)H spectroscopic imaging of human brain at 3 Tesla: comparison of fast three-dimensional magnetic resonance spectroscopic imaging techniques. *Journal of magnetic resonance imaging : JMRI* **30**, 473-480 (2009).

171. S. J. Nelson, Y. Li, J. M. Lupo, M. Olson, J. C. Crane, A. Molinaro, R. Roy, J. Clarke, N. Butowski, M. Prados, S. Cha, S. M. Chang, Serial analysis of 3D H-1 MRSI for patients with newly diagnosed GBM treated with combination therapy that includes bevacizumab. *Journal of neuro-oncology* **130**, 171-179 (2016).